Growth and Characterization of Bismuth Perovskite Thin Films for Integrated Magneto-Optical Isolator Applications

by

ALEXANDER R. TAUSSIG

A.B. Physics, 2005
Harvard University

Submitted to the Department of Materials Science & Engineering
in partial fulfillment of the requirements for the degree of

Master of Science in Materials Science & Engineering

at the

MASSACHUSETTS INSTITUTE OF TECHNOLOGY

June 2007

Author .....
Department of Materials Science & Engineering
May 4, 2007

Certified by .....
Caroline A. Ross
Professor of Materials Science & Engineering
Thesis Supervisor

Accepted by .....
Samuel M. Allen
Professor of Materials Science & Engineering
Chairman, Committee on Graduate Students

Growth and Characterization of Bismuth Perovskite Thin Films for Integrated Magneto-Optical Isolator Applications

by

ALEXANDER R. TAUSSIG

A.B. Physics, 2005

Harvard University

Submitted to the Department of Materials Science & Engineering
on May 4, 2007, in partial fulfillment of the
requirements for the degree of
Master of Science in Materials Science & Engineering

Abstract

In this thesis, we discuss the motivation for integrated magneto-optical isolators and explain why the orthoferrite is such an attractive materials class for this purpose. We then derive from first physical principles the dependence of Faraday rotation, absorption, and certain figures of merit on the material's dielectric tensor elements. Next, we use pulsed laser deposition to grow thin films of $BiFeO_3$ on MgO (001) and $SrTiO_3$ (001) substrates. After optimizing growth conditions to obtain high quality films, we characterize the films' crystal structure with two-dimensional x-ray diffraction. We then examine the magnetic, optical, and magneto-optical properties of these films. We find that the highly textured films grown on $SrTiO_3$ are monoclinic with an out-of-plane c-axis aligned with the (001) direction of the substrate and approximate pseudocubic lattice parameters of $a = b = 4.04$ Å, $c = 3.95$ Å, and $90° - \beta = -0.88°$. These films are weakly magnetic, with a magnetization of 1.2 emu/cm^3 at an applied field of 10 kOe; highly absorptive, with an average absorption coefficient of 910 cm^{-1}; and possess a low specific Faraday rotation of 32°/cm at 1.8 kOe of applied field. As expected, we find that the magneto-optical figure of merit is negligible for this material due to its high absorption, which we attribute to a thin surface layer of phase separated bismuth and iron oxides caused by bismuth segregation during growth. We offer additional explanations for these values and show the first results of newer, more promising work with mixed cation perovskites.

Thesis Supervisor: Caroline A. Ross
Title: Professor of Materials Science & Engineering

Acknowledgments

When I reflect upon the long chain of events that have brought me to this point in my scientific career, I begin to wonder when exactly my interest in science began. For whatever reason, the first thought that pops into my head is an excerpt from the famous Bill Watterson comic strip *Calvin and Hobbes*. Calvin, an inquisitive young boy with an unusually active imagination, would often ask his father questions about basic scientific phenomena like this one:

> Calvin: "Dad, what makes wind?"
>
> Dad: "Trees sneezing."
>
> Calvin: "Really?"
>
> Dad: "No, but the truth is more complicated."

Like Calvin, I have to thank, before all others, my parents Andrew and Susan Taussig for their wisdom and guidance. Although my father probably knows slightly less then Calvin's about the origin of wind, that never stopped him from attempting to explain it to me; nor did it stop him from teaching me algebra, the "birds and the bees," or why Motown was the center of the world from 1959 to 1972. My mother taught me the beauty of art and language, the intricacies of the five paragraph essay, and that you should *always* write a thank you note, no matter how inedible the dinner was.

I also owe a great deal of gratitude to the teachers who helped me along the way, in science and otherwise. In particular, I would like to thank my musical mentor Dr. Johannes Somary, who taught me to "pursue excellence and eschew mediocrity" and whose pervasive optimism and *joie de vivre* have been a constant source of inspiration. In addition, I would like to thank my advisor Dr. Caroline Ross, whose gentle encouragement always kept me going in the face of experimental woes and whose door was always open to me and the rest of her students.

I am indebted to the other members of my laboratory group who have taken time to teach me various experimental methods and help me collect data. Lei Bi, especially, deserves a great deal of thanks for all of his efforts, as well as Vikram Sivakumar and Hyun-Suk Kim. I would also like to thank our collaborator Dr. Gerry Dionne for

all his helpful conversations as well as Dr. Scott Speakman, who was responsible for teaching me two-dimensional x-ray diffraction.

Of course, I can not forget all the wonderful friends I have made at MIT in the past 2 years. Each of you has brought such great happiness to my life and truly made this school home to me. I especially want to thank my two sidekicks—Adam Eisenman and Danny Truque. You two are my KGs, my BPSs, and, without you, I never would have never "found the chicken." I had seven nightmares last night, and you two were in eight of them.

Finally, on a more serious note, I would like to thank my grandfather Ralph Taussig, who was responsible more than anyone for encouraging me to learn as much as I could. From the time I could talk, he took me to museum after museum, informed me of different cultures and languages, and dazzled me with his stories from World War II. Pop, this thesis is dedicated to you; I know you would have loved to read it. We all love you and miss you.

Thanks for the lessons and memories, everyone.

— ALEXANDER R. TAUSSIG, May 4, 2007

Contents

List of Figures

List of Tables

Chapter 1

Introduction

> What we call "progress" is the exchange of one nuisance for another nuisance.
>
> —HENRY HAVELOCK ELLIS, *Impressions and Comments*

The British doctor of sexual psychology Henry Havelock Ellis (1859-1939) wrote the above words in response to opposition to his theories on human sexuality. Although in this epigraph Ellis laments the paradox of social progress, the same statement could be used to describe the transition from contemporary electronic computers to the so-called "microphotonic" computers of the future. We shall see over and over again in the discussion that follows a theme common to all scientific investigations—that sweeping paradigm change requires the comprehension and, ultimately, the exchange of what seem to be fundamental obstructions to progress for ones which are hopefully less cumbersome.

1.1 The Silicon Microphotonics "Revolution"

As stated in an industry roadmap publication in 2005 [1], "silicon microphotonics seeks to build optical devices on the platform that has enabled Moore's Law: electronics-grade, single-crystal silicon. Beyond this, definitions diverge." The divergence the authors refer to is the lack of consensus on the materials systems required

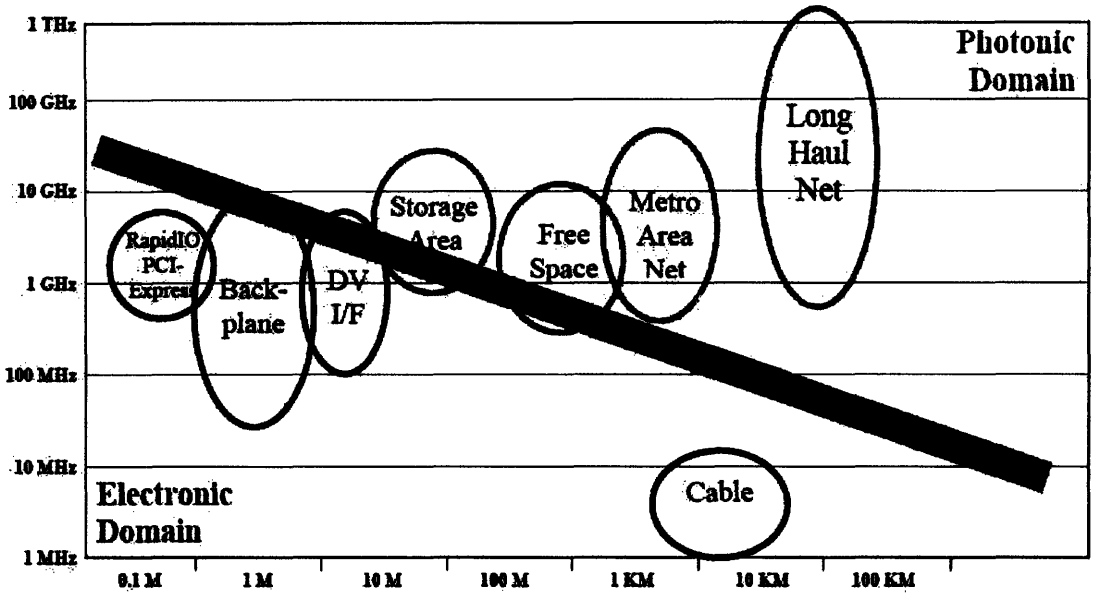

Figure 1-1: Illustration of the tradeoff between distance and bandwidth in communications links, with the market transition zone from electronic to photonic technologies indicated in red [1].

to achieve the goal of a fully functioning integrated photonic chip. While some researchers insist we draw upon the diversity of other compound semiconductor systems and eventually integrate them with silicon, others attempt to create all the necessary devices from silicon and silicon-based dielectrics alone. Regardless of one choice or the other, all researchers in this field believe that microphonotics will eventually be a truly disruptive technology, a "revolution," if you will.

The drivers of this revolution, as indicated in the roadmap, are the fundamental limitations of electronic communications links. The most significant of these are physical loss mechanisms like dielectric losses and skin effect losses, both a function of distance and bandwidth. These problems are exacerbated by noise limits necessitated by crosstalk and process technology. Shannon's law, which defines a theoretical maximum rate at which information can be transmitted error-free, creates a maximum bandwidth which contemporary electronic links are now approaching. Furthermore, as we approach this limit, the marginal cost of the next unit of bandwidth gets higher and higher.

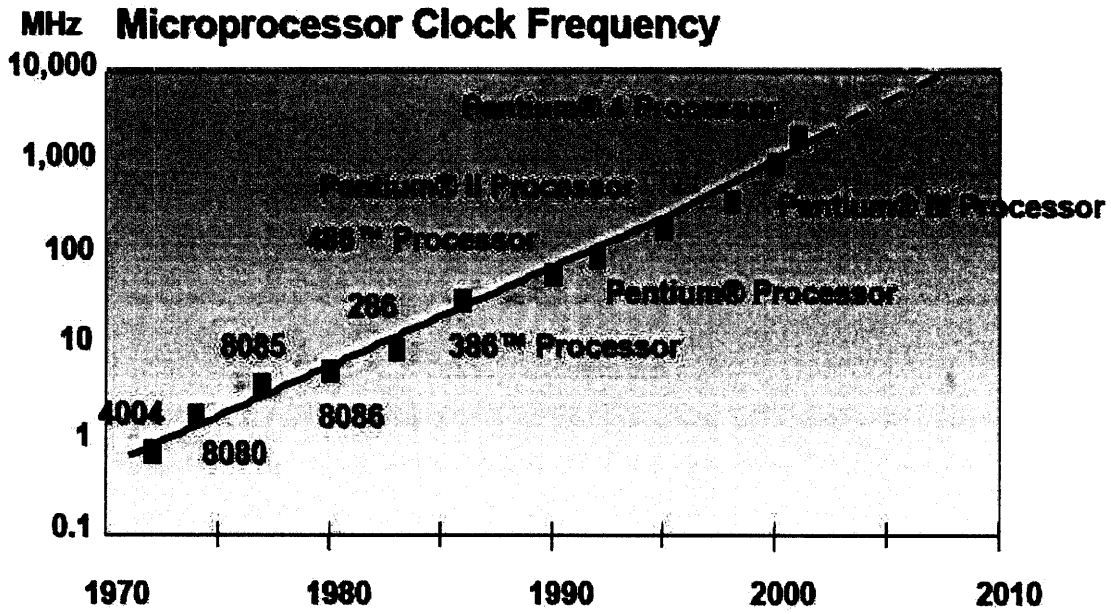

Figure 1-2: Graph showing the exponential increase of clock frequency over time [1].

There is, in fact, always a tradeoff between distance and bandwidth; hence, the electronics/microphotonics industry finds the distance-bandwidth product to be an important figure of merit. As shown in Figure 1-1, when this product is large (i.e. on the right side of the red zone), the market favors photonic communication. Fiber optic links have been used for over 25 years in the "long haul net" market, and the areas indicated in green have been added chronologically from right to left as the technology has improved. Clearly, microphotonics is getting better and better at satisfying different market needs.

The roadmap also makes certain predictions based on current Moore's laws. In 2005, serial computer buses had a bandwidth of 2.5 GHz, doubling every 4 years. Since the electrical limit is 15-20 GHz, the roadmap predicts a transition to photonic communication in 2017. The backplane bandwidth, 3.6 GHz in 2005, increases at the same rate and will reach its 10-20 GHz limit by 2013.

Clock frequencies, as shown in Figure 1-2, are also increasing exponentially as a function of time. Even if Moore's law could continue as shown, an unfortunate side effect is that processor heat dissipation scales with clock frequency. With con-

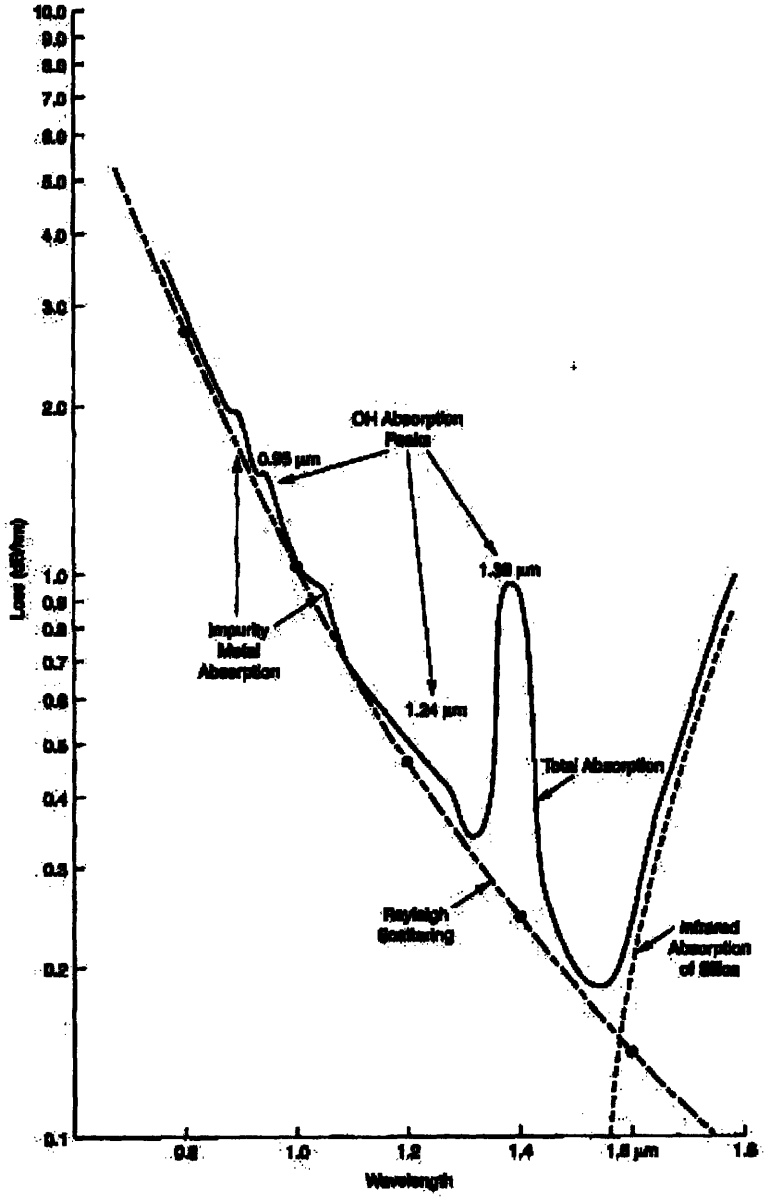

Figure 1-3: Total attenuation in an SiO_2 fiber due to various absorption resonances and Rayleigh scattering [2].

temporary processors exceeding 100 W of dissipated power, higher electronic clock frequencies will become increasingly difficult and expensive to package and cool.

So, why is a photonic link such a good choice for low loss, and therefore low heat and high power efficiency? Simply put, light doesn't heat things up. An electron traveling through a copper wire, even one of excellent purity, is still subject to several loss mechanisms. A photon traveling through an SiO_2 waveguide without any significant bends, however, shows almost no attenuation of light of the appropriate wavelength. For SiO_2, a minimum in loss of 0.2 dB/km is reached at $\lambda_0 = 1550$ nm, as shown in Figure 1-3 [2]. This particular wavelength is therefore a very important one for long distance communication and possibly also for integrated photonic technology, which is why we will later choose to analyze Faraday rotation in our samples at this wavelength. In contrast, RG-6 coaxial copper cable, which is typically used for low loss at high frequency in cable and satellite television as well as cable modems, has an attenuation of 242 dB/km at 400 MHz, more than 3 orders of magnitude greater [46]. Since electric losses increase as a function of frequency, higher data modulation and transmission will only result in an increase of this figure.

This low attenuation, therefore, gives us two advantages over metal wires for transmitting data: less signal lost during transmission and less heating at high frequencies of operation. In addition, there is another advantage to photonic communication that has to do with the nature of light itself. Unlike electrons, photons have color; and, hence, we can send more than one color down the same fiber (perhaps on the order of 40 or 50 of them) and then, using a filter, read each color separately as a different stream of information. This process is known as wavelength-division multiplexing (WDM). The benefit is clear if you have ever waited in a slowly moving line at a movie theater with only one door. If the movie theater had 50 doors, for the same amount of people, the total entrance time would be less. By adding more doors, the effective "bandwidth" of the theater entrance has increased by a factor of 50, assuming there is no pushing and shoving for seats!

An optical link consists of more than a transmission medium, however. As shown in the link schematic in Figure 1-4, it also consists of a light source (typically a laser

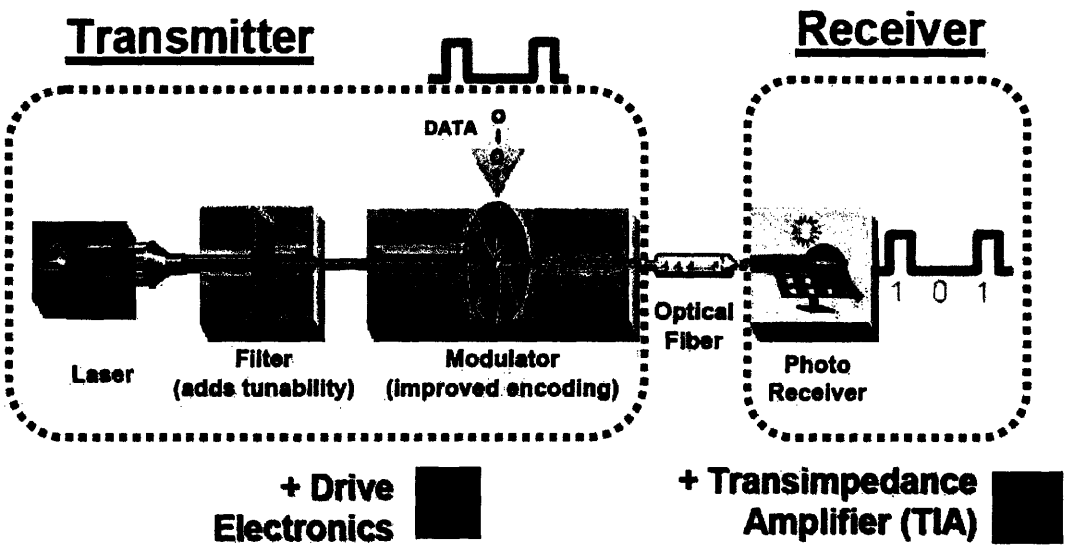

Figure 1-4: Schematic of an optical link [1].

or LED), a tunable filter, a modulator, and a receiver. All of these components are essential parts of the link, and each provides its own obstacles to the materials science community. Overcoming these obstacles in order to reap the benefits of an optical computer will be the challenge of proponents of microphotonics in the next 10 years. We will play our part in this struggle by addressing a component that will usually be employed between the laser and the filter, but in principle can be used at any point in a microphonotic circuit—the isolator.

1.2 Integrated Magneto-Optical Isolators

An isolator, in an optical circuit, is simply a one-way valve for light. A magneto-optical isolator is an isolator controlled by an applied magnetic field via the Faraday effect or Faraday rotation. Such a device is not only desirable, but wholly necessary for any system which employs a laser light source. As described in [47],

> When coupling laser diodes to optical waveguides, fibres, or components, the inevitable back reflections that arise from the connection interface travel back into the laser cavity resulting in what's known as reflection

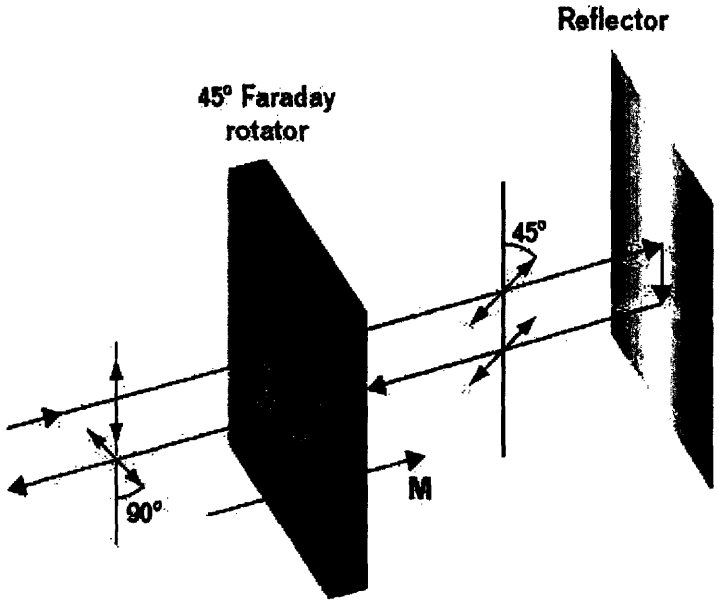

Figure 1-5: Demonstration of nonreciprocal rotation of light passing through a medium exhibiting the Faraday effect. The reflected beam, having passed through the 45° active medium twice, is now orthogonal to the original beam [3].

noise or injection noise. This causes instabilities, leading to restrictions on the operational speed and reduced lifetime of the devices.

Not surprisingly, not all materials can be magneto-optically isolating. There are two main requirements, the first of which is that the material possess a large Faraday rotation per unit length, i.e. it must rotate a linearly polarized beam of light through a large angle in a short distance and do so in a nonreciprocal fashion. Nonreciprocality, as shown in Figure 1-5, is the independence of the direction of rotation from the direction of propagation of the light. The direction of rotation should depend only on the magnetization or applied field vector. The other requirement is that the material be transparent to the wavelength in use so that loss due to the isolator is minimized.

With such a material, one can construct the canonical bulk magneto-optical isolator shown in Figure 1-6. The two polarizers shown are oriented 45° from one another along the axis of propagation. In between them, the active material sits along the propagation axis with enough thickness to provide 45° of nonreciprocal rotation. Incoming light made linear by the first polarizer will then pass through the active

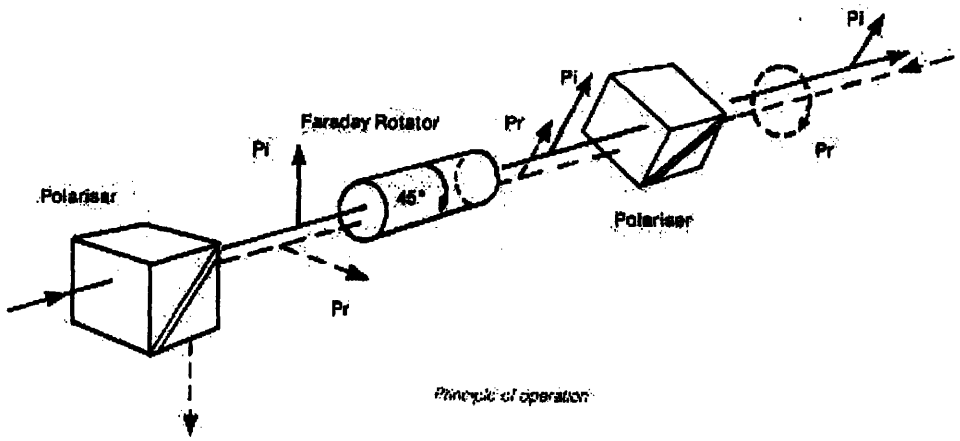

Figure 1-6: Schematic of a bulk magneto-optical isolator with the incoming beam shown in blue and the back-reflected beam shown in black. Note that the second polarizer is tilted about the propagation axis 45° with respect to the initial polarizer so that, upon superposition at the initial polarizer, the outgoing and incoming waves deconstructively interfere [4].

medium, rotate 45°, and pass completely through the second polarizer. If the light is reflected downstream, however, it will pass back through the second polarizer, rotate *in the same direction* by 45°, and completely annihilate at the first polarizer since it is orthogonal to the original outgoing beam.

Integrated isolators, unfortunately, can not use this bulk design. Instead, we need a planar solution, compatible with waveguide technology. A planar solution poses two significant problems: shape birefringence and angular selectivity. The former problem arises because films tend to grow with misfit strain when grown on mismatched substrates, thereby inducing a difference between values of both the index of refraction and loss coefficient in different directions. In general, the film will therefore be both birefringent and dichroic. The angular selectivity problem exists due to the difficulty of making two integrated polarizers that are oriented 45° from each other, although it is relatively easy to do so with a 90° separation through the use of selective TM absorption [47].

Fortunately, there are solutions to both of these problems, most of which can achieve an isolation ratio (defined as the logarithm of the ratio of incoming light to

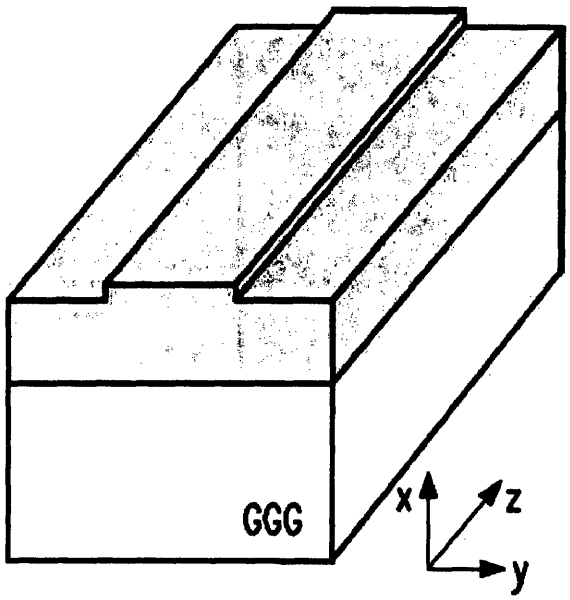

Figure 1-7: Schematic of a ridge waveguide magneto-optical isolator with an active garnet material grown on a gadolinium gallium garnet (GGG) substrate [5].

outgoing) of −30 dB or better and a forward loss of less than 0.5 dB. Some of these solutions involve etching various ridges and trenches into planar waveguides to create structures like the one shown in Figure 1-7. Others involve the utilization of clever device architectures, some of which combine reciprocal and nonreciprocal rotation to get the desired result, like the Mach-Zehnder interferometer (MZI) isolators shown in Figure 1-8. Finally, solutions exist in both these categories for which the polarization dependence of incoming light has been removed with some degree of reliability. Rather than paraphrase the details here, we refer the reader to an excellent review article which reports the state of the art in magneto-optical waveguide isolators [5].

1.3 Roadblocks to Integration and Our Solution

Despite the fact that waveguide isolators have been fabricated and can perform fairly robustly, with good isolation ratios and forward losses, there have been few successful attempts at integrating these waveguides into a microphotonic link. The main reason for the lack of progress in this final endeavor is that the magnetic garnets which are

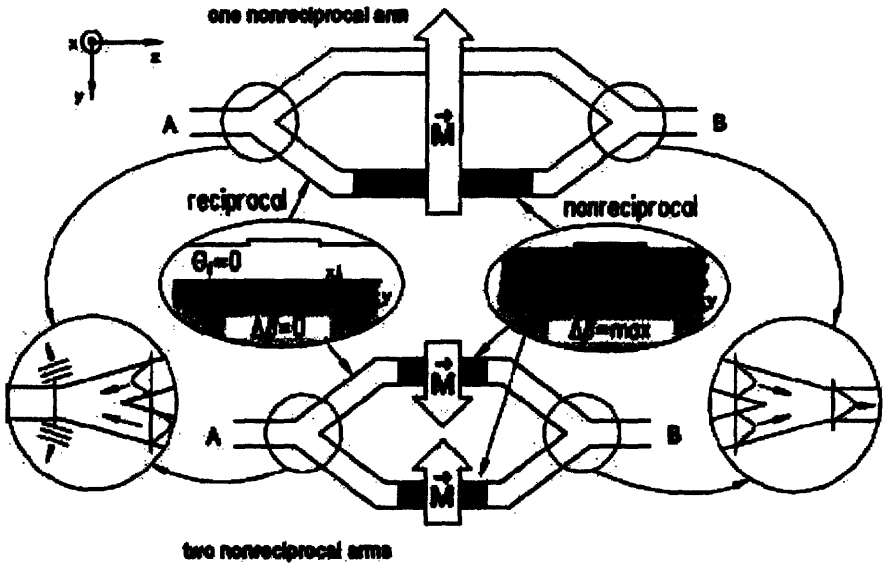

Figure 1-8: Design of two MZI isolators, one which has both a reciprocal and a nonreciprocal rotation arm (top) and one which has two oppositely magnetized nonreciprocal arms (bottom) [5].

used as the active Faraday medium have such large lattice parameters (on the order of 12 Å) that they can not be grown epitaxially on silicon or any silicon buffer layer. The research community has, hence, approached this issue in two ways. They have either focused on making the isolator on a garnet substrate, effectively ignoring the integration issue, or they have attempted to wafer bond the garnet to a compound semiconductor device grown on a single crystal substrate like InP, as shown in Figure 1-9 [6]. Since wafer bonding is an expensive fabrication step both from a thermal budget and monetary cost standpoint, some attempts have been made to use an MgO buffer layer between the garnet and the semiconductor substrate in a more simple fabrication method like metal-organic chemical vapor deposition [48, 49].

In this thesis, we decide to take a completely different approach to the problem of integration. In fact, we view the problem of creating a truly integrated magneto-optical isolator not as a device design or fabrication issue, but as a materials selection issue. We have decided to move entirely away from the garnet and replace our active material with a member of the perovskite class. The advantage of doing so is that the perovskites are far better lattice-matched to semiconductors and oxide buffer

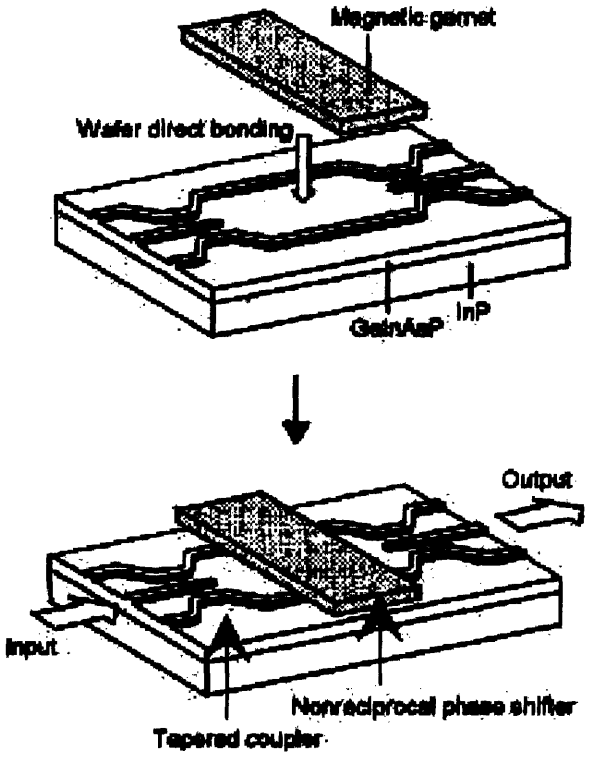

Figure 1-9: A schematic showing the wafer bonding of a magnetic garnet to a GaInAsP-based MZI isolator grown on an InP substrate [6].

layers, so we expect to find epitaxial growth if we pick our materials system carefully. Furthermore, certain subsets of the perovskite class like the orthoferrites have been shown to have very high intrinsic Faraday rotation (despite high linear birefringence) coupled with low optical absorption at near infrared wavelengths. The combination of these three properties—low lattice mismatch, high Faraday rotation, and low loss—makes the perovskite, and specifically the orthoferrite, a potentially useful materials class for magneto-optical isolators.

Chapter 2

Isolator Materials: From Iron Garnets to Orthoferrites

Although the iron garnet ($R_3Fe_5O_{12}$, in which R is typically a rare-earth element or other trivalent specie) is currently the material of choice for optical isolators as well as other important magneto-optic devices, the orthoferrite class ($RFeO_3$) will turn out to be an important isolator material as well, particularly in microphotonic circuits. At the telecommunications wavelength $\lambda_0 = 1550$ nm, R=Bi has particularly attractive qualities. Nevertheless, in order to understand why orthoferrites are so promising, we need to first understand what makes the iron garnet the current leading material for isolation.

2.1 Iron Garnets

2.1.1 Composition & Crystal Structure

The conventional unit cell of a garnet is cubic, with space group $Ia3d$ (O_h^{10}) and a lattice parameter on the order of 12 Å. The formula $R_3Fe_5O_{12}$ may be more accurately written $\{R^{3+}\}_3[Fe^{3+}]_2(Fe^{3+})_3O_3$, where { } denotes a dodecahedral "c" site, [ ] denotes an octahedral "a" site, and ( ) denotes a tetrahedral "d" site. The O^{2-} anions then coordinate each of these cations, forming a close-packed structure. The {c} site is

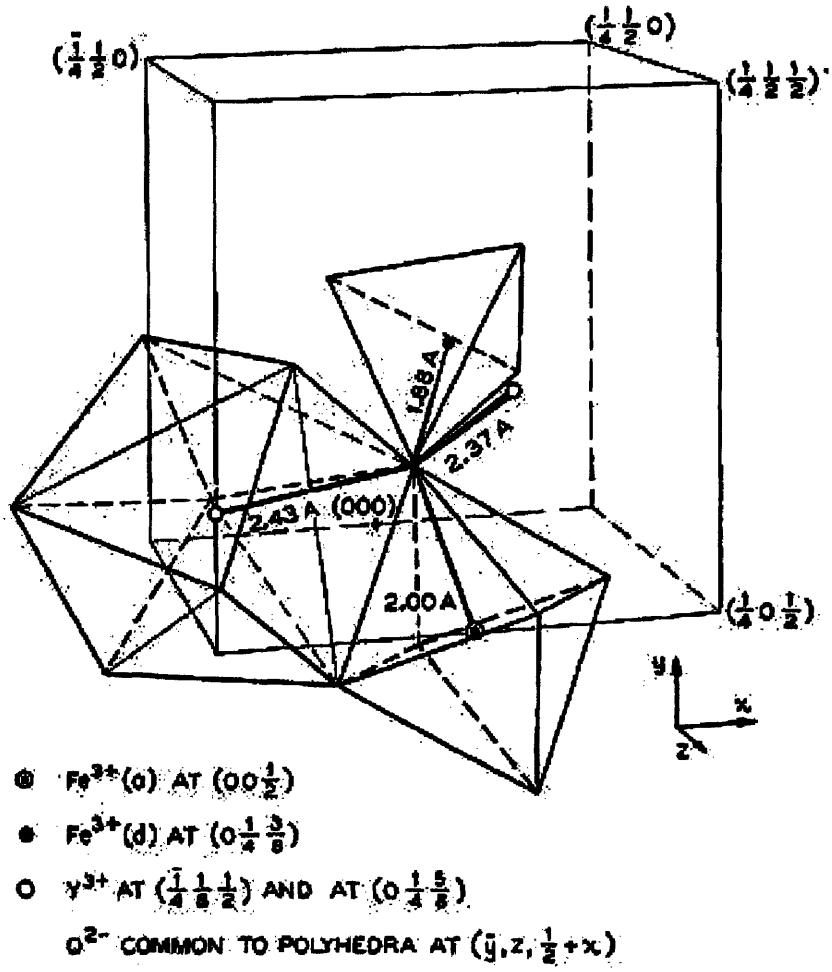

Figure 2-1: Oxygen coordination of cations within conventional unit cell of YIG. Also, $a = 12.376 \pm 0.004$ Å [7].

surrounded by 8 O's, the [a] by 6, and the (d) by 4 [50, pg. 163]. Figure 2-1 shows very clearly how each of these coordinated structures fits within the conventional unit cell for Yttrium Iron Garnet (YIG), where R=Y.

2.1.2 Growth Methods

Iron garnets can be grown from the melt in single crystal form, but they can also be deposited with various thin film techniques, including liquid phase epitaxy (LPE) [51], chemical vapor deposition (CVD) [52], metal-organic chemical vapor deposition (MOCVD) [53], sputtering [54], and pulsed laser deposition (PLD) [55, 56]. Because

Table 2.1: TYPICAL PLD CONDITIONS FOR BIG ON GGG (111) FROM [41]

Growth Parameter	Value
Laser λ_0	KrF, 248 nm
Pulse length	25 ns
Repetition rate	10-50 Hz
Target stoichiometry	Bi:Fe $\approx$ 3:5
Energy density	5 J/cm^2
Substrate temperature	550°C
O_2 background pressure (during deposition)	18.75 mTorr
O_2 background pressure (during cooling)	525 Torr
Cooling rate	10°C/min

we are most interested in PLD, we provide an example of typical deposition conditions for bismuth iron garnet (BIG) on a (111) oriented gallium gadolinium garnet (GGG) substrate in Table 2.1.[1]

2.1.3 Magnetic Properties

The iron garnet is a ferrimagnet because the Fe^{3+} in the conventional unit cell which reside on the [a] sites anti-align with those on the 3 (d) sites. The magnitude of the effective field between the [a] and (d) lattices is quite large, nearly 2 MOe. Because the two sublattices, coupled via superexchange through neighboring oxygen anions, are aligned oppositely, the moment of the garnet is then simply the difference, i.e. that of one Fe^{3+} per unit cell, or 5 μ_B/cell at 0 K.[2] This value of the saturation magnetization can be increased or decreased, however, as a function of amounts of substituent cations on these lattice sites. In reality, garnets of pure form are rarely used except as substrates or in some other structural purpose [50, pgs. 163-4]. In addition, the coercivity of a YIG film, for instance, can be fairly low, less than 35 Oe, as shown by the *M-H* hysteresis loop in Figure 2-2 [8].

[1] A description of the PLD technique can be found in Section 4.1 and an additional reference for BIG PLD deposition on GGG can be found in [57].

[2] A good description of superexchange and many other magnetic phenomena described herein may be found in [58].

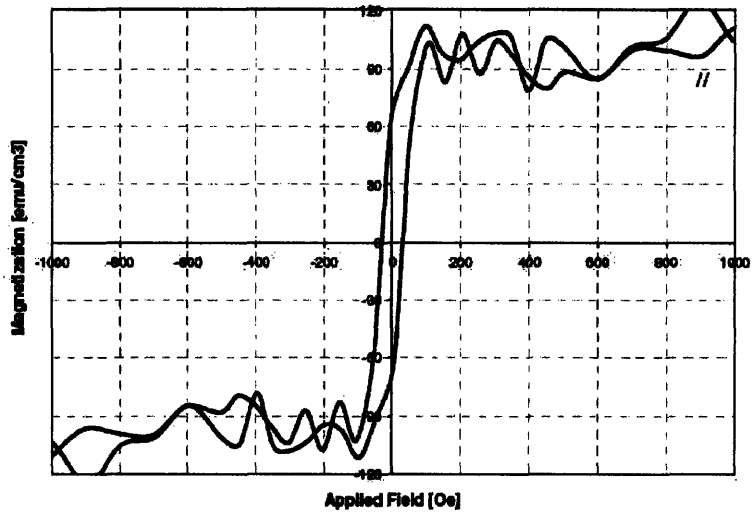

Figure 2-2: VSM hysteresis loop of a YIG thin film [8].

2.1.4 Optical and Magneto-Optical Properties

The iron garnet is so useful as an isolator in the near infrared because of its nearly zero absorption (α as low as 0.03 cm^{-1}) from $\lambda_0 = 1200$ nm to 5000 nm in some cases. At the long wavelength limit, α begins to grow because of vibrational lattice resonances of the ions within the garnet. At the short wavelength limit, α grows rapidly because of the abundance of electronic transitions of the Fe^{3+} cations. These electronic transitions either come from crystal field splittings of the Fe^{3+} levels in the octahedral and tetrahedral sites or from a charge transfer process from the Fe cations to the O anions. The measured absorption spectra for various rare-earth iron garnets is shown in Figure 2-3.

Of particular interest are those electronic transitions near the band edge of the garnet, as those will be the ones which extend their tails into the infrared region. Analysis of the crystal field of the Fe^{3+} cation in both a tetrahedral and an octahedral coordination has yielded the energy band diagram in Figure 2-4. The bottom level, where the energy is defined as 0 eV, is the $^6A_{1g}$ level, and the transitions from this level to the various other field-split levels are the ones in which we are interested. As we can see from Figure 2-4, the lowest energy transition in the garnet ($h\nu = 1.38$

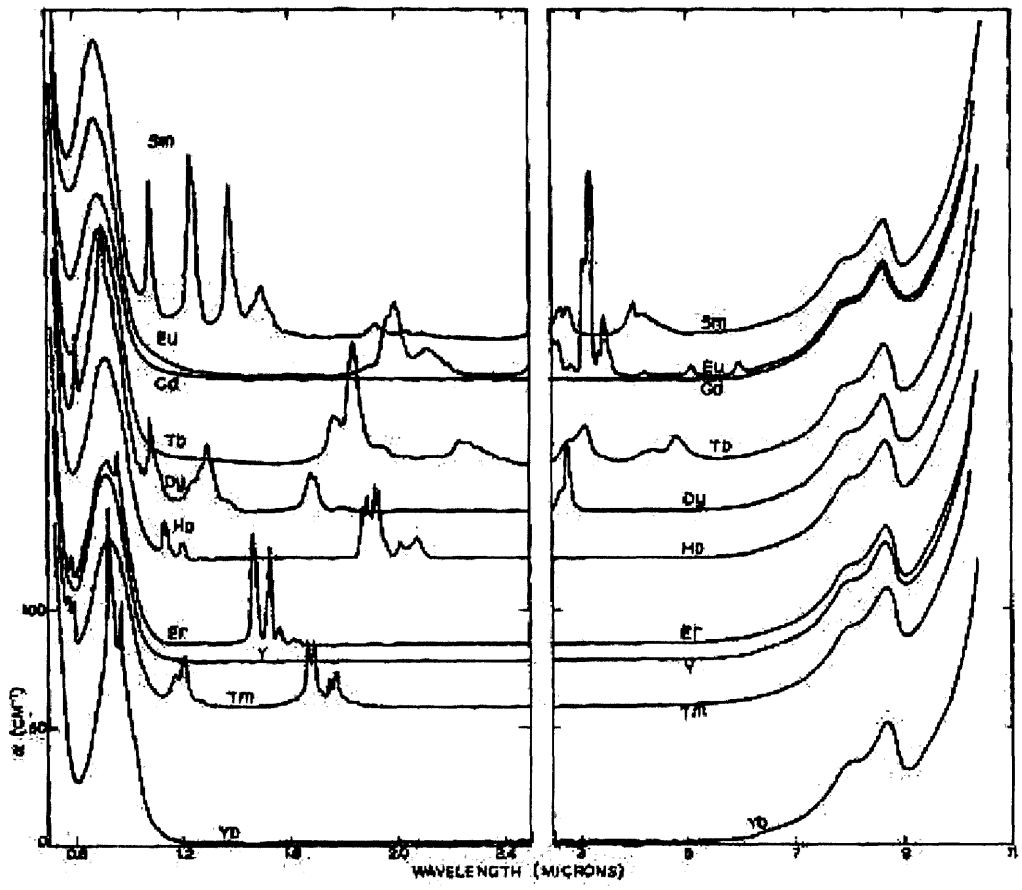

Figure 2-3: Absorption spectra for the rare-earth iron garnets [9].

eV, or $\lambda_0 = 900$ nm) is from the octahedral cation in the $^6A_{1g}$ to $^4T_{1g}$ transition. A list of the various transitions at the band edge of YIG, their wavelengths and energies, coordination sources, and oscillator strengths (a measure of the probability of a particular transition) can be found in Table 2.2 [42].[3]

Of course, a good isolator material must be magneto-optically active as well as transparent in the range of interest. YIG, as shown in Figure 2-5, is such a material. Ga-substituted YIG is shown because diluting the garnet with Ga on Fe sites can change the magnetization of the material, as well as the Faraday rotation. Substituting Bi on the Y sites can also increase Faraday rotation a great deal. We see this effect in Figure 2-5 by examining how different the scales are on the positive and negative vertical axes. In fact, the magnitude of the Faraday rotation (the direction

[3]A more comprehensive list of transitions can be found in [10].

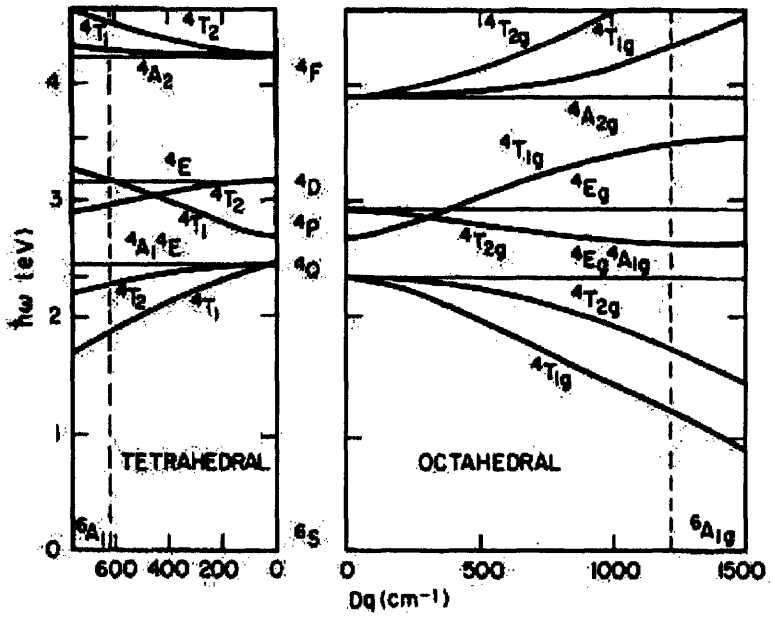

Figure 2-4: Energy level schematic for the Fe^{3+} cation coordinated in both a tetrahedral (left) and octahedral (right) site. The vertical lines correspond to the value of the crystal field parameter Dq in YIG [10].

Table 2.2: PARAMETERS OF THE OPTICAL TRANSITIONS IN YIG AT 77 K FROM [42]

λ_0 (nm)	$h\nu$ (eV)	Transition	Fe^{3+}	Oscillator Strength
900	1.38	$^6A_{1g}(^6S) \rightarrow {}^4T_{1g}(^4G)$	Oct	2×10^{-5}
690	1.80	$^6A_{1g}(^6S) \rightarrow {}^4T_{2g}(^4G)$	Oct	2×10^{-5}
620	2.00	$^6A_{1g}(^6S) \rightarrow {}^4T_1(^4G)$	Tet	8×10^{-5}
510	2.44	$^6A_{1g}(^6S) \rightarrow {}^4T_2(^4G)$	Tet	1.6×10^{-4}
480	2.59	$^6A_{1g}(^6S) \rightarrow {}^4E,{}^4A_1(^4G)$	Tet	3×10^{-5}
470	2.64	$^6A_{1g}(^6S) \rightarrow {}^4E_g,A_{1g}(^4G)$	Oct	2×10^{-5}
440	2.82	$^6A_{1g}(^6S) \rightarrow {}^4T_{2g}(^4D)$	Oct	1×10^{-4}
430	2.89	Not crystal field		2×10^{-3}
410	3.03	$^6A_{1g}(^6S) \rightarrow {}^4T_2(^4D)$	Tet	6×10^{-5}
390	3.19	Not crystal field		4×10^{-3}
365	3.40	Not crystal field		1×10^{-2}

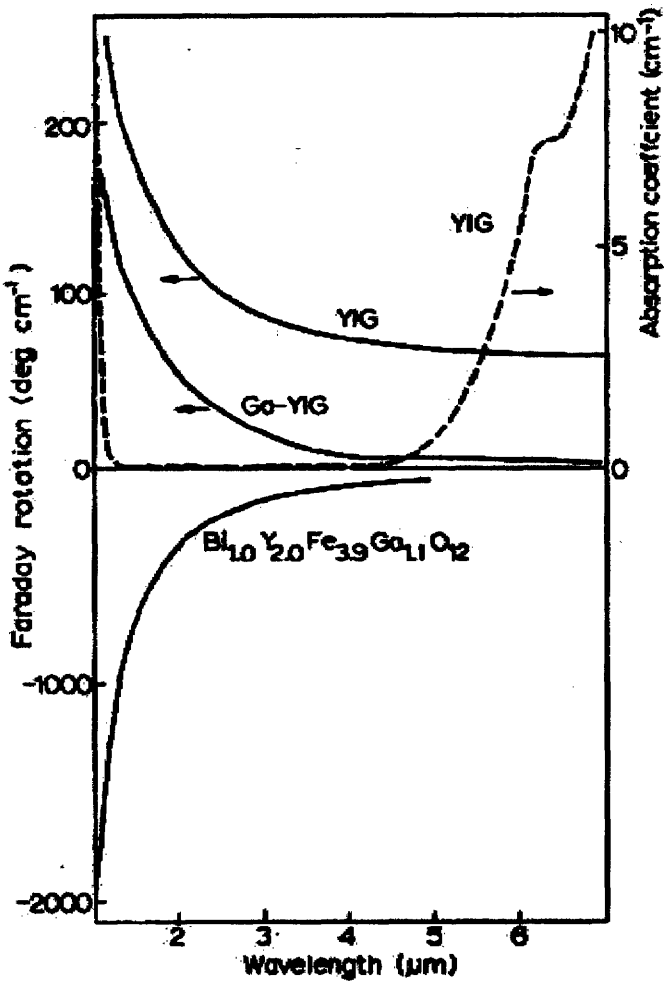

Figure 2-5: Comparison between Faraday rotation (left axis, solid) in YIG, Ga-YIG, and Bi,Ga-YIG at infrared wavelengths. Note the change in the scale of the positive and negative axes. In addition, the absorption spectra of YIG is plotted (right axis, dotted) [11].

has changed) at $\lambda_0 = 1500$ nm has grown by over a factor of 4 between YIG and $Bi_{1.0}Y_{2.0}Fe_{3.9}Ga_{1.1}O_{12}$ (Bi,Ga-YIG)! The reason for this increase will be examined in the next chapter, wherein we shall discuss the theoretical origins of Faraday rotation

. High Faraday rotation seems to be a property of most garnets, particularly rare earth iron garnets. A systematic study of Faraday rotation spectra at infrared wavelengths can be found in [12], although we have specifically included the infrared Faraday rotation spectra of YIG, HoIG, YbIG, TbIG, DyIG, ErIG, and GdIG in Figure 2-6 here.

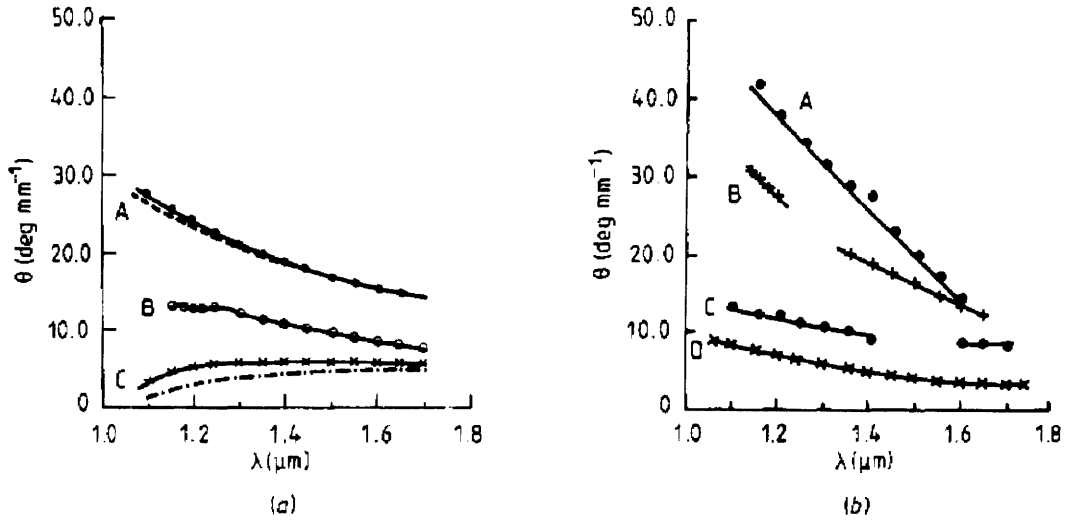

Figure 2-6: Faraday rotation spectra ($H = 1900$ Oe, $T = 20°$C) of (a) YIG (A), HoIG (B), and YbIG (C) and (b) TbIG (A), DyIG (B), ErIG (C), and GdIG (D) [12].

2.1.5 Application in Isolator Devices

Garnets are the natural choice in optical isolators for several reasons, some of which are described above. What engineers are chiefly concerned with in designing any device, however, are the values of certain figures of merit. In our case, we are interested in the magneto-optical figure of merit, defined as $F_\Theta \equiv |\Theta|/\alpha$, where Θ is the Faraday rotation per unit length (or "specific" Faraday rotation) and α is the absorption coefficient given in either cm^{-1} or dB/cm^{-1}. This figure of merit will be discussed in greater detail in the following chapter, but suffice it to say that any good isolator should have a large Θ and a small α in order to maximize F_Θ. At $\lambda_0 = 1550$ nm, for pure, bulk YIG, $F_\Theta = 9.1°/\text{dB}$; but, for substituted garnets like $Yb_{1.12}Bi_{1.03}Y_{0.85}Fe_5O_{12}$ (YbBi:YIG), F_Θ can be as high as $25.8°/\text{dB}$ [13]. The spectra of Θ and α for YbBi:YIG, as well as those of F_Θ for YbBi:YIG and YIG, can be found in Figure 2-7.

Furthermore, because garnets are inherently cubic, linear birefringence, which is detrimental to device performance, is usually negligible in the bulk. However, garnet films grown on mismatched substrates can be strained, and this strain may cause its own birefringence. Fortunately, ridges may be etched into the garnet waveguide and

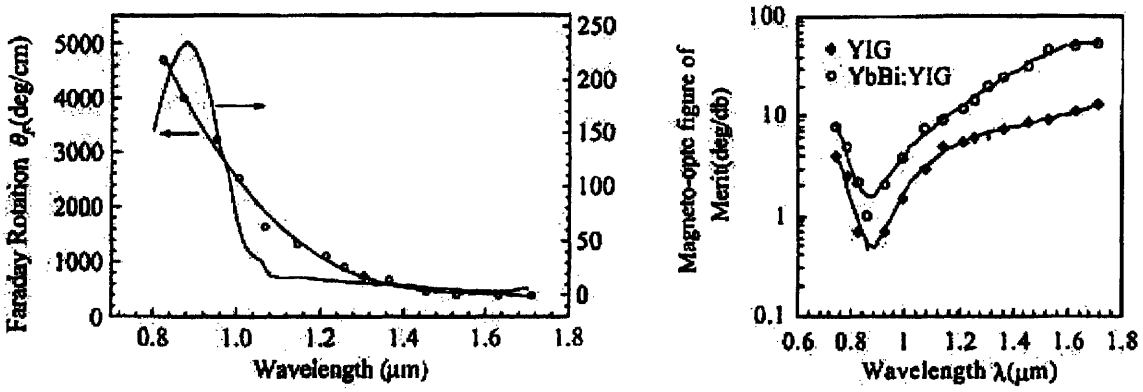

Figure 2-7: For YbBi:YIG, Θ and α (left), along with F_Θ (right) for YbBi:YIG (open circles) and YIG (closed diamonds) [13].

shape birefringence may be used to exactly cancel the stress birefringence at a certain wavelength. Using such a method, zero linear birefringence has been obtained in a Bi:YIG system at $\lambda_0 = 1500$ nm with an isolation ratio (see definition in previous chapter) of -25 dB or better [59].

The biggest problem with garnet isolators, however, is their inability to be easily integrated into a silicon-based microphotonic circuit. Because of their significant lattice mismatch to many semiconductor substrates, there is little hope for epitaxial growth. It is for this reason that we turn to a materials class long abandoned for use in optical isolators—the orthoferrite.

2.2 Orthoferrites

2.2.1 Composition & Crystal Structure

The orthoferrite ($RFeO_3$) is a sub-class of the larger perovskite crystal class (ABO_3), so, in order to understand its structure, we must first understand that of the larger category. Perovskites in the bulk typically take on one of four crystal structures: cubic (e.g. $SrTiO_3$), tetragonal (e.g. $BaTiO_3$ at room temperature), orthorhombic (e.g. $GdFeO_3$), or rhombohedral (e.g. $BiFeO_3$). The crystal structure of the first of these, which is the simplest, is shown in Figure 2-8.

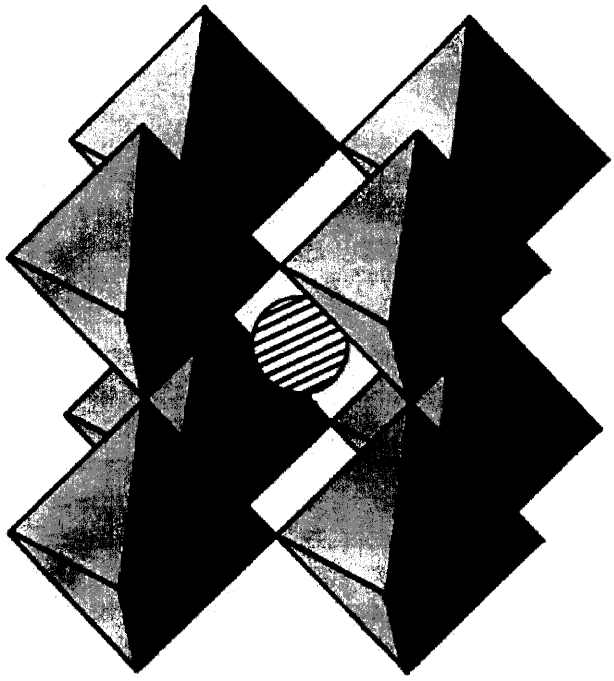

Figure 2-8: The ideal, cubic perovskite (ABO_3) structure (e.g. $SrTiO_3$). Here, the lightly-shaded body center is the A-site, the black corner dots are the B-sites, and the octahedra vertices (which lie on the edge centers) are the sites of the O^{2-} anions [14].

As we can see, each of the B-sites is octahedrally coordinated by oxygen atoms, as is the [a] site in the garnet, while the A-site lies in the middle of these octahedra. If we were to place the A-sites on cube corners (i.e. place the body center in Figure 2-8 on the unit cell's corner), the oxygens would sit on the face centers and the B-site would lie in the body center [60].

In order to visualize the other crystal structures, we can take $BaTiO_3$ as model system. As temperature is varied, a single crystal of $BaTiO_3$ will actually take on all 4 of the possible perovskite crystal structures shown in Figure 2-9. At high temperatures, the structure is cubic; between 5°C and 120°C, it is tetragonal; between -90°C and 5°C, it is orthorhombic; and below -90°C, it is rhombohedral [15].[4]

As previously mentioned, the orthoferrite class is a subclass of the perovskite class

[4]A brief list of crystallographic definitions: cubic means $a = b = c$ and $\alpha = \beta = \gamma = 90°$; tetragonal means $a = b \neq c$ and $\alpha = \beta = \gamma = 90°$; orthorhombic means $a \neq b \neq c$ and $\alpha = \beta = \gamma = 90°$; and rhombohedral means $a = b = c$ and $\alpha, \beta, \gamma \neq 90°$.

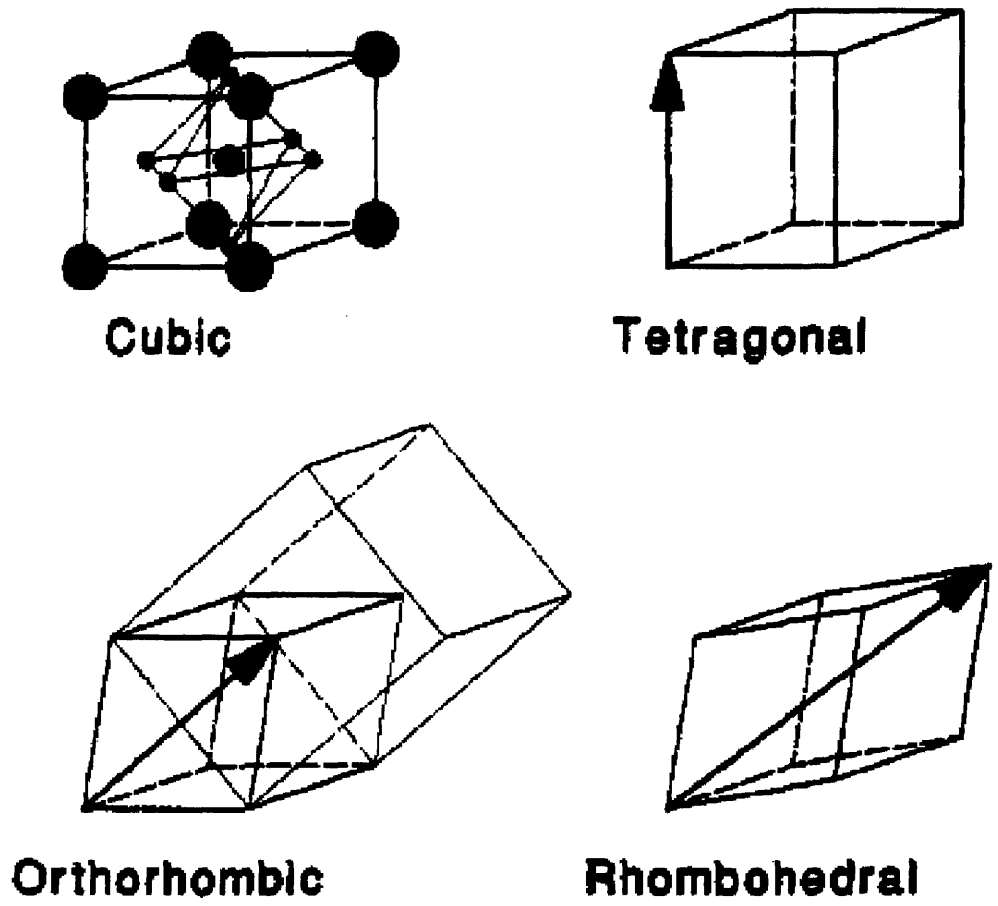

Figure 2-9: Crystal structure of the 4 different phases of $BaTiO_3$, corresponding to $T > 120°C$ (cubic), $5°C < T < 120°C$ (tetragonal), $-90°C < T < 5°C$ (orthorhombic), and $T < -90°C$ (rhombohedral). The arrows point in the direction of electric polarization ([001] for tetragonal, [011] for orthorhombic, and [111] for rhombohedral) since $BaTiO_3$ is a ferroelectric material [15].

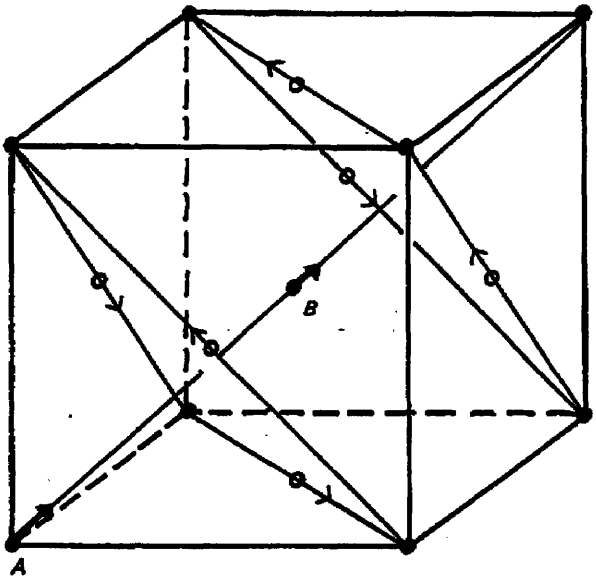

Figure 2-10: Atomic displacements in $BiFeO_3$ along the [111] axis of the pseudocubic unit cell. The corner A-sites are Bi, the body center B-site is Fe, and the open circles are O. The (111) planes which contain the O are indicated. The respective displacement directions of each atom are indicated by the arrows [16].

in which an Fe atom sits on the B-site. We are motivated to choose this subclass by our experience with the garnet class, wherein the Faraday rotation is the sum of that arising from so-called "electric dipole transitions" of the electrons belonging to both octahedrally and tetrahedrally coordinated Fe^{3+} cations. In the garnet, these electric dipole transitions give Faraday rotations in opposite senses; in the orthoferrite, however, the tetrahedral Fe^{3+} does not exist, so we would naively expect the Faraday rotation, now solely from an octahedral cation, to be much higher. Although this assumption turns out to be false due to low inherent magnetization, the orthoferrite still has great potential as isolator material. We will pay particularly close attention to $BiFeO_3$ (BFO), for reasons that will be discussed imminently.

BFO has a rhombohedrally distorted perovskite structure. It is often helpful to picture it, at first, as a cubic perovskite, and then imagine displacing each of the atoms in the cell to obtain the rhombohedral structure. In Figure 2-10, we see how the A- and B-sites of the now *pseudo*cubic unit cell are shifted along the [111] direction (by 0.62 ± 0.03 Å and 0.23 ± 0.03 Å, respectively), while the O atoms are shifted along

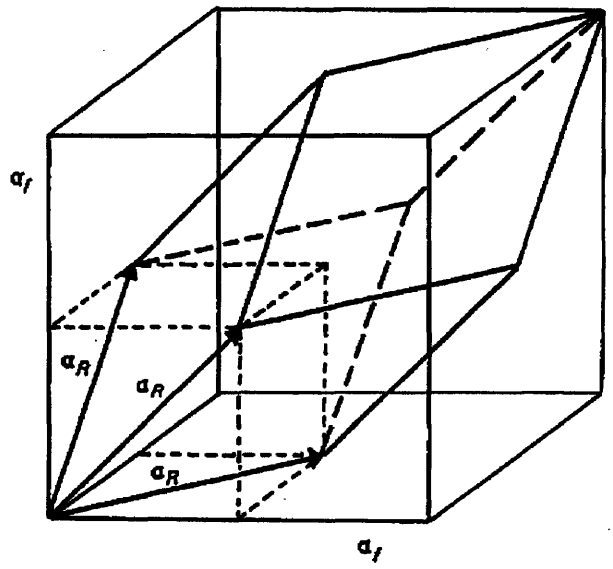

Figure 2-11: Relationship between the pseudocubic unit cell (lightly dashed) of BFO and the rhombohedral unit cell. a_R is the unit vector of the rhombohedral cell, but is also equivalent to the length of [110] in the pseudocubic cell. $a_f/2$ is the pseudocubic unit cell parameter a_{pc} [16].

<110>-type directions in the (111) plane (by 0.30 ± 0.03 Å [18, pg. 22]). These shifts stretch the cell in the [111] direction, turning the cubic crystal into a rhombohedral one, as shown in Figure 2-11.

The effect of shifting the oxygens, in particular, is a differential rotation ω between the adjacent octahedra. As shown in Figure 2-12, when these octahedra are offset by ω, they form a periodic structure along the [111] pseudocubic direction that passes through 2 adjacent octahedra before repeating itself. Furthermore, if we look along the [111] direction, we can see that the (111) planes form something approaching a close-packed structure, as in a hexagonal array. It is therefore convenient to represent BFO as a hexagonal crystal in which the pseudocubic [111] direction is equivalent to a new [0001] direction. This hexagonal cell contains 6 formula units, and the oxygen atoms are arranged in equidistant planar layers normal to, and intersecting, the c axis at values of $z = (1/12)(2n + 1)$, where n is an integer. If we look at a plane in between adjacent oxygen planes, i.e. a (0002) plane, we can see more clearly how $\omega \neq 0$ impacts the crystal structure. From Figure 2-13, we can see that ω has

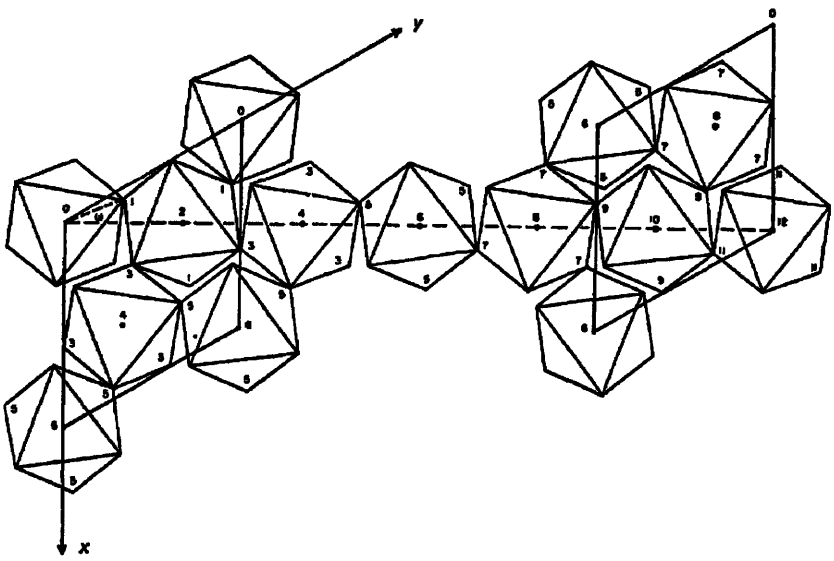

Figure 2-12: Three-dimensional rotation of oxygen octahedra oriented in the [111] pseudocubic direction (also the [0001] hexagonal direction) sharing corners and offset by an angular displacement ω. The numbers correspond to the heights of the octahedral positions in units of $c/2$, where c is the [0001] direction lattice parameter of the hexagonal cell. The solid lines on the left represent the bottom of the hexagonal unit cell, while the solid lines on the right represent the top [17].

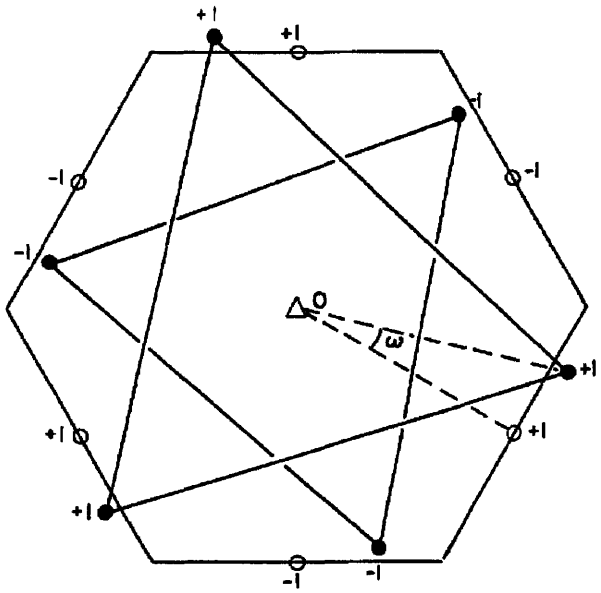

Figure 2-13: Cross section of BFO in (0002)-type plane showing the effect of $\omega \neq 0$. $\circ$ = Oxygen atom in ideal perovskite, $\bullet$ = shifted position of oxygen atom. The numbers refer to distance above and below the (0002)-type plane in units of $c/12$ [16].

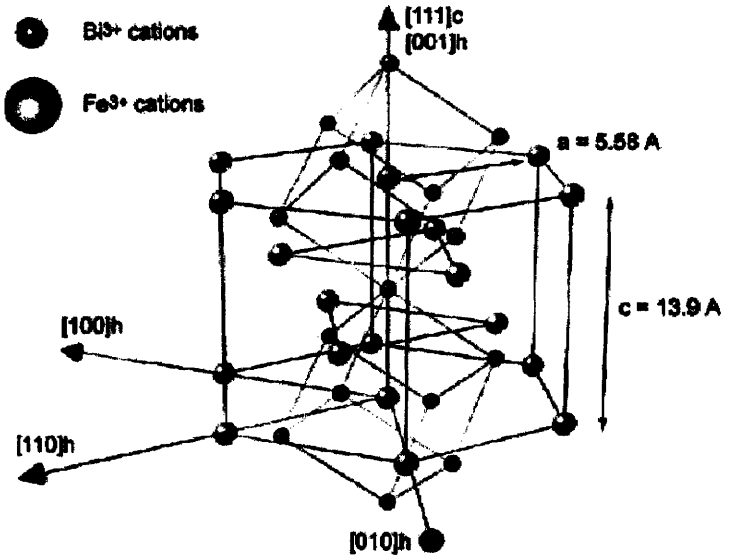

Figure 2-14: The hexagonal unit cell of BFO with the pseudocubic unit cell also indicated [18].

the effect of rotating all the oxygens in the plane by the same amount, in the same direction. It can be shown that ω has a maximum value of 60°, in which case the array is perfectly hexagonally close-packed. On the other hand, when $\omega = 0°$, the lattice is that of a purely cubic perovskite. In the case of BFO, $\omega = 11.4°$, so it is somewhere in between these two extremes [16].

In summary, BFO in bulk, single crystal form can be considered a member of the space group $R3c$, described by the hexagonal unit cell in Figure 2-14. There are several different conventions for describing its unit cell. In the hexagonal convention in which we have been working, $a_H = 5.5799 \pm 0.0003$ Å and $c_H = 13.8670 \pm 0.0005$ Å. We can also represent the crystal as a rhombohedral crystal, however, containing 2 formula units of BFO with $a_R = 5.6336 \pm 0.0003$ Å and $\alpha_R = 59°20.86 \pm 0.30'$ [61]. The most convenient way to represent the unit cell of BFO, though, is with a pseudocubic cell. The reason this choice is convenient is that, for most perovskites, any deformation from a cubic system is small, and at high temperatures many often revert back to cubic forms. Furthermore, when we consider epitaxial growth on cubic substrates like $SrTiO_3$, it makes more sense to reference a pseudocubic unit cell for

the film. Therefore, we shall relate the pseudocubic lattice parameter a_{pc} and the angular deformation parameter α_{pc} (e.g. $\alpha_{pc} = 90°$ for a perfect cubic material) to a_H and c_H with

$$a_{pc} = \frac{1}{2}\sqrt{\frac{2a_H^2}{1-\cos\alpha_{pc}}} \tag{2.1}$$

$$\cos\alpha_{pc} = \frac{c_H^2 - 6a_H^2}{c_H^2 + 12a_H^2} \tag{2.2}$$

as well as a_{pc} and α_{pc} to the rhombohedral parameters with

$$a_{rh} = a_{pc}\sqrt{2(1+\cos\alpha_{pc})} \tag{2.3}$$

$$\cos\alpha_{rh} = \frac{3\cos\alpha_{pc}+1}{2(\cos\alpha_{pc}+1)} \tag{2.4}$$

Eqs. (2.1-2.2) are from [62] while Eqs. (2.3-2.4) are from [16]. When we plug into Eqs. (2.1-2.2) the above measured values for a_H and c_H, we find that $a_{pc} = 3.9648$ Å and $\alpha_{pc} = 89.445°$ (or $90 - \alpha_{pc} = 0.555°$). Henceforth, we will refer to these as the lattice parameters of BFO in its bulk state.[5]

Epitaxial films of BFO, however, have different structural properties. When grown on cubic $SrTiO_3$ (STO) with $a = 3.905$ Å, if the substrate and film are both assumed to be oriented (001), then $\epsilon_m = (a_{\text{STO}} - a_{\text{BFO}})/a_{\text{STO}} \approx -0.77\%$ is the lattice strain between the film and the substrate [63]. This degree of mismatch can be compensated differently by changes in the crystal structure of the film that depend on what orientation of the STO substrate is used. Table 2.3 summarizes a recent experiment in which BFO films were deposited by PLD onto STO (001), (101), and (111) substrates. The dependence of the film's crystal structure on the substrate orientation was then examined.[6] Although films were grown epitaxially at all orientations of the

[5]It should also be mentioned that there is a direct relationship between the rhombohedral angular parameter α_{rh} and the aforementioned octahedral tilt ω given by

$$\cos\alpha_{rh} = (4 - \cos^2\omega)/(4 + 2\cos^2\omega)$$

Further analysis and a far more detailed treatment of different crystallographic representations of a rhombohedral perovskite may be found in [62].

[6]It should be noted that in the case of the (101) film, monoclinic lattice parameters were not

Table 2.3: STRUCTURAL PARAMETERS OF BFO/STO FILMS AS A FUNCTION OF SUBSTRATE ORIENTATION FROM [43] WITH CALCULATION OF (101) PARAMETERS FROM [44]

STO Orientation	BFO Structure	$a = b$	c	$90° - \alpha$	$90° - \beta$
(001)	Monoclinic	4.001 Å	3.935 Å		−0.6°
(101)	Monoclinic	3.984 Å	3.989 Å		+0.4°
(111)	Rhombohedral	3.959 Å	3.959 Å	+0.6°	
None (Bulk BFO)	Rhombohedral	3.959 Å	3.959 Å	+0.6°	

substrate, the (111) oriented film showed the least strain and had a structure closest to that of the bulk crystal [43]. Similar results for a (001) oriented substrate have been obtained by [22]. Interestingly enough, it has been found that the monoclinic distortion of these (001) films can be reduced or even eliminated by substituting La on the Bi sites in BFO, creating a tetragonal, epitaxial film [64]. Even when the BFO film is grown by PLD on a $Pt/TiO_2/SiO_2/Si$ multilayer substrate and annealed, La substitution still removes the monoclinic distortion and creates a tetragonal crystal [65].

2.2.2 Growth Methods

Some orthoferrites can be grown in bulk crystal form, but most, including BFO, are now grown with various thin film methods. These include LPE [66], MOCVD [67], sol-gel [68], and PLD [19, 22]. Since PLD is our growth method of choice and BFO is our material of interest, we shall focus on the conditions of BFO growth by PLD. A systematic study was performed by [19] and a phase diagram as a function of deposition temperature T and oxygen pressure p_{O_2} was assembled and can be found

calculated explicitly. We therefore took the provided $d-$spacings and used them to solve for the lattice parameters using the equation

$$d_{hk\ell} = a \sin\beta / \sqrt{h^2 + k^2(a \sin\beta/b)^2 + \ell^2(a/c)^2 - 2h\ell(a/c)\cos\beta}$$

where a and b, the in-plane parameters, c, the out-of-plane parameter, and β, the in-plane deformation angle, describe a monoclinic crystal [44]. It should also be noted that, in Table 2.3, for the rhombohedral crystal, the coordinate axes switch from the pseudocubic ones that describe the monoclinic cell to rhombohedral ones in which $a = b = c$ and α describes the angle in between each of these axes. Finally, the reader may have noticed that the bulk values in Table 2.3 differ from those previously provided in this section; because they differ only slightly, we will proceed without worrying too much about it.

Table 2.4: OPTIMAL PLD CONDITIONS FOR BFO ON STO (001) FROM [19]

Growth Parameter	Value
Laser Wavelength	Nd:YAG, 355 nm
Repetition rate	2.5 Hz
Target stoichiometry	Bi:Fe $\approx$ 1.15:1
Substrate temperature	580°C
O_2 background pressure (during deposition)	7.50 mTorr
O_2 background pressure (during cooling)	225 Torr
Growth Rate	2.4-3.6 nm/min

in Figure 2-15. The optimal deposition conditions for this experiment are displayed in Table 2.4. Further study by the same group found that the important deposition parameters were not only T and p_{O_2}, but also length of deposition, i.e. the thickness t of the film. A phase diagram as a function of p_{O_2} and t can be found in Figure 2-16. As we can see from both Figure 2-15 and 2-16, growth conditions must be properly maintained in order to grow a film which is free of impurity phases, particularly γ-Fe_2O_3 and Bi_2O_3. The former impurity phase is favored at high temperature and low pressure, where the volatile Bi atoms are depleted from the film, driving it off stoichiometry. When the Bi:Fe ratio is low, the majority phase is then γ-Fe_2O_3 (maghemite), which is a ferrimagnetic material with a Curie temperature $T_C = 577°C$ and a saturation magnetization $M_s = 420$ emu/cm^3 or 1.25 μ_B/Fe atom [69]. The presence of this phase in a BFO film, even in small quantities, can easily raise the film's magnetization, which should be several orders of magnitude lower, as will be discussed imminently.[7] This increase in M_s is obviously undesirable if we want to examine the M_s of the BFO itself.

At the other extreme, high pressure and low temperature, the impurity phase is Bi_2O_3 which, although it not ferromagnetic or ferrimagnetic, is still undesirable if it dilutes the desirable properties of the BFO component of the film. It occurs because the high overpressure and low temperature cause the Bi not to be volatile "enough," leaving us with a film with a Bi:Fe ratio greater than 1 [20]. Thus, we see that

[7]Further investigation of these types of films by another group revealed that the majority phase at low deposition pressure is actually the canted antiferromagnetic α-Fe_2O_3, but that γ-Fe_2O_3 can make up as much as 20% of the volume of the film deposited at $p_{O_2} \leq 1.0$ mTorr, thus driving M_s to as much as 80 emu/cm^3 [69].

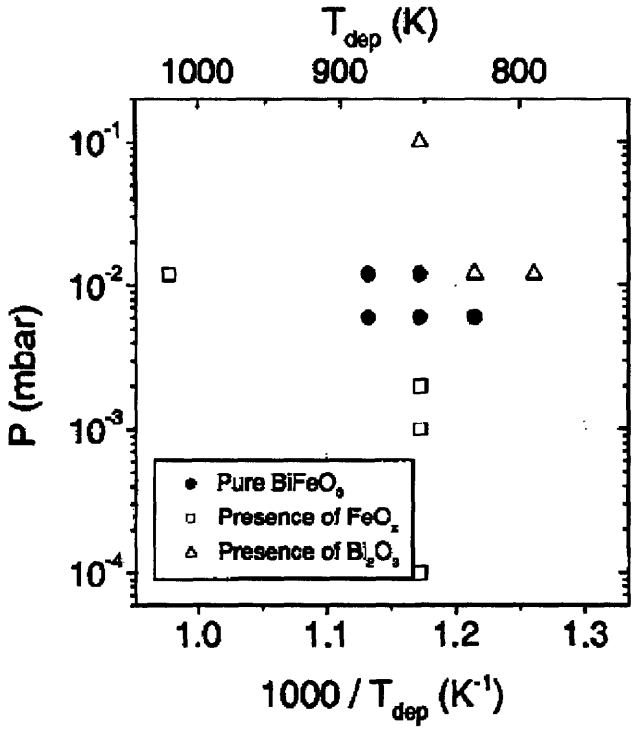

Figure 2-15: Pressure-temperature phase diagram for BFO growth by PLD on STO (001) substrates [19].

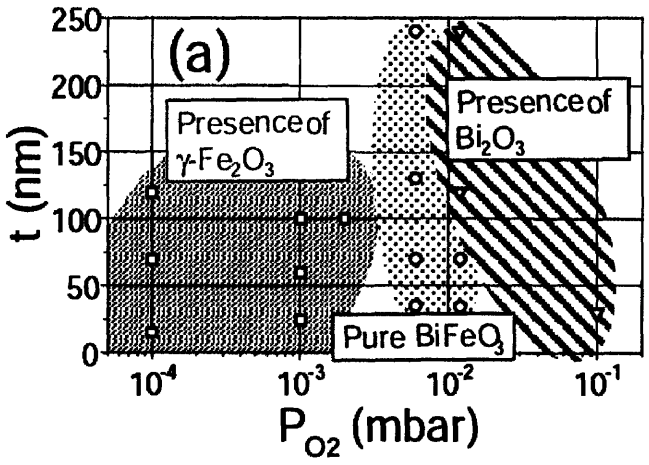

Figure 2-16: Pressure-thickness phase diagram for BFO growth by PLD on STO (001) substrates [20].

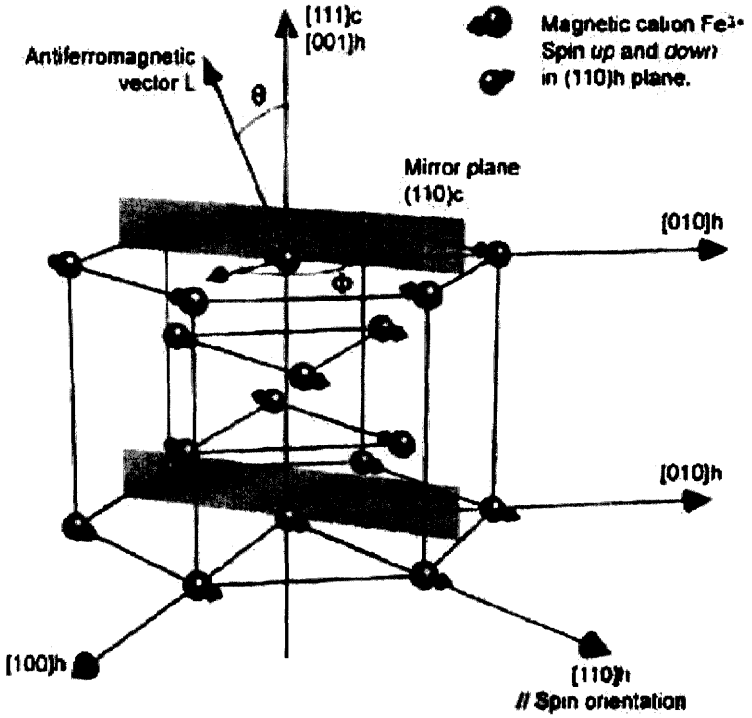

Figure 2-17: Hexagonal crystal representation of G type antiferromagnetic ordering in BFO. Both the order and spin rotation planes are shown [21].

controlling T and p_{O_2}, as well as t to second order, is necessary to avoid parasitic phases in our films.

2.2.3 Magnetic Properties

Orthoferrites are magnetic because of exchange interactions between the Fe^{3+} atoms on the B-sites. These exchange interactions are antiferromagnetic in nature, and adjacent sublattices in the crystal structure will have spins which align oppositely. In non-cubic orthoferrites, like BFO, however, these spins do not exactly cancel each other out. Instead, they are aligned in a given direction with a slight canting of about 0.5°, yielding a small, but non-zero, magnetization [50, pg. 141].

As shown in Figure 2-17, BFO has G type antiferromagnetic order along the [0001] hexagonal direction (or the [111] pseudocubic direction). In this arrangement, each Fe^{3+} cation is surrounded by 6 nearest neighbors of the opposite spin configuration

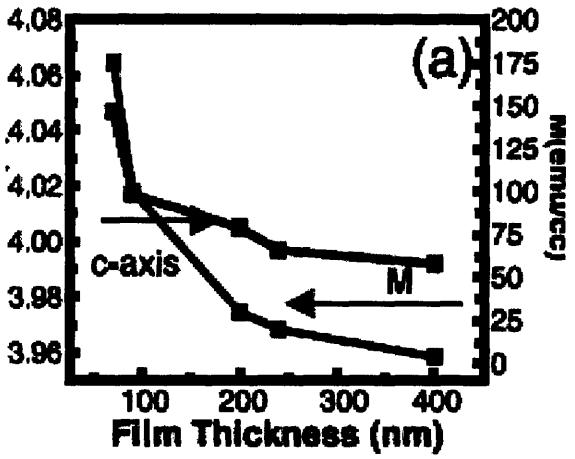

Figure 2-18: Thickness dependence of the saturation magnetization M and tetragonal, out-of-plane c axis in BFO/STO(001) film [22].

[21]. The spins are oriented perpendicular to the [0001] hexagonal direction (i.e. in the $[11\bar{2}0]$ direction), but are canted slightly out of this plane. Furthermore, superimposed on this antiferromagnetic ordering is a spiral spin structure of period $\lambda_s \approx 620$ Å which is directed along the $[11\bar{2}0]$ hexagonal direction [70]. Because of the nearly symmetric nature of the spiral spin structure, the antiferromagnetic vector $\boldsymbol{L}$ shown in Figure 2-17 averages out to zero over several λ_s, and so does the magnetization. In addition, the spiral reduces the remanent magnetization to zero. In thick BFO films ($t > 200$ nm $> \lambda_s$), then, we usually measure a small "saturation" M_s (which is not really saturation since the material is difficult to saturate because of the spiral) on the order of 2-9 emu/cm^3 or 0.01-0.06 μ_B/Fe at $H = 6$ kOe [69, 71].[8]

Thin BFO films ($t < 200$ nm), however, experience some very strange and controversial magnetic effects. A paper published in *Science* which claimed an $M_s = 150$ emu/cm^3 (or 1 μ_B/Fe) for a 70 nm BFO film [22] elicited a decisive response [71]. The former group claimed that the inverse relationship between M_s and t, shown in Figure

[8]Sometimes it is necessary to convert units of M_s from μ_B/cell or μ_B/Fe atom (which are really the same thing in an orthoferrite) to emu/cm^3 or emu/g. For a (001) oriented BFO film with the lattice constants given in Table 2.3, the density of BFO is $\rho = 8.25$ g/cm^3 and the conversion becomes

$$1\ \mu_B/\text{Fe} \approx 147\ \text{emu/cm}^3 \approx 17.9\ \text{emu/g}$$

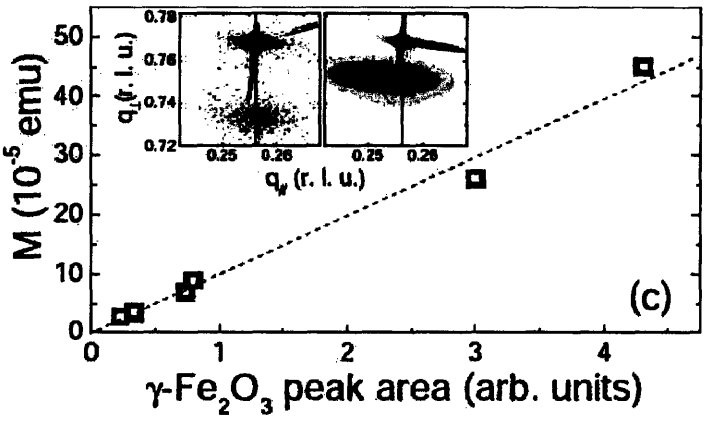

Figure 2-19: Saturation magnetization M of films grown at 0.075 mTorr and 0.75 mTorr O_2 dependence on area of γ-Fe_2O_3(008) XRD peak [20].

2-18, could be attributed to strain effects in the BFO films since there is a similar relationship between thickness and the out-of-plane lattice parameter c. The latter group refuted their claim and blamed the high M_s on the presence of Fe^{2+} in their films, which were grown in reducing conditions. The latter group found films of similar thickness with the expected M_s of around 0.05 μ_B/Fe. Although Fe^{2+} was found in these films by the former group under closer inspection [72], their explanation of why it would raise M_s to such a great degree is inconclusive. Although the presence of γ-Fe_2O_3 would explain a large M_s, it would not necessarily explain the thickness dependence, unless somehow highly strained films favored growth of the iron oxide phase. It is very possible that, with one-dimensional x-ray diffraction (1DXRD), the group in [22, 72] may have missed epitaxial γ-Fe_2O_3 peaks. In our experimental section, we will describe how we avoid such pitfalls by using two-dimensional XRD (2DXRD).

Some of this controversy may have been at least partially solved by [20]. They point out that the (00l) peaks of γ-Fe_2O_3 are extremely close to those of BFO. Therefore, when looking at a BFO (002) peak, one can not resolve the adjacent γ-Fe_2O_3 (004) peak. Furthermore, there is *no* epitaxial γ-Fe_2O_3 peak adjacent to the BFO (003) peak, which is the one used to identify the BFO phase in [22]. One needs to scan large angles and look at the BFO (004) peak to see the adjacent γ-Fe_2O_3 (008),

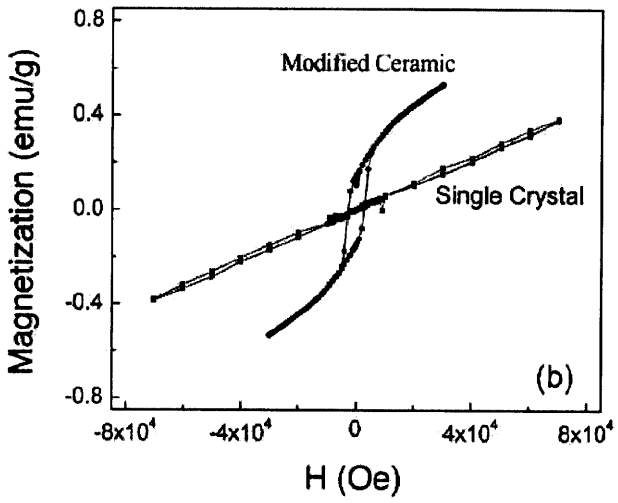

Figure 2-20: *M-H* hysteresis loops for modified $(Bi_{0.8}La_{0.2})(Fe,Ga)O_3$-43%$PbTiO_3$ and BFO single crystals [23].

which are distinguishable from one and other. As shown in Figure 2-19, once this peak area is related to the M_s, there is almost a linear dependence, suggesting that an extra, strongly ferrimagnetic phase is responsible for the anomalously large M_s found in [22].

Other interesting magnetic properties of BFO arise from its unusual spiral spin structure. The spiral is, in general, undesirable because it prevents the Fe^{3+} spins from aligning with an applied field, causing zero remanence. It is therefore advantageous to destroy this cycloidal spin configuration. There are currently two methods for doing so: chemically and elastically. As an example of the first method, one group found that, using a solid solution $(Bi_{0.8}La_{0.2})(Fe,Ga)O_3$-43%$PbTiO_3$ which is close to a morphotropic phase boundary, they were able to break the cycloid and release some of the spins to align more freely with an applied field. Hysteresis loops of their alloy compared with a regular BFO crystal, shown in Figure 2-20, clearly show remanence (0.25 emu/g or 2.1 emu/cm^3) and saturation (0.3 emu/g or 2.5 emu/cm^3), whereas the BFO sample shows neither [23]. A similar effect can be achieved by doping BFO with 1-3 mol% Nb, but to a much smaller degree, yielding a remanence of only 0.015 emu/g or 0.12 emu/cm^3 [73].

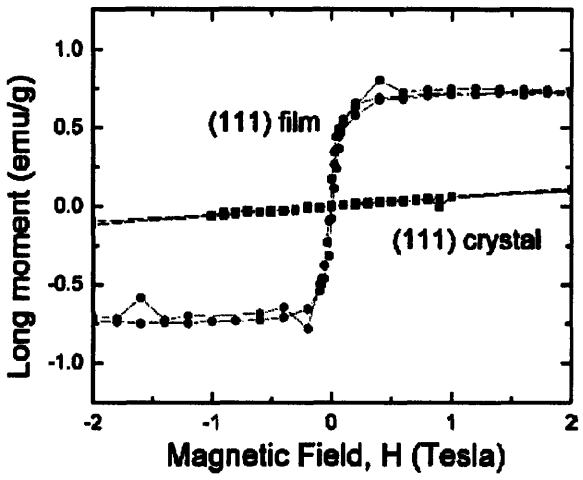

Figure 2-21: *M-H* hysteresis loops for a (111) oriented BFO film (red) and a (111) oriented bulk BFO crystal (black) [24].

Of course, the above data was taken for bulk ceramics. Growing BFO as a film on a substrate which has an epitaxial constraint can also contribute to destruction of the spin cycloid. One group has shown that even in a (111) oriented BFO film, grown on STO (111), where the rhombohedral crystal structure is almost identical to that of the bulk, the epitaxial constraint causes a non-zero remanence and saturation. As shown in Figure 2-21, the BFO film shows actual hysteresis not found in the bulk crystal and has an $M_s = 0.6$ emu/g or 5 emu/cm^3 [24].

2.2.4 Optical and Magneto-Optical Properties

The optical and magneto-optical properties of orthoferrites were examined in the late 60's and early 70's for those with rare-earth atoms on the A-sites. Although it was more difficult to measure absorption in transparent regions due to the difficulty of growing samples thicker than a millimeter with no flux inclusions, many of the rare-earth orthoferrites were shown to possess a transparency window in the near infrared with $\alpha < 0.5$ cm^{-1}.[9] The fact that they all possess this window to some degree can

[9]This result should be compared with that of YIG, which can have $\alpha < 0.03$ cm^{-1}, keeping in mind, however, that the former is simply an upper limit due to experimental limitations and the absorption may be, in fact, much lower.

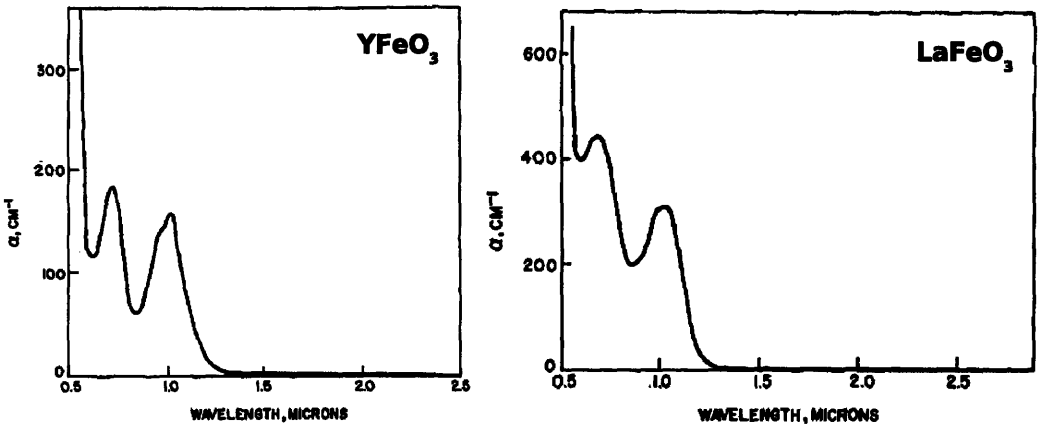

Figure 2-22: Near infrared optical absorption spectra for $YFeO_3$ and $LaFeO_3$ [25].

be attributed to the fact that, as in the garnets, most of the absorption in this region comes from the Fe^{3+} cation and not the rare-earth iron. The absorption spectra for two of the most transparent materials, $YFeO_3$ and $LaFeO_3$, are shown in Figure 2-22 [25].

The Faraday rotation spectra of those rare-earth orthoferrites that were examined are also fairly similar, with the exception of $SmFeO_3$, as shown in Figure 2-23. Once again, this similarity and partial independence of the identity of the rare-earth ion is due to the fact that electric dipole transitions of the Fe^{3+} cation govern Faraday rotation in this regime. $SmFeO_3$ is different than the others because it is the only orthoferrite whose magnetization lies along its a-axis, as opposed to its c-axis. It should be noted that the intrinsic Faraday rotation here (ignoring birefringence) is actually quite high, as that of $YFeO_3$ is about 3 times that of YIG at $\lambda_0 = 1550$ nm [26].

2.2.5 Application in Isolator Devices

There has been almost no recent work done on the Faraday rotation of orthoferrites, especially those grown as thin films. One study, however [27], looked at the related $Ba(Ti,Fe)O_3$ system and optimized it for high Faraday rotation and low loss, i.e. a high magneto-optical figure of merit. As shown in Figure 2-24, an optimal compo-

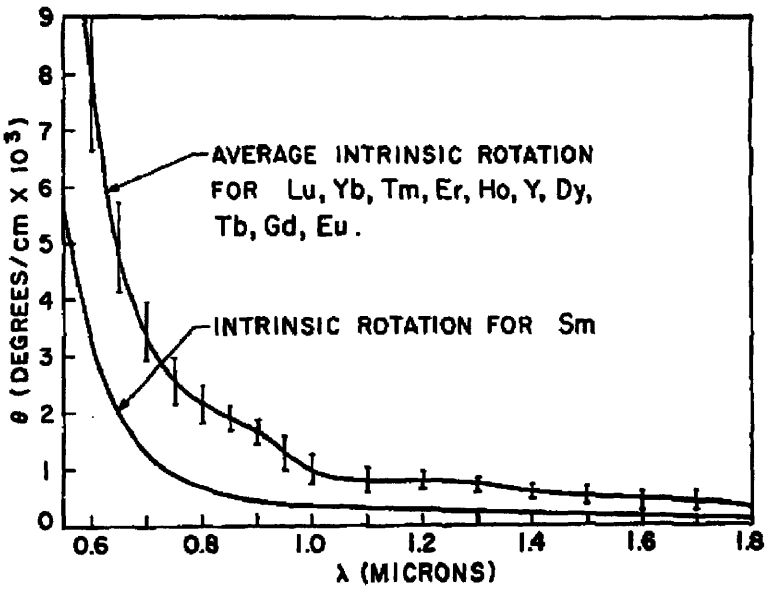

Figure 2-23: Intrinsic Faraday rotation spectra of many rare-earth orthoferrites. The vertical lines are not error bars, but represent the range of those quantities averaged to create the upper line [26].

sition of $BaTi_{0.8}Fe_{0.2}O_3$ was found with a figure of merit of $F_\Theta = 3.7°/\text{dB}$ (or 86°), corresponding to a specific Faraday rotation of 300°/cm and a loss of 81 dB/cm (or 3.5 cm^{-1}).[10] Nevertheless, this Faraday rotation at $\lambda_0 = 1550$ nm is still lower than that of a typical orthoferrite or some of the best garnets (around 800°/cm) with a loss that is one to two orders of magnitude higher. Its figure of merit is therefore an order of magnitude lower than those of the best garnets. There is also some doubt as to what mechanism governs the increasing absorption in this solid solution as a function of Fe content. The paucity of x-ray data in this paper could be hiding the fact that there were hidden Fe clusters or γ-Fe_2O_3 in the films, and the fact that no observable

[10]It will occasionally be useful to convert from dimensionless units of loss k (i.e. the imaginary part of the index of refraction) to loss per unit length α to loss in dB per unit length α_{dB}. The relationship between the first two quantities is simply $\alpha = 4\pi k/\lambda_0$, and we can convert this result to units of dB/length by using

$$\begin{aligned} \alpha_{\text{dB}} &= 10\log_{10}\left(\frac{I}{I_0}\right) = 10\log_{10}\left(\text{e}^{-\alpha z}\right) = -10\alpha z \log_{10}\text{e} \\ \frac{\alpha_{\text{dB}}}{z} &\approx -23.03\alpha \end{aligned}$$

We must keep in mind that α_{dB} is always a negative number because it represents a decay.

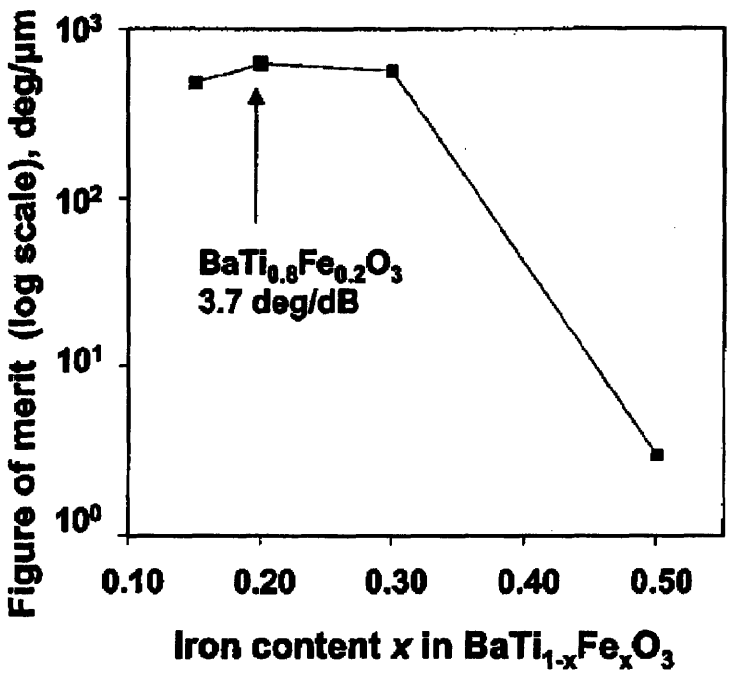

Figure 2-24: Magneto-optical figure of merit (ratio of Faraday rotation to absorption) at $\lambda_0 = 1550$ nm in $BaTi_{1-x}Fe_xO_3$ as a function of x [27].

Faraday rotation was found in samples grown by PLD at $p_{O_2} > 2$ mTorr could be attributed to the fact that, above this critical pressure, γ-Fe_2O_3 does not form and does not contribute to Faraday rotation. Since the Faraday rotation of γ-Fe_2O_3 is $25,000°/cm$ [74], even 1% of the iron oxide phase in the film could cause the measured Faraday rotation at high field. These empirical observations are certainly consistent with previous work and warrant further investigation [27].

Despite the high intrinsic Faraday rotation of the orthoferrites, they are not used in optical isolators, mainly due to their linear birefringent properties. Because most orthoferrites have a low-symmetry crystal structure (e.g. BFO is rhombohedral in the bulk), the indices of refraction and dielectric constants along each of the crystalline axes are not necessarily equal. This causes a phase lag to build up as light propagates through the material which, as will be discussed in greater detail in Section 3.4, limits the total Faraday rotation possible for *any given length* of material. The figure of merit that measures the ratio of Faraday rotation to birefringence χ ($\sin\chi = 1$ for pure Faraday rotation, $\sin\chi = 0$ for pure birefringence) has been measured and is

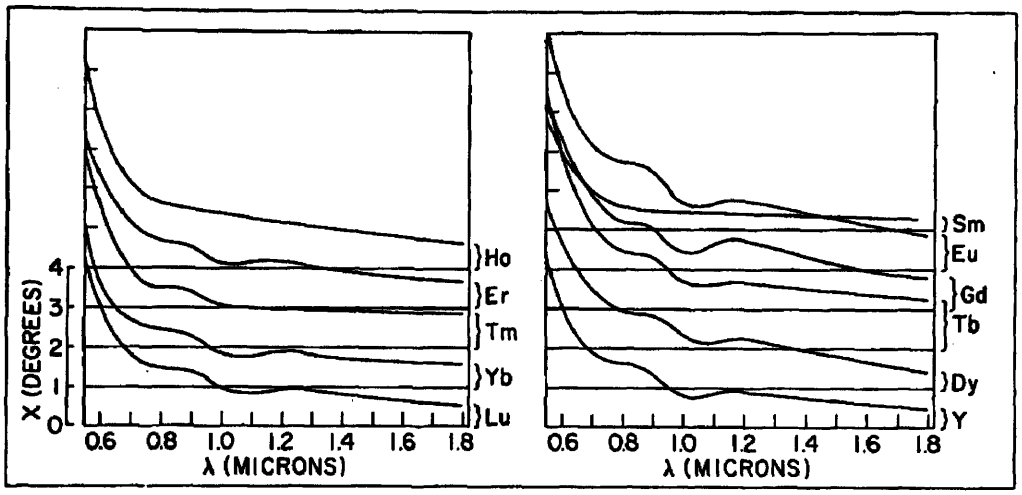

Figure 2-25: χ, a ratio of the intrinsic Faraday rotation (i.e. along the optical axis) to the birefringence ($\sin\chi = 1$ for pure Faraday rotation, $\sin\chi = 0$ for pure birefringence), in units of degrees verses wavelength for several rare-earth orthoferrites. The estimated error in χ is $\pm 0.25°$ and each plot is connected to its origin with brackets [26].

plotted in Figure 2-25 as a function of wavelength for several rare-earth orthoferrites. As we can see from the plot, at $\lambda_0 = 1550$ μm, χ is on the order of 1°, meaning that almost no Faraday rotation can be obtained conventionally in orthoferrites despite their high intrinsic Faraday rotation [26].

Now, this sounds pessimistic. It turns out that not all is lost, though, for we can always align the crystal along one of its optical axes, in which case the birefringence goes to zero. However, in this case the power transmitted drops off proportional to $\cos^2\phi$, where ϕ is the angle between the optical axis and the magnetization direction (usually the c-axis). So, we raise the Faraday rotation, but lose more to attenuation. Thus, our two figures of merit F_Θ and χ are not independent, since raising one may lower the other. Also, although it is easy to rotate a bulk crystal to an arbitrary angle, it is certainly not so easy to grow an orthoferrite epitaxially at an arbitrary angle on a substrate, and values of ϕ for other crystals can be on the order of 50° [26]. Hence, it will take some clever manipulation of crystal structure and device geometry to make these orthoferrites useful in isolators; but it's not impossible!

Chapter 3

The Theory of Faraday Rotation & Electric Dipole Transitions

In this chapter, we will establish a physical basis for Faraday rotation in magnetic oxides by deriving its dependence on the elements of the dielectric tensor. We will then use this result to calculate the magneto-optical figure of merit based on these parameters. We will also comment on how linear birefringence effects the efficacy of an isolator material. After this purely classical treatment, we will then discuss the quantum physics of electric dipole transitions and describe how they are relevant to describing the dielectric tensor elements in question. Finally, we will examine the effect of Bi-substitution in materials containing octahedrally coordinated Fe^{3+} ions and conclude by citing some hopeful predictions for the $BiFeO_3$ system.

3.1 Normal Modes of Propagation

3.1.1 Derivation of the Wave Equation

We begin, as one typically does in classical E&M problems, with Maxwell's equations [28, pg. 330]:

$$\nabla \cdot \boldsymbol{D} = \rho_f \tag{3.1}$$

$$\nabla \cdot \boldsymbol{B} = 0 \tag{3.2}$$

$$\nabla \times \boldsymbol{E} = -\frac{\partial \boldsymbol{B}}{\partial t} \tag{3.3}$$

$$\nabla \times \boldsymbol{H} = \frac{\partial \boldsymbol{D}}{\partial t} + \boldsymbol{J}_f \tag{3.4}$$

where $\boldsymbol{E}$ is the electric field, $\boldsymbol{D}$ is the electric displacement, $\boldsymbol{B}$ is the magnetic field, $\boldsymbol{H}$ is the magnetic intensity, ρ_f is the free charge density, and $\boldsymbol{J}_f$ is the free current density. These equations describe the propagation of electromagnetic radiation in a material of arbitrary complexity.

Our system, fortunately, is not arbitrarily complex. In particular, we can assume that there is no free charge built up, so $\rho_f = 0$. Furthermore, we can assume that our material is a linear dielectric, meaning that we can assume

$$\boldsymbol{D} = \widehat{\epsilon}\boldsymbol{E} \tag{3.5}$$

$$\boldsymbol{B} = \widehat{\mu}\boldsymbol{H} \tag{3.6}$$

$$\boldsymbol{J}_f = \widehat{\sigma}\boldsymbol{E} \tag{3.7}$$

where $\widehat{\epsilon}$ is the dielectric tensor, $\widehat{\mu}$ is the permeability tensor, and $\widehat{\sigma}$ is the conductivity tensor. Eq. (3.5) and Eq. (3.6) are simply the definition of a linear dielectric, while Eq. (3.7) is Ohm's law. Substituting these equations into Eqs. (3.1-3.4), we can derive the following relationships for $\boldsymbol{E}$ and $\boldsymbol{H}$:

$$\nabla \cdot \boldsymbol{E} = 0 \tag{3.8}$$

$$\nabla \cdot \boldsymbol{H} = 0 \tag{3.9}$$

$$\nabla \times \boldsymbol{E} = -\widehat{\mu}\frac{\partial \boldsymbol{H}}{\partial t} \tag{3.10}$$

$$\nabla \times \boldsymbol{H} = \widehat{\epsilon}\frac{\partial \boldsymbol{E}}{\partial t} + \widehat{\sigma}\boldsymbol{E} \tag{3.11}$$

Taking the curl of Eq. (3.10) and subsequently substituting Eq. (3.11) into the re-

sulting equation, we find that

$$\begin{aligned} \nabla \times (\nabla \times \boldsymbol{E}) &= -\widehat{\mu}\frac{\partial(\nabla \times \boldsymbol{H})}{\partial t} \\ \nabla(\nabla \cdot \boldsymbol{E}) - \nabla^2 \boldsymbol{E} &= -\widehat{\mu}\frac{\partial}{\partial t}\left[\widehat{\epsilon}\frac{\partial \boldsymbol{E}}{\partial t} + \widehat{\sigma}\boldsymbol{E}\right] \end{aligned} \tag{3.12}$$

Eq. (3.8) tells us that the first term in Eq. (3.12) is equal to 0. Thus, the latter equation reduces to the familiar electromagnetic wave equation

$$\nabla^2 \boldsymbol{E} - \widehat{\mu}\widehat{\epsilon}\frac{\partial^2 \boldsymbol{E}}{\partial t^2} - \widehat{\mu}\widehat{\sigma}\frac{\partial \boldsymbol{E}}{\partial t} = 0 \tag{3.13}$$

There is a corresponding equation for $\boldsymbol{H}$; but, since the two fields are related by Maxwell's equations, it will suffice just to speak of $\boldsymbol{E}$ from now on.

3.1.2 Plane Wave Solution & Relevant Approximations

We will need a series of approximations and educated guesses to solve the wave equation in Eq. (3.13). The first of these is that, for an isotropic crystal, one only needs $\widehat{\epsilon}$ and $\widehat{\sigma}$ to describe the system. Hence, in Eq. (3.13), we can set $\widehat{\mu} = \mu_0\widehat{1}$, where μ_0 is the permeability of free space and $\widehat{1}$ is the identity tensor [75].

Now, in order to find the eigenfunctions of Eq. (3.13), we make the typical plane wave ansatz for an electromagnetic wave propagating in the z-direction that

$$\boldsymbol{E}(z,t) = \boldsymbol{E}_0 \mathrm{e}^{-i\omega(t-nz/c)}$$

where $i = \sqrt{-1}$, $\boldsymbol{E}_0 = E_0(1, i\zeta, 0)$ is a constant, t is time, ω is the frequency of the wave in free space, c is the speed of light in free space, and n is the index of refraction of the material.[1] In this ansatz, n will be our eigenvalue and will be determined shortly through a dispersion relation. Before we substitute this ansatz into Eq. (3.13), however, we need to provide the forms of $\widehat{\epsilon}$ and $\widehat{\sigma}$. Fortunately, it can be shown that

[1]Typically, in solving these types of differential equations, one assumes a complex $\boldsymbol{E}$ will be a solution. Of course, nothing in the real world is really complex (at least not in the mathematical sense); so, we must keep in mind that, at the end of the day, we must take the real part of any complex quantity left over.

for a so-called "polar geometry" like ours, wherein the applied magnetic field points in the z-direction and we have planar symmetry in the orthogonal directions, and for a crystal with uniaxial symmetry, the most general form of these tensors is [75]

$$\widehat{\epsilon} = \epsilon_0 \begin{pmatrix} \epsilon_d & -ig & 0 \\ ig & \epsilon_d & 0 \\ 0 & 0 & \epsilon_z \end{pmatrix}; \quad \widehat{\sigma} = \sigma_0 \begin{pmatrix} \sigma_d & -is & 0 \\ is & \sigma_d & 0 \\ 0 & 0 & \sigma_z \end{pmatrix} \tag{3.14}$$

where ϵ_0 is the permittivity of free space, σ_0 is a characteristic conductivity (which we will eventually set to 0) and all other quantities are dimensionless functions of ω. Of course, the assumption of uniaxial symmetry in a garnet is an excellent one, but not necessarily in certain orthoferrites which can have rhombohedral, orthorhombic, or monoclinic distortions. In these, the x- and y-diagonal components of these tensors are not necessarily equal. This situation shall be addressed in Section 3.4; but, from here on, let us proceed under the assumption of at least uniaxial symmetry.

Using the uniaxial definitions, and substituting our ansatz into the Eq. (3.13), we see that the x- and y-components, respectively, are

$$\left(\frac{i\omega n}{c}\right)^2 - \mu_0\epsilon_0(\epsilon_d + g\zeta)(-i\omega)^2 - \mu_0\sigma_0(\sigma_d + s\zeta)(-i\omega) = 0 \tag{3.15}$$

$$i\left(\frac{\omega n}{c}\right)^2 \zeta - i\mu_0\epsilon_0(\epsilon_d + g\zeta)(-i\omega)^2 - i\mu_0\sigma_0(\sigma_d + s\zeta)(-i\omega) = 0 \tag{3.16}$$

If we divide the latter equation by i, we realize that the only way these two equations can be equivalent (and they must be because they represent the same physics) is if the arbitrarily defined constant $\zeta = \pm 1$. Also, note that if we wish to compare the size of the final two terms of these equations, we must essentially compare the size of $\epsilon_0\omega$ to σ_0. At our wavelength of interest, $\lambda_0 = 1550$ nm (or $\omega = 2\pi c/\lambda_0 = 1.22 \times 10^{15}$ Hz), and at room temperature, the former term is equal to $1 \times 10^4\ \Omega^{-1}\mathrm{m}^{-1}$ while, for $BiFeO_3$, the latter is equal to $3 \times 10^{-3}\ \Omega^{-1}\ \mathrm{m}^{-1}$ [76]. Considering that we have taken the lower limit on the former term, it must be larger than the latter by at least 7 orders of magnitude. Thus, we are justified in neglecting the conductivity term

henceforth in our calculations. Doing so, Eq. (3.15) becomes

$$-\frac{\omega^2 n_\pm^2}{c^2} + \mu_0\epsilon_0\omega^2(\epsilon_d \pm g) = 0$$
$$n_\pm^2 = \epsilon_d \pm g \tag{3.17}$$

where we have used the fact that $c^2 = 1/\mu_0\epsilon_0$. We have also illustrated the fact that $\zeta = \pm 1$ leads to two solutions to this equation for $n = n_\pm$. These two values are the eigenvalues, while the orthonormal eigenmodes of propagation are[2]

$$\mathbf{e}_\pm = \frac{1}{\sqrt{2}} \begin{pmatrix} 1 \\ \pm i \end{pmatrix} \mathrm{e}^{-i\omega(t - n_\pm z/c)} \tag{3.18}$$

Physically, this result tells us two important pieces of information: (1) the two eigenmodes of the system are right (+) and left (−) circularly polarized light and (2) the index of refraction of the + mode is greater than that of the other and the splitting is a function of g, the off-diagonal component of the dielectric tensor. The second point is very important, since it tells us that the two eigenmodes will have different velocities in a medium where $g \neq 0$. It will turn out that this difference in velocities is the main cause of Faraday rotation.

The final result of this section is that, as we can with any set of orthonormal eigenmodes, we can represent any plane wave in our medium traveling in the z-direction as a linear combination of our eigenmodes, namely

$$\boldsymbol{E}(z,t) \;=\; C_+\mathbf{e}_+ + C_-\mathbf{e}_- \tag{3.19}$$

where $C_\pm$ are constants.

[2]The reader should note that we have dropped the z-term in our vector notation. We have done so because, for a plane wave propagating in the z-direction, E_z is identically 0; hence, we will not concern ourselves with it henceforth.

3.2 Faraday Rotation and Ellipticity

3.2.1 Derivation of General $\boldsymbol{E}$-Field

The $C_{\pm}$ given in Eq. (3.19) have particular values that determine the form of $\boldsymbol{E}$. Finding them really comes down to plugging in the appropriate boundary condition. In this case, the boundary condition is that at $z = 0$, where the light in question enters the medium, the light is linearly polarized arbitrarily in the x-direction. This statement is equivalent to writing

$$\boldsymbol{E}(z=0,t) = E_0 \begin{pmatrix} 1 \\ 0 \end{pmatrix} \mathrm{e}^{-i\omega t} \tag{3.20}$$

where E_0 is the initial magnitude of the field. Substituting the boundary condition in Eq. (3.20) into Eq. (3.19) and solving for the constants tells us that

$$\begin{aligned} C_+ = C_- &= E_0/\sqrt{2} \\ \therefore \quad \boldsymbol{E}(z,t) &= \frac{E_0}{\sqrt{2}}(\mathbf{e}_+ + \mathbf{e}_-) \\ &= \frac{E_0 \mathrm{e}^{-i\omega t}}{2}\left[\begin{pmatrix} 1 \\ i \end{pmatrix} \mathrm{e}^{i\omega n_+ z/c} + \begin{pmatrix} 1 \\ -i \end{pmatrix} \mathrm{e}^{i\omega n_- z/c}\right] \\ &= \frac{E_0 \mathrm{e}^{-i\omega t}}{2}\begin{pmatrix} \mathrm{e}^{i\omega n_+ z/c} + \mathrm{e}^{i\omega n_- z/c} \\ i\mathrm{e}^{i\omega n_+ z/c} - i\mathrm{e}^{i\omega n_- z/c} \end{pmatrix} \end{aligned} \tag{3.21}$$

We shall now employ an algebraic trick to change this equation into a more intuitive form. We will use the identities

$$\begin{aligned} \cos x &= \frac{\mathrm{e}^{ix} + \mathrm{e}^{-ix}}{2} \\ \sin x &= \frac{\mathrm{e}^{ix} - \mathrm{e}^{-ix}}{2i} \end{aligned}$$

as well as the definitions

$$n_0 \equiv \frac{n_+ + n_-}{2}; \quad \Delta n \equiv \frac{n_+ - n_-}{2}$$

We start by factoring out $e^{i\omega n_+ z/2c} e^{i\omega n_- z/2c}$ from the vector in Eq. (3.39). This gives

$$\begin{aligned}
\boldsymbol{E}(z,t) &= \frac{E_0 e^{-i\omega t}}{2} e^{i\omega n_+ z/2c} e^{i\omega n_- z/2c} \begin{pmatrix} e^{i\omega(n_+ - n_-)z/2c} + e^{i\omega(n_- - n_+)z/2c} \\ i e^{i\omega(n_+ - n_-)z/2c} - i e^{i\omega(n_- - n_+)z/c} \end{pmatrix} \\
&= \frac{E_0 e^{-i\omega t}}{2} e^{i\omega n_0 z/c} \begin{pmatrix} e^{i\omega\Delta n z/c} + e^{-i\omega\Delta n z/c} \\ i e^{i\omega\Delta n z/c} - i e^{-i\omega\Delta n z/c} \end{pmatrix} \\
&= E_0 e^{-i\omega t} e^{i\omega n_0 z/c} \begin{pmatrix} \cos(\omega\Delta n z/c) \\ -\sin(\omega\Delta n z/c) \end{pmatrix}
\end{aligned}$$

Thus, when we rearrange terms, we arrive at the final result

$$\boldsymbol{E}(z,t) = E_0 \begin{pmatrix} \cos(\omega\Delta n z/c) \\ -\sin(\omega\Delta n z/c) \end{pmatrix} e^{-i\omega(t - n_0 z/c)} \tag{3.22}$$

Note that in the trivial case where $\Delta n = 0$, this reduces back to the linearly polarized case for all z.

3.2.2 Θ and Ψ in the Transparent Approximation

Let us consider the simplest, non-trivial case of Eq. (3.22) in which Δn is real. At $z = 0$, the wave is polarized in the x-direction. As z increases, though, the y-component becomes non-zero and, at some arbitrary value of z, $\boldsymbol{E}$ will be pointed at an angle θ with respect to the x-axis given by

$$\tan\theta = -\frac{\sin(\omega\Delta n z/c)}{\cos(\omega\Delta n z/c)} = -\tan(\omega\Delta n z/c) = \tan[-(\omega\Delta n z/c)]$$

Therefore, after traveling a distance z, $\boldsymbol{E}$ will have rotated through an angle of $\theta = -\omega\Delta n z/c$. This is the phenomenon of Faraday rotation; the material has essentially

rotated the direction of polarization of our light by θ degrees. Since it is often useful to normalize θ by the distance traveled z, we define a quantity called the *specific* Faraday rotation

$$\Theta \equiv \frac{\theta}{z} = -\frac{\omega \Delta n}{c} \tag{3.23}$$

In reality, however, Δn is almost always complex. Consequently, after traveling a distance z, the initially linearly polarized wave is not linearly polarized, but elliptically polarized with ellipticity ψ. It is possible in a more general way to derive both the Faraday rotation and the ellipticity. In order to do so, it will be useful to think of n_0 and Δn as complex numbers. Of course, this means we must also think of their constituents $n_{\pm}(\epsilon_d, g)$ as complex numbers. Solving for $n_{\pm}$ as a function of n_0 and Δn and using Eq. (3.17), we get

$$n_{\pm} = n_0 \pm \Delta n = \sqrt{\epsilon_d \pm g} \tag{3.24}$$

which means that n_0 and Δn must be

$$n_0 = \frac{1}{2}\left(\sqrt{\epsilon_d + g} + \sqrt{\epsilon_d - g}\right) = \frac{\sqrt{\epsilon_d}}{2}\left(\sqrt{1+Q} + \sqrt{1-Q}\right) \tag{3.25}$$

$$\Delta n = \frac{1}{2}\left(\sqrt{\epsilon_d + g} - \sqrt{\epsilon_d - g}\right) = \frac{\sqrt{\epsilon_d}}{2}\left(\sqrt{1+Q} - \sqrt{1-Q}\right) \tag{3.26}$$

where the constant $Q \equiv g/\epsilon_d \ll 1$ in most situations [50, pg. 22]. We may therefore expand the square root terms in Eqs. (3.25-3.26) in a Taylor series to first order in Q, as follows:

$$n_0 \approx \frac{\sqrt{\epsilon_d}}{2}\left(1 + \frac{Q}{2} + 1 - \frac{Q}{2}\right) = \sqrt{\epsilon_d} \tag{3.27}$$

$$\Delta n \approx \frac{\sqrt{\epsilon_d}}{2}\left(1 + \frac{Q}{2} - 1 + \frac{Q}{2}\right) = \frac{\sqrt{\epsilon_d}}{2} Q \tag{3.28}$$

To seek the complex forms of these variables, we let $n_0 = n_0' + i n_0''$, $\Delta n = \Delta n' + i \Delta n''$, $\epsilon_d = \epsilon_d' + i\epsilon_d''$, and $g = g' + ig''$, wherein all primed quantities are real numbers. Let

us begin with n_0. Plugging the relevant definitions into Eq. (3.27) and squaring it, we get

$$n_0'^2 + n_0''^2 + 2in_0'n_0'' = \epsilon_d' + i\epsilon_d''$$

This single equation is really two: one for the real component and one for the imaginary. Solving them simultaneously for n_0' and n_0'' gives, for the latter,[3]

$$n_0'' = \sqrt{\frac{\epsilon_d'}{2}}\sqrt{1-\sqrt{1-\left(\frac{\epsilon_d''}{\epsilon_d'}\right)^2}} \tag{3.29}$$

At a wavelength where there is little absorption (e.g. at 1550 nm in some garnets and orthoferrites), we can make the approximation $\epsilon_d''/\epsilon_d' \ll 1$. In fact, in such a wavelength regime, it is often common to assume [50, pg. 35]

$$|\epsilon_d'| \gg \max(|\epsilon_d''|, |g'|, |g''|) \tag{3.30}$$

In this approximation, we can Taylor expand Eq. (3.29) to first order in ϵ_d''/ϵ_d' to get

$$n_0'' \approx \sqrt{\frac{\epsilon_d'}{2}}\sqrt{1-1+\frac{1}{2}\left(\epsilon_d''/\epsilon_d'\right)^2} = \frac{\epsilon_d''}{2\sqrt{\epsilon_d'}} \tag{3.31}$$

We can solve for n_0' in a similar way since

$$n_0' = \frac{\epsilon_d''}{2n_0''} \approx \frac{\epsilon_d''}{2} \times \frac{2\sqrt{\epsilon_d'}}{\epsilon_d''} = \sqrt{\epsilon_d'} \tag{3.32}$$

So, in summary, we find that the complex form of n_0, as a function of the dielectric tensor elements, is to first order

$$n_0 = \sqrt{\epsilon_d'} + i\frac{\epsilon_d''}{2\sqrt{\epsilon_d'}} \tag{3.33}$$

[3]Solving for n_0'' involves finding the roots of a fourth-order polynomial, for which there are obviously four solutions. Two of these are negative and are therefore non-physical. We choose the solution of the remaining two for which $n_0'' = 0$ when $\epsilon_d'' = 0$ because n_0 should be real when ϵ_d is real.

We can solve for the real and imaginary parts of Δn in a similar fashion—by squaring both sides of Eq. (3.28) to get

$$\Delta n'^2 + \Delta n''^2 + 2i\Delta n'\Delta n'' = \frac{1}{4}\left[(\epsilon_d' + i\epsilon_d'')(Q'^2 + Q''^2 + 2iQ'Q'')\right]$$

where we have written $Q = Q' + iQ''$ as a complex number as well. After we group terms, we must simultaneously solve the two equations

$$\Delta n'^2 + \Delta n''^2 = \frac{1}{4}\left(\epsilon_d' Q'^2 + \epsilon_d' Q''^2 - 2\epsilon_d'' Q'Q''\right) \tag{3.34}$$

$$2\Delta n'\Delta n'' = \frac{1}{4}\left(2\epsilon_d' Q'Q'' + \epsilon_d'' Q'^2 + \epsilon_d'' Q''^2\right) \tag{3.35}$$

This would be an algebraic mess to solve exactly. Fortunately, we may employ the approximation given in Eq. (3.30), which also tells us that $|\epsilon_d'| \gg \max(|Q'|, |Q''|)$. To do so, we factor out ϵ_d' from the right hand side of Eqs. (3.34-3.35) and then keep the terms which contain the fewest small factors, as follows:

$$\begin{aligned}\Delta n'^2 + \Delta n''^2 &= \frac{\epsilon_d'}{4}\left(Q'^2 + Q''^2 - 2\frac{\epsilon_d''}{\epsilon_d'}Q'Q''\right) \\ &\approx \frac{\epsilon_d'}{4}\left(Q'^2 + Q''^2\right) \qquad (3.36)\\ 2\Delta n'\Delta n'' &= \frac{\epsilon_d'}{4}\left(2Q'Q'' + \frac{\epsilon_d''}{\epsilon_d'}Q'^2 + \frac{\epsilon_d''}{\epsilon_d'}Q''^2\right) \\ &\approx \frac{\epsilon_d'}{4}\left(2Q'Q''\right) = \frac{\epsilon_d'}{2}Q'Q'' \qquad (3.37)\end{aligned}$$

Solving the above system of equations to leading order gives[4]

$$\Delta n = \frac{\sqrt{\epsilon_d'}}{2}Q' + i\frac{\sqrt{\epsilon_d'}}{2}Q'' \tag{3.38}$$

[4]Actually, this system can also give the solution $n = (\sqrt{\epsilon_d'}/2)(Q'' + iQ')$, but this result is incorrect. If we, instead, solve for Δn without squaring both sides of Eq. (3.28) and apply the relevant approximations, we get the answer in Eq. (3.38) unambiguously. However, doing so is more difficult since it requires taking the square root of a complex number.

We shall now return to Eq. (3.22) to see how the complexity of n_0 and Δn affect $\boldsymbol{E}$:

$$\boldsymbol{E}(z,t) = E_0 \begin{pmatrix} \cos[\omega(\Delta n' + i\Delta n'')z/c] \\ -\sin[\omega(\Delta n' + i\Delta n'')z/c] \end{pmatrix} \mathrm{e}^{-i\omega[t-(n_0'+in_0'')z/c]} \tag{3.39}$$

We can use the identities

$$\begin{aligned} \cos(a+ib) &= \cos a \cosh b - i \sin a \sinh b \\ \sin(a+ib) &= \sin a \cosh b + i \cos a \sinh b \end{aligned}$$

to re-write the vector in Eq. (3.39), which for brevity we shall call $\boldsymbol{v}$, as

$$\boldsymbol{v} = \begin{pmatrix} \cos(\gamma\Delta n')\cosh(\gamma\Delta n'') - i\sin(\gamma\Delta n')\sinh(\gamma\Delta n'') \\ -\sin(\gamma\Delta n')\cosh(\gamma\Delta n'') - i\cos(\gamma\Delta n')\sinh(\gamma\Delta n'') \end{pmatrix}$$

where $\gamma \equiv \omega z/c$. This means that

$$\boldsymbol{E}(\gamma,t) = E_0 \mathrm{e}^{-\gamma n_0''} \boldsymbol{v} \mathrm{e}^{-i(\omega t - \gamma n_0')}$$

Now that we have described the $\boldsymbol{E}$ field, we must calculate the Faraday rotation θ and the ellipticity ψ. These may be obtained by examining the quantity $\chi \equiv E_y/E_x = v_y/v_x$ because [50, pg. 29]

$$\tan 2\theta = \frac{2}{1-|\chi|^2}\mathrm{Re}\{\chi\} \tag{3.40}$$

$$\sin 2\psi = \frac{2}{1+|\chi|^2}\mathrm{Im}\{\chi\} \tag{3.41}$$

Using the definition, we find that

$$\chi = -\frac{\sin(\gamma\Delta n')\cosh(\gamma\Delta n'') + i\cos(\gamma\Delta n')\sinh(\gamma\Delta n'')}{\cos(\gamma\Delta n')\cosh(\gamma\Delta n'') - i\sin(\gamma\Delta n')\sinh(\gamma\Delta n'')}$$

When we multiply the top and bottom by the complex conjugate of the denominator,

we get

$$\chi = \frac{-\sin(\gamma\Delta n')\cos(\gamma\Delta n') - i\sinh(\gamma\Delta n'')\cosh(\gamma\Delta n'')}{\cos^2(\gamma\Delta n')\cosh^2(\gamma\Delta n'') + \sin^2(\gamma\Delta n')\sinh^2(\gamma\Delta n'')}$$

To make the following calculation simpler, we define the denominator of the right hand side of this equation to be D; thus,

$$\begin{aligned} |\chi|^2 &= \frac{1}{D^2}\left[\sin^2(\gamma\Delta n')\cos^2(\gamma\Delta n') + \sinh^2(\gamma\Delta n'')\cosh^2(\gamma\Delta n'')\right] \\ \tan 2\theta &= \frac{2[-\sin(\gamma\Delta n')\cos(\gamma\Delta n')]/D}{1 - [\sin^2(\gamma\Delta n')\cos^2(\gamma\Delta n') + \sinh^2(\gamma\Delta n'')\cosh^2(\gamma\Delta n'')]/D^2} \\ &= -\frac{2\sin(\gamma\Delta n')\cos(\gamma\Delta n')D}{D^2 - \sin^2(\gamma\Delta n')\cos^2(\gamma\Delta n') + \sinh^2(\gamma\Delta n'')\cosh^2(\gamma\Delta n'')} \end{aligned}$$

After a great amount of algebraic simplification, this equation reduces to the surprisingly simple result

$$\tan 2\theta = -\tan 2\gamma\Delta n' = \tan(-2\gamma\Delta n')$$

This equation tells us that $\theta = -\gamma\Delta n'$, so we must simply plug back into the equation our definition of γ and the result from Eq. (3.38), to get

$$\begin{aligned} \theta &= -\frac{\omega z}{c}\Delta n' = -\frac{\omega z}{c} \times \frac{\sqrt{\epsilon'_d}}{2}Q' \\ \Theta &= \frac{\theta}{z} = -\frac{\omega}{2c}\sqrt{\epsilon'_d}Q' = -\frac{\omega}{2c}\frac{g'}{\sqrt{\epsilon'_d}} \end{aligned} \tag{3.42}$$

where we have used the fact that $Q' \approx g'/\epsilon'_d$ when ϵ'_d is much greater than the other tensor elements.

Now, the only remaining problem is to find the ellipticity from Eq. (3.41), as follows:

$$\begin{aligned} \sin 2\psi &= \frac{2[-\sinh(\gamma\Delta n'')\cosh(\gamma\Delta n'')]/D}{1 - [\sin^2(\gamma\Delta n')\cos^2(\gamma\Delta n') + \sinh^2(\gamma\Delta n'')\cosh^2(\gamma\Delta n'')]/D^2} \\ &= \frac{-2\sinh(\gamma\Delta n'')\cosh(\gamma\Delta n'')D}{D^2 - \sin^2(\gamma\Delta n')\cos^2(\gamma\Delta n') + \sinh^2(\gamma\Delta n'')\cosh^2(\gamma\Delta n'')} \end{aligned}$$

After simplifying this equation, we get another simple result:

$$\begin{aligned} \sin 2\psi &= -\tanh(2\gamma\Delta n'') \\ \psi &= -\frac{1}{2}\sin^{-1}\left[\tanh(2\gamma\Delta n'')\right] \end{aligned} \tag{3.43}$$

This result, however, can not be solved analytically. Fortunately, some illuminating approximations can be made. We can use a Taylor series approximation to first order to describe the function $\sin^{-1}(\tanh\delta)$ as long as $\delta < 1/2$. In this regime,

$$\sin^{-1}(\tanh\delta) \approx \delta$$

which would make our calculations a lot simpler. At $\lambda_0 = 1550$ nm and $z = 1$ μm (a typical length scale), $\gamma \approx 8$. $\Delta n''$, however, is typically a couple orders of magnitude less than 1, so $\gamma\Delta n''$ is most likely less than $1/2$, allowing us to use the above Taylor approximation. When we apply it to Eq. (3.43) and use Eq. (3.38) as before, we get

$$\begin{aligned} \psi &\approx -\frac{2\gamma\Delta n''}{2} = -\frac{\omega z}{c} \times \frac{\sqrt{\epsilon_d'}}{2} Q'' \\ \Psi &\approx \frac{\psi}{z} = -\frac{\omega}{2c}\sqrt{\epsilon_d'}Q'' = -\frac{\omega}{2c}\frac{g''}{\sqrt{\epsilon_d'}} \end{aligned} \tag{3.44}$$

So, from Eqs. (3.42) and (3.44), we have the specific Faraday rotation Θ and ellipticity Ψ as a function of the dielectric tensor elements.

3.3 Magneto-Optical Figure of Merit

In designing a magneto-optical isolator material, one is not only concerned about maximizing its Faraday rotation, but also in minimizing its loss. Therefore, we attempt to maximize a Faraday rotation figure of merit defined as

$$F_\Theta = \frac{|\Theta|}{\max(\alpha_\pm)} \tag{3.45}$$

where $\alpha_\pm$ are the loss coefficients of the right and left circularly polarized modes, respectively. It is defined to be part of the exponential prefactor to the eigenmode $\mathbf{e}_\pm$ in the equation for $\boldsymbol{E}$. This prefactor has the form $\mathrm{e}^{-(\alpha_\pm/2)z}$, so $\alpha_\pm$ is positive and has units of inverse length.[5] The reason we take the maximum of these two in F_Θ is because whichever mode is more attenuated will determine the maximum possible amplitude of a linearly polarized wave exiting the material after interacting with a polarizing filter.

To find $\alpha_\pm$, we must seek a form of Eq. (3.39) which expresses $\boldsymbol{E}$ in terms of its eigenmodes $\mathbf{e}_\pm$ given in Eq. (3.18). In other words, for some constants $A_\pm$,

$$\begin{aligned} E_0\boldsymbol{v}\mathrm{e}^{-\gamma n_0''}\mathrm{e}^{-i\omega t}\mathrm{e}^{i\gamma n_0'} &= A_+\mathbf{e}_+ + A_-\mathbf{e}_- \\ &= \frac{\mathrm{e}^{-i\omega t}}{\sqrt{2}}\begin{pmatrix} A_+\mathrm{e}^{i\gamma(n_0+\Delta n)} + A_-\mathrm{e}^{i\gamma(n_0-\Delta n)} \\ iA_+\mathrm{e}^{i\gamma(n_0+\Delta n)} - iA_-\mathrm{e}^{i\gamma(n_0-\Delta n)} \end{pmatrix} \\ \sqrt{2}E_0\boldsymbol{v} &= \begin{pmatrix} A_+\mathrm{e}^{i\gamma\Delta n'}\mathrm{e}^{-\gamma\Delta n''} + A_-\mathrm{e}^{-i\gamma\Delta n'}\mathrm{e}^{+\gamma\Delta n''} \\ iA_+\mathrm{e}^{i\gamma\Delta n'}\mathrm{e}^{-\gamma\Delta n''} - iA_-\mathrm{e}^{-i\gamma\Delta n'}\mathrm{e}^{+\gamma\Delta n''} \end{pmatrix} \end{aligned}$$

Solving for $A_\pm$, not surprisingly, yields $A_\pm = E_0/2$, as specified by the boundary condition. This means that

$$\begin{aligned} \boldsymbol{E}(z,t) &= \frac{E_0\mathrm{e}^{-i\omega t}}{2\sqrt{2}}\left[\begin{pmatrix} 1 \\ i \end{pmatrix}\mathrm{e}^{i\omega(n_0+\Delta n)z/c} + \begin{pmatrix} 1 \\ -i \end{pmatrix}\mathrm{e}^{i\omega(n_0-\Delta n)z/c}\right] \\ &= \frac{E_0\mathrm{e}^{-i\omega t}}{2\sqrt{2}}\begin{pmatrix} 1 \\ i \end{pmatrix}\mathrm{e}^{-\omega(n_0''+\Delta n'')z/c}\mathrm{e}^{i\omega(n_0'+\Delta n')z/c} \\ &+ \frac{E_0\mathrm{e}^{-i\omega t}}{2\sqrt{2}}\begin{pmatrix} 1 \\ -i \end{pmatrix}\mathrm{e}^{-\omega(n_0''-\Delta n'')z/c}\mathrm{e}^{i\omega(n_0'-\Delta n')z/c} \end{aligned} \tag{3.46}$$

By inspection of Eq. (3.46), we see that

$$\alpha_\pm = \frac{2\omega}{c}(n_0'' \pm \Delta n'') = \frac{\omega}{c}\sqrt{\epsilon_d'}\left(\frac{\epsilon_d''}{\epsilon_d'} \pm \frac{g''}{\epsilon_d'}\right) \tag{3.47}$$

[5] We define $\alpha_\pm/2$ to be the prefactor because the intensity of the electromagnetic wave is proportional to $|\boldsymbol{E}|^2 \propto \mathrm{e}^{-\alpha_\pm z}$.

Because $\alpha_+ > \alpha_-$ in this case, we choose the former to be the denominator of F_Θ. Thus, combining Eq. (3.42) with Eq. (3.47) and using the definition in Eq. (3.45), we arrive at the result

$$\begin{aligned} F_\Theta &= \frac{\omega}{2c}\frac{|g'|}{\sqrt{\epsilon'_d}} \times \frac{c}{\omega\sqrt{\epsilon'_d}}\left(\frac{\epsilon''_d}{\epsilon'_d} + \frac{g''}{\epsilon'_d}\right)^{-1} \\ &= \frac{|g'|}{2\epsilon'_d\left(\frac{\epsilon''_d}{\epsilon'_d} + \frac{g''}{\epsilon'_d}\right)} = \frac{|g'|}{2(\epsilon''_d + g'')} \end{aligned} \tag{3.48}$$

Eq. (3.48) is an elegant and simple expression for the Faraday rotation magneto-optical figure of merit F_Θ as a function of the components of the dielectric tensor. It implies that a good optical isolator will have a large value of g', but small values of ϵ''_d and g''. Furthermore, since g' and g'' are linearly dependent on M, the magnitude of the magnetization in the material, we see that F_Θ has an upper, asymptotic limit as $M \to \infty$. This limit makes sense since applying an infinite bias field to the material should not increase the figure of merit after saturation of the magnetization.

3.4 A Comment on Linear Birefringence

The magneto-optical figure of merit F_Θ in Eq. (3.48) has been derived under the assumption of at least uniaxial symmetry. In the case of the orthoferrites, this assumption may or may not be valid; and, in the case of rhombohedral or monoclinic $BiFeO_3$ (BFO),[6] it is probably not. In general, for a material like BFO, we need to write the dielectric tensor $\widehat{\epsilon}$ like

$$\widehat{\epsilon} = \epsilon_0 \begin{pmatrix} \epsilon_{d1} & -ig & 0 \\ ig & \epsilon_{d2} & 0 \\ 0 & 0 & \epsilon_z \end{pmatrix} \tag{3.49}$$

where $\epsilon_{d1} \neq \epsilon_{d2}$. This is the definition of linear, biaxial birefringence. Following a similar analysis to the above, it can be shown that, under the assumption of zero

[6]See previous chapter for discussion of BFO crystal structure.

absorption (i.e. all dielectric constants are real) and given the boundary condition in Eq. (3.20), the spatial components of $\boldsymbol{E}$ are

$$E_x(z)/E_0 = \cos(\delta z/2) - i\cos\chi\sin(\delta z/2) \tag{3.50}$$

$$E_y(z)/E_0 = \sin\chi\sin(\delta z/2) \tag{3.51}$$

where

$$\delta = \bar{k}_+ - \bar{k}_-; \qquad k_\pm^2 = (1/2)\omega^2\mu_0\left[(\epsilon_{d1}+\epsilon_{d2}) \pm \sqrt{(\epsilon_{d1}-\epsilon_{d2})^2+4g^2}\right]$$

$$\cos\chi = \frac{1-\xi^2}{1+\xi^2}; \qquad \sin\chi = \frac{2\xi}{1+\xi^2}$$

$$\xi = \frac{2g}{-(\epsilon_{d1}-\epsilon_{d2}) + \sqrt{(\epsilon_{d1}-\epsilon_{d2})^2+4g^2}}$$

Note that χ is defined differently here than in the last section. Essentially, the birefringence a material like BFO creates a situation in which the normal modes of propagation are no longer circularly polarized waves, but elliptically polarized waves governed by wavenumbers $\bar{k}_\pm$. There will therefore be a phase lag per unit length between E_x and E_y equal to δ just from the birefringence itself. χ on the other hand is a useful parameter that relates the strength of the Faraday rotation to that of the birefringence. In other words, $\sin\chi = 1$ for a pure Faraday rotation with no birefringence and $\sin\chi = 0$ for a purely birefringent medium with no Faraday rotation [77].

Eqs. (3.50-3.51) imply a disturbing reality for those wishing to use BFO as an isolator. Firstly, these equations show a periodic dependence of the angle of polarization on z, the length of propagation into the material. This behavior differs greatly from that of a material with zero birefringence, where Faraday rotation is linearly proportional to z and, hence, a rotation per unit length Θ can be defined. In addition, the latter equation implies that the maximum value of E_y/E_0, achieved when δz is an odd multiple of π, is $\sin\chi$. To achieve the 45° of rotation necessary in a conventional optical isolator, one therefore needs $\sin\chi \geq 1/\sqrt{2}$ or $\chi \geq 45°$. This requirement places a restriction on the allowed values of $\epsilon_{d1} - \epsilon_{d2}$, which is the main

determiner of ξ and therefore the main determiner of χ. Specifically, in order to be able to achieve 45° of isolation, we need $\epsilon_{d1} - \epsilon_{d2} \leq 2g$.[7] As previously stated, g is typically a smaller number, usually much less than the diagonal terms. Therefore, the restriction imposed by birefringence can be a very powerful one and must be overcome in order to use a biaxially birefringent material in an isolator. In fact, in the absence of any clever way of combating the birefringence, this result implies that F_Θ is truly irrelevant when $\sin\chi$ is small because even a powerful isolator several meters long will never be able to rotate the light to a full 45°. Consequently, when contemplating figures of merit, it makes the most sense to consider F_Θ and χ together.

As mentioned in the previous chapter, it is possible to eliminate birefringence by sending light along one of the crystal's optical axis. However, we pay the price for doing so since attenuation leaves us with only $\cos^2\phi$ of the transmitted power, where ϕ is the angle between the optical axis and the magnetization direction. Thus, there is an inherent tradeoff between F_Θ and χ that must be overcome. An excellent analysis of the interaction of Faraday rotation and birefringence in orthoferrites specifically can be found in [78].

3.5 Electric Dipole Transitions

What makes Eq. (3.48) so interesting is that, because the dielectric tensor elements are all functions of ω, the equation provides the relationship between the figure of merit of an optical isolator and its operating frequency. In theory, if one had enough information about the dielectric constants, one could find the optimal ω by maximizing F_Θ. Moreover, it is sufficient to simply know either g' or g'' because they are related to each other via the Kramers-Kronig dispersion relations

[7] This result can be obtained by setting $\sin\chi = 1/\sqrt{2}$ and solving for $\epsilon_{d1} - \epsilon_{d2}$ in the equations of their definition.

$$g'(\omega) = \frac{2}{\pi} P \int_0^\infty \frac{\widetilde{\omega} g''(\widetilde{\omega})}{\widetilde{\omega}^2 - \omega^2} \mathrm{d}\widetilde{\omega} \tag{3.52}$$

$$g''(\omega) = -\frac{2\omega}{\pi} P \int_0^\infty \frac{g'(\widetilde{\omega})}{\widetilde{\omega}^2 - \omega^2} \mathrm{d}\widetilde{\omega} \tag{3.53}$$

where $\widetilde{\omega}$ is a dummy variable and P is the so-called Cauchy principal value. The latter is defined by

$$P \oint f(\widetilde{\omega}) \mathrm{d}\widetilde{\omega} = \lim_{\delta \to 0} \left\{ \int_A^{\omega - \delta} f(\widetilde{\omega}) \mathrm{d}\widetilde{\omega} + \int_{\omega + \delta}^A f(\widetilde{\omega}) \mathrm{d}\widetilde{\omega} \right\} \tag{3.54}$$

where the closed path integral indicates that the integral is taken on a closed path in the complex plane which excludes the singularity at $\widetilde{\omega} = \omega$ and A is an indicative value on that path [79, pgs. 613-6]. So, if complex analysis does not frighten you, the problem of determining F_Θ really boils down to knowing $\epsilon_d''(\omega)$ and either $g'(\omega)$ or $g''(\omega)$.

The question remains, however: what physically determines ϵ_d and g? These are quantities we can measure directly, but it is also important to understand the physics that gives rise to their existence. Because the physics governing ϵ_d and g is inherently very complicated and quantum mechanical, before simply stating the results, we will delve into a simple, yet informative example pulled from classical electrodynamics.

3.5.1 A Classical, Illustrative Example

As an approximation of an electron bound to an atom, let us consider the arrangement shown in Figure 3-1.[8] In this diagram, a charge bound with a linear restoring force associated with constant k_{spring} is subjected to an incoming electromagnetic wave. Let us assume that the wave has frequency ω and amplitude E_0, while the charge has mass m and charge q and experiences a damping force proportional to its velocity, with constant of proportionality $m\gamma$. Hence, we can write Newton's second law for the displacement of the particle x as

[8] This example is taken from [28, pgs. 399-404].

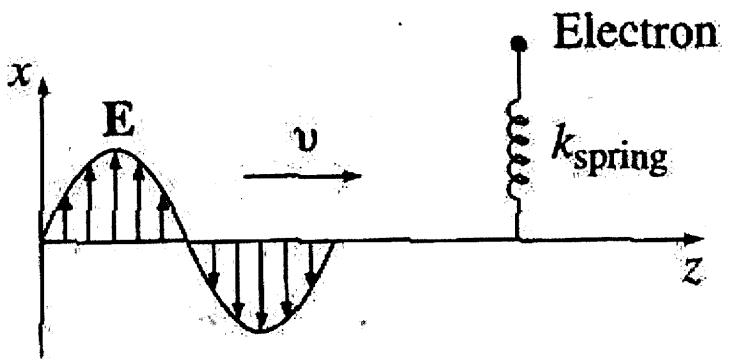

Figure 3-1: Illustration for a classical electrodynamics problem describing the frequency dependence of $\widehat{\epsilon}$ [28].

$$\begin{aligned} m\frac{\mathrm{d}^2x}{\mathrm{d}t^2} &= F_{\text{total}} = F_{\text{binding}} + F_{\text{damping}} + F_{\text{driving}} \\ &= -k_{\text{spring}}x - m\gamma\frac{\mathrm{d}x}{\mathrm{d}t} + qE_0\mathrm{e}^{-i\omega t} \end{aligned} \tag{3.55}$$

Using the definition of the resonant frequency $\omega_0 \equiv \sqrt{k_{\text{spring}}/m}$, we can write Eq. (3.55) as

$$\frac{\mathrm{d}^2x}{\mathrm{d}t^2} + \gamma\frac{\mathrm{d}x}{\mathrm{d}t} + \omega_0^2 x = \frac{q}{m}E_0\mathrm{e}^{-i\omega t}$$

Because, in the steady state, the system must oscillate at the driving frequency, we substitute the ansatz $x(t) = x_0\mathrm{e}^{-i\omega t}$ into this equation and solve for x_0 to get

$$x_0 = \frac{q/m}{\omega^2 - \omega^2 - i\gamma\omega}E_0$$

The dipole moment of this charge is simply $p(t) = qx(t)$. In a system where there are f_j charges with resonant frequency ω_j and damping γ_j, in which there are N of these "molecules" per unit volume and each charge has identical charge q and mass m, we can therefore write the polarization vector $\boldsymbol{P}$ as

$$\boldsymbol{P} = \frac{Nq^2}{m}\left(\sum_j \frac{f_j}{\omega_j^2 - \omega^2 - i\gamma_j\omega}\right)\boldsymbol{E} \tag{3.56}$$

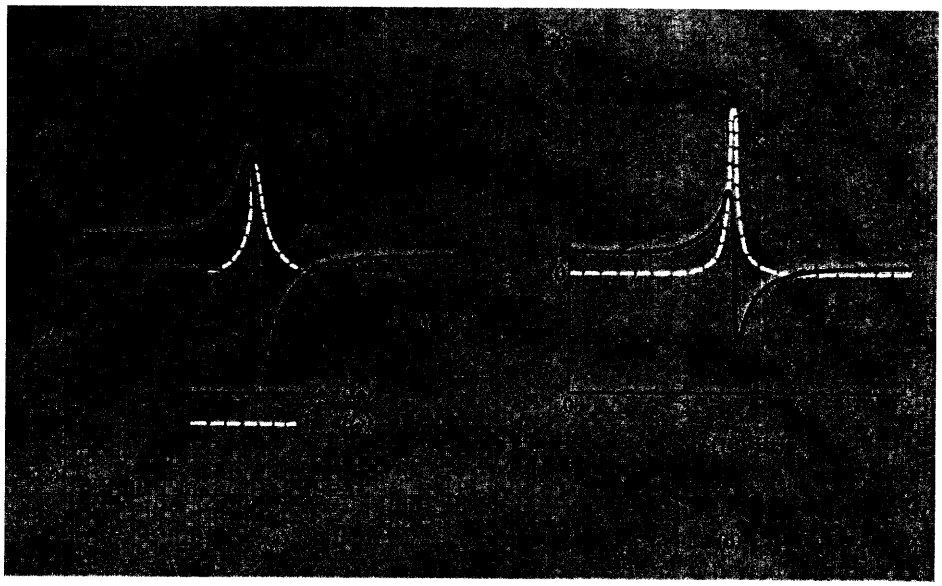

Figure 3-2: Real and imaginary parts of the dielectric constant ϵ_d for (a) ZnS and (b) KCl [29, pg. 552].

In this isotropic case, the dielectric tensor $\widehat{\epsilon}$ is reduced to a scalar $\epsilon = \epsilon_0\epsilon_d$, but nevertheless can be defined in the usual way as $\boldsymbol{P} = \epsilon_0(\epsilon_d + 1)\boldsymbol{E}$.[9] This means that

$$\begin{aligned} \epsilon_d(\omega) &= 1 + \frac{Nq^2}{m\epsilon_0}\sum_j \frac{f_j}{\omega_j^2 - \omega^2 - i\gamma_j\omega} \\ &= 1 + \frac{Nq^2}{m\epsilon_0}\sum_j f_j \frac{\omega_j^2 - \omega^2 + i\gamma_j\omega}{(\omega_j^2 - \omega^2)^2 + \gamma_j^2\omega^2} \end{aligned} \tag{3.57}$$

is the equation for the dielectric constant as a function of frequency. Taking the real and imaginary parts of this equation gives information about the index of refraction and loss coefficients of a given material, respectively. As shown in Figure 3-2 for ZnS and KCl, the real part has an inflection point at the resonant frequency while the imaginary part goes through a maximum. The latter behavior is colloquially known as an absorption peak.

[9]Note that in this case there are no off-diagonal components of $\widehat{\epsilon}$ (i.e. $g = 0$), so we have simply used ϵ_d as the relative dielectric constant.

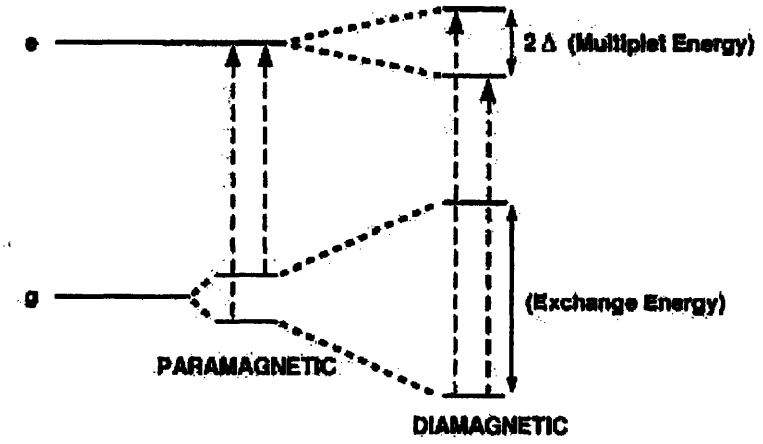

Figure 3-3: Depiction of transitions for the paramagnetic and diamagnetic cases, and indication of the origin of level splittings in each case [30].

3.5.2 Exact Equations of the Dielectric Constants

The electron's true, quantum mechanical interaction with an electromagnetic field is somewhat similar to the above classical approximation. Instead of an charged particle attached to a spring, though, we have one, or several, electrons bound to a nucleus and subjected to a local crystal field. Other electromagnetic forces, such as external fields and spin-orbit coupling, may also exert forces on the electrons in question. Furthermore, just as the charged particle in the classical example can exist in a variety of vibrational states, each with a different value of ω, so too can the quantum mechanical electron. The main difference between the two situations is that the classical particle can take on any energetic state, while the quantum mechanical one is restricted to discrete levels. In garnet materials at near infrared wavelengths, as well as in orthoferrites, we are interested in one type of transition in particular, the electric dipole transition. It is the quantum mechanical analogue of the above description of a classical interaction with an electromagnetic field. There are two main types of electric dipole transitions: diamagnetic and paramagnetic.[10] The former occurs between a singlet ground state, which has been produced by superexchange field quenching of

[10]These names actually have nothing to do with magnetism, but simply refer to the fact that, like their namesake magnetic effects, they either have a temperature dependence (paramagnetic) or do not (diamagnetic).

the spin degeneracy (precluding the Zeeman splitting), and an excited state which has been split by spin-orbit coupling [30]. Before saturation, the splitting is therefore proportional to an applied magnetic field, insofar as the magnetic field lines up the spins in the material and maximizes the spin-orbit coupling. Although the excited state has been split, however, the probability of a transition from the ground state to either excited state is the same.

In contrast, the paramagnetic transition is characterized by a singlet excited state with a ground state split by the Zeeman effect. Whereas in the diamagnetic case the degeneracy of these ground states is quenched by superexchange, in this case, they are populated according to the temperature-dependant Boltzmann distribution. Therefore, the probability of transition to the excited state (also temperature dependent) depends on where the electron lies energetically within the Boltzmann distribution. These transition probabilities are encoded in the so-called oscillator strengths f of the transitions. Rigorously, the oscillator strength is defined as

$$f = \frac{m\omega_0}{h}\langle g|x|e\rangle^2 \tag{3.58}$$

where x is the electric dipole operator and is sensitive to the magnetization through spin-orbit coupling. $\langle g|$ and $|e\rangle$ represent the ground and excited states, respectively. Although f is different for right- and left-polarized light in the paramagnetic case, it is the same for each polarization in the diamagnetic one. The schematic difference between the two types of transitions is depicted in Figure 3-3, while their resulting dispersion curves are displayed in Figure 3-4.

In this thesis, we shall be exclusively interested in transitions of the diamagnetic type since these are the type that give rise to the giant Faraday rotation observed in iron garnets, and possibly in orthoferrites. The expressions for ϵ_d and g in this case are

$$\epsilon_d(\omega) = 1 + \omega_p^2 \sum_{+}^{-} f_{\pm} \frac{\omega_{0\pm}^2 - \omega^2 + \Gamma^2 - i2\omega\Gamma}{(\omega_{0\pm}^2 - \omega^2 + \Gamma^2)^2 + 4\omega^2\Gamma^2} \tag{3.59}$$

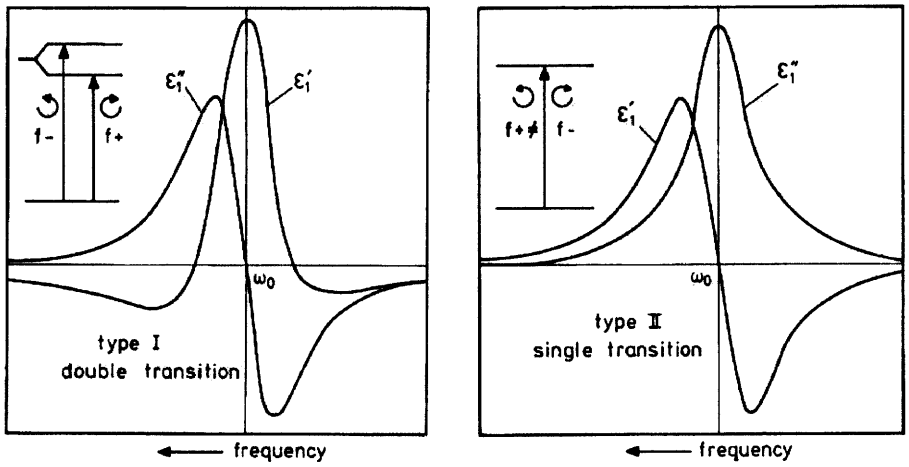

Figure 3-4: Energy band diagram and dispersion curves for a diamagnetic (left, "double") and paramagnetic (right, "single") transition. Note that ϵ_1 is equivalent to our g [31].

$$g(\omega) = \omega_p^2 \bar{\sum_{+}} (\pm) \frac{f_\pm}{2\omega_{0\pm}} \frac{\omega(\omega_{0\pm}^2 - \omega^2 - \Gamma^2) + i\Gamma(\omega_{0\pm}^2 + \omega^2 + \Gamma^2)}{(\omega_{0\pm}^2 - \omega^2 - \Gamma^2)^2 + 4\omega^2\Gamma^2} \tag{3.60}$$

where $\omega_p^2 \equiv 4\pi Ne^2/m$ is the square of the plasma frequency, $\omega_{0\pm} = \omega_0 \pm \Delta$, and $f_\pm \approx (f/2)(1 \pm \Delta/\omega_0)$. The sum extends over the $\pm$ modes. Also, the transition occurs at frequency ω_0, but is diamagnetically split by frequency 2Δ and has a characteristic linewidth of Γ. We should also note that, in this simple example, we are only considering the contribution to ϵ_d and g of one transition. In reality, there are many that need to be summed over as well. In theory, if one knew the types, positions, linewidths, and oscillator strengths of all the transitions in a material, one could write down $\epsilon_d(\omega)$ and $g(\omega)$ and, using Eq. (3.48), could write down $F_\Theta(\omega)$. By maximizing $F_\Theta(\omega)$, one could, in principle, find the optimal frequency at which to operate an isolator.

3.5.3 The Importance of Δ

Because of the dependence of $f_\pm$, and therefore g, on Δ in Eq. (3.60), it becomes clear that the excited state splitting of a diamagnetic transition is the most important parameter one needs to tune to obtain high Faraday rotation. It can even be shown

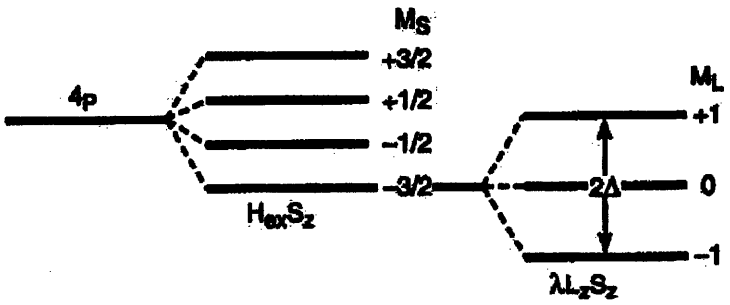

Figure 3-5: Exchange field spin quenching of a ^{4}P orbital split by the Zeeman effect, followed by a spin-orbit splitting of the quenched level, resulting in 2Δ [32].

that in the vicinity of a transition (i.e. $\omega \approx \omega_0$) and for $\Gamma \ll \omega_0$ [80]

$$g(\omega) \approx -\omega_p^2 \frac{f}{2} \frac{\Delta}{\omega_0} \frac{(\omega_0 - \omega)^2 - (\Gamma^2 + \Delta^2) + i2(\omega_0 - \omega)\Gamma}{[(\omega_0 - \omega)^2 - (\Gamma^2 + \Delta^2)]^2 + 4(\omega_0 - \omega)^2\Gamma^2} \tag{3.61}$$

so that g is clearly proportional to Δ. Remembering from Eq. (3.48) that $F_\Theta = g'/2(\epsilon_d'' + g'')$ and seeing from Eq. (3.61) that g' and g'' are both, to first order, linear in Δ, we see that we can maximize F_Θ by raising Δ as much as possible.[11] Because Δ, then, is so essential to achieving high Faraday rotation, it is worth knowing a bit about its origins.

In garnets, in particular (and possibly in orthoferrites as well), the value of Δ is determined by the magnitude of spin-orbit coupling of the Fe^{3+} valence electrons. This effect is enhanced greatly if the spins of these electrons are aligned in the same direction. This alignment can occur through an applied field which induces an exchange field in the material. As shown in Figure 3-5 for a ^{4}P term, the exchange field serves to align the spins and quench the spin degeneracy, while the level to which these spins are quenched is itself then split by spin-orbit coupling. 2Δ is then defined by the separation between $m_L = \pm 1$ [32].

The most important reason we care about Δ so much is that its value in iron garnets seems to be greatly affected by Bi-substitution. For the transition in the

[11] Of course, since F_Θ has a $\Delta/(1+\Delta)$-type dependence to first order, it will eventually saturate at high Δ; eventually, therefore, we will reach a region of diminishing marginal returns as we increase it, but let us not worry about that for now.

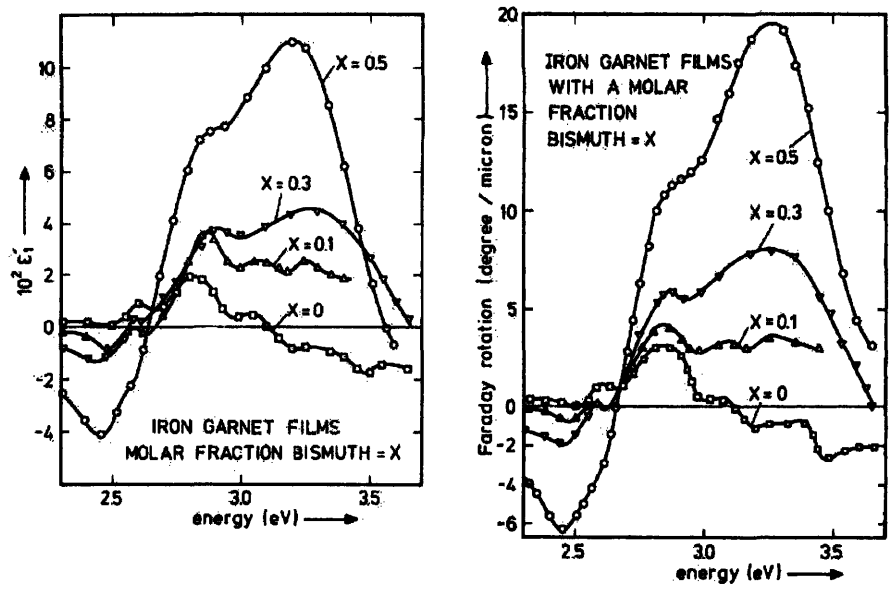

Figure 3-6: Off-diagonal components of the dielectric tensor (left) and Faraday rotation (right) as a function of bismuth content x and energy in $Y_{3-x}Bi_xFe_5O_{12}$ [31].

Bi-O-Fe system located near ω_0 =3.15 eV, one group found that a 4-fold increase in Bi-content x in $Y_{3-x}Bi_xFe_5O_{12}$ caused a 3.7-fold increase in Δ, demonstrating an almost linear dependence of Δ on x [31]. As can be seen from Figure 3-6, the increase in Δ results in an increase in g' (called ϵ_1' in the figure) around the transition. This increase, in turn, results in an increase in Faraday rotation.

It is thought that the Bi^{3+} ion increases Δ by mixing its valence $6s$ and $6p$ orbitals with the $2p$ valence orbitals of the surrounding oxygens as well as with, to a lesser degree, the iron $3d$ orbitals. This mixing causes an increase in Δ since the $6p$ valence electrons have a high spin-orbit coupling. Coincidentally, another desirable effect of the mixing is that the oscillator strength f goes up since there are more electrons available to make a transition [31].

By fitting the models proposed thus far to actual spectra of dielectric tensor elements, it is possible to quantify values of ω_0, Γ, and Δ in these garnet materials. The two transitions that correspond to the Fe^{3+} in an octahedral [a] site and a tetrahedral (d) site in Bi:YIG are described in Table 3.1. We should note that these transitions, as indicated, give Faraday rotations of opposite sign and, therefore, somewhat cancel

Table 3.1: ELECTRIC DIPOLE TRANSITIONS IN BI:YIG FROM [45]

Site	ω_0 (eV)	Γ (eV)	Δ (eV)	Sign of θ
Fe_a^{3+}	3.15	0.47	0.27	+
Fe_d^{3+}	2.51	0.38	0.11	−

each other out. Consequently, we expect that $BiFeO_3$, which *only* possesses Fe_a^{3+}, to have a much higher a Faraday rotation than Bi:YIG given the same superexchange field.

The challenge of turning $BiFeO_3$ into a good isolator material, then, really turns into the challenge of aligning all the Fe_a^{3+} ions. Eventually, we would like to do so by compositionally tuning the B-site in the perovskite lattice. By mixing transition metals like Co, Mn, and Ni in a 1:1 ratio with Fe, we hope to induce a strong superexchange field that will align these Fe_a^{3+} moments, quench the excited state degeneracy, and result in a well defined splitting due to spin-orbit coupling. The Bi on the A-site will hopefully, as it does in the garnet materials, enhance the splitting due to this coupling, creating an effective isolating material. Furthermore, at some point, we will also need to consider the birefringence of these materials and how it influences both theoretical and practical aspects of our investigation.

Chapter 4

Experimental Methods

This chapter is designed to give a brief overview and explanation of the various experimental methods of thin film growth and characterization used in our research. Many of these methods are quite standard in the field, so, when appropriate, we have provided excellent references in which the reader may find a more extensive explanation of the underlying physics of the processes utilized in these techniques.

4.1 Film Growth with PLD

Pulsed Laser Deposition (PLD) or Pulsed Laser Ablation (PLA) is a very simple method of deposition in principle. As shown in Figure 4-1, a target (of pressed oxides, in our case) sitting on a rotatable holder in a vacuum chamber is subjected to repeated, optically focused pulses from a high power laser source, creating a plasma plume of material which then is deposited on a nearby substrate. The substrate assembly sits on top of a heating element in order to aid kinetics during growth. The vacuum base pressure, achieved using a turbo pump, is usually better than 10^{-6} Torr. Once a good vacuum is achieved, different gases can be flowed into the chamber to enhance the growth of certain phases. The laser is scanned, or "rastered," across the surface of the target in order to ablate the material more uniformly and to prevent the laser from digging too deep a hole into the target. Many different high power lasers over a variety of wavelengths can be used, but the most popular are the excimers,

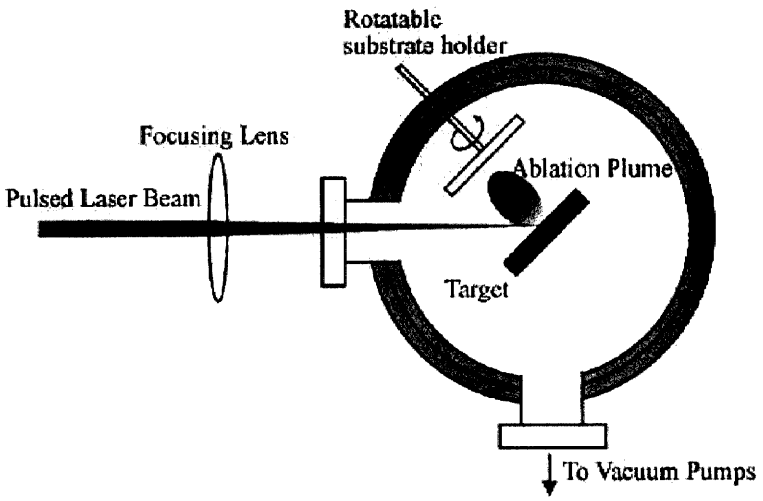

Figure 4-1: Schematic diagram of a PLD apparatus with rotatable substrate holder [33].

which operate in the UV at 308 nm (XeCl), 248 nm (KrF), 193 nm (ArF), and 157 nm (F_2) [33].

The complexities of PLD lie in the physics of the actual ablation process. Although the specifics are out of the scope of this discussion (but can be found in an excellent theoretical discussion in [81]), a heuristic understanding can be gleaned from Figure 4-2. Essentially, a laser pulse causes extremely rapid heating and expansion of the

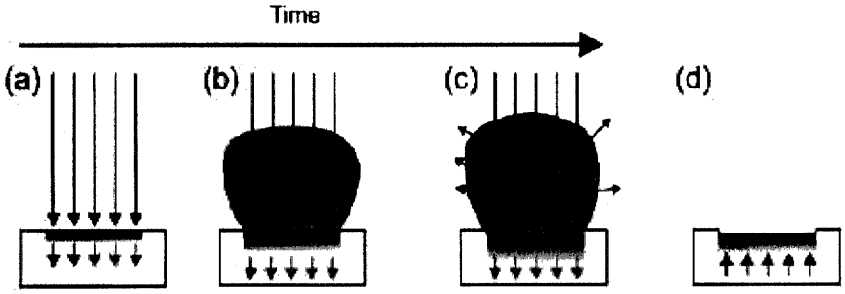

Figure 4-2: Schematic indicating the key steps in the ablation process: (a) Initial absorption of laser energy by the target (long arrows); melting and vaporization begin (shaded area is melted material, short arrows indicate formation of solid-liquid interface). (b) Melt front moves farther into the solid target, vaporization continues, and the laser begins to interact with the plume. (c) Plume begins to absorb laser radiation and the plasma begins to form. (d) Melt front recedes and re-solidification begins [33].

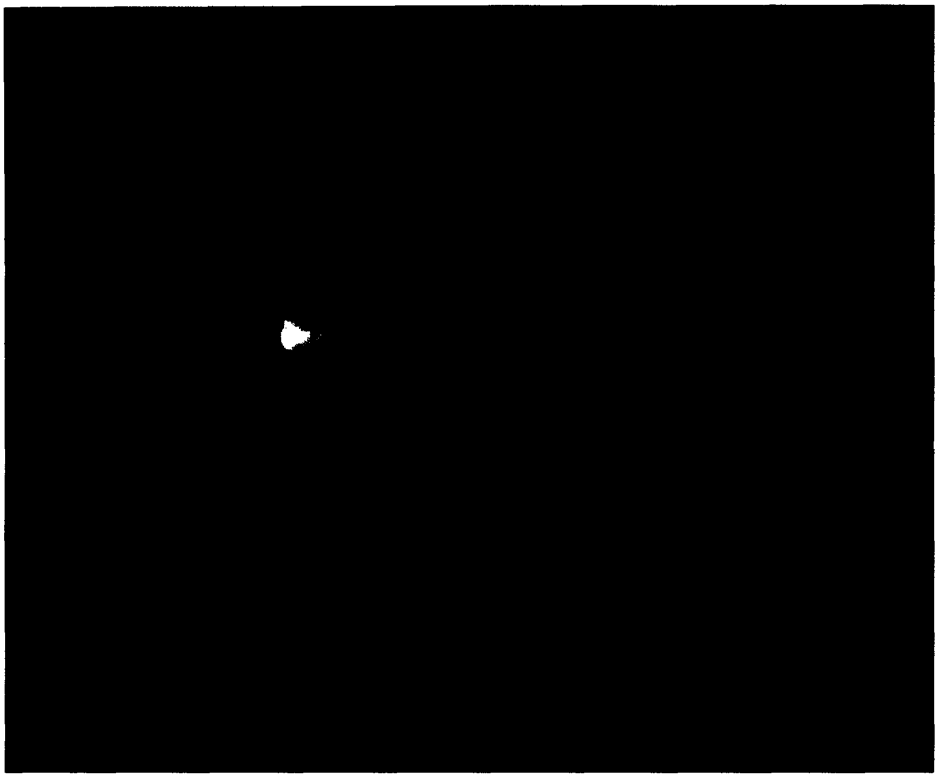

Figure 4-3: Image of a PLD plume created by a typical $SrRuO_3$ deposition. The target is on the left, as is the inception point of the plume, and the substrate is on the right [34].

target material. The heat and stress cause phase transitions in the material, and some of it will boil off and go into the gas phase. This ejection occurs on a picosecond timescale. Once a plume of gas begins to develop, it will then *itself* begin to interact with the laser pulse and absorb energy. As it does so, the plume will begin to be ionized, forming a plasma and causing optical emission, as shown in Figure 4-3. After the pulse dies off, the target resolidifies. The plume, however, now carrying a variety of charged and uncharged particles, continues to expand away from the target until it ultimately impinges on the substrate where the deposited material condenses to form a film.

This method of deposition affords several key advantages over other conventional film deposition methods such as vacuum evaporation and sputtering (this list is paraphrased from [82]):

1. The maximum instantaneous deposition rate is much higher in PLD than in

other conventional thin film deposition methods, although it is often necessary to operate at lower rates in order to achieve better crystalline quality and lower roughness in films.

2. The higher concentration of ionic particles (around 10%) in PLD as well as the higher particle velocities (on the order of 10^6 cm/s) aid crystal growth and reduce the substrate temperature needed to grow a crystalline film.

3. PLD can be used to grow many different materials in a similar fashion, even during the same deposition as in multilayers; whereas, in evaporation methods and sputtering, a different electron "gun" must be used for each material.

4. Instead of the atomistic ejections that occur in other methods, a variety of species, including diatomic molecules, are ejected from the target in PLD. This process can contribute to more accurate stoichiometry transfer between the target and the film, although this accuracy does not hold for all materials.

5. The PLD plume has a characteristic $\cos^n \theta$ distribution, where θ is the angle away from the target normal direction and n is a power greater than one. For other deposition methods, n is often of order one, so PLD turns out to be more directional and therefore makes more efficient use of the target material. However, for the same reason, PLD can often result in nonuniformities in film thickness, thereby limiting the areal size of the substrate.

Perhaps the most significant disadvantage, however, is that it is very difficult to prevent particulates (or "droplets") from forming on the surface of the film as a consequence of the fact that the laser can ablate large chunks of material from the target. The prevalence of these droplets on the film surface is proportional to the target-substrate distance, so moving the substrate away from the target can help. However, doing so also reduces the deposition rate significantly, so there is a tradeoff between quality and speed present here that is, of course, present in all deposition methods [82].

Table 4.1: PLD Conditions for Bismuth Orthoferrite Deposition

Growth Parameter	Value
T_s	530-710°C
p_{O_2}	0.001-15 mTorr
λ	KrF, 248 nm
E	550 mJ
f	10 Hz
ρ	5 J/cm^2
t_p	25 ns
P	5.5 W
d	7 cm
r_d	1-15 nm/1,000 pulses or 0.6-9.0 nm/min
r_c	5°C/min
t_a	varies
T_a	varies
p_a	$\approx$ 50 mTorr
p_b	$\approx$ 0.001 mTorr
Target Bi:Fe	1.2:1
Substrate	MgO (001), $SrTiO_3$ (001), Si (001)

There are many controllable parameters in the PLD process, the most important of which are the substrate temperature T_s and the ambient gas pressure during deposition. Since we only made films in an oxygen ambient, we will refer to this pressure as p_{O_2}. Other parameters (some of which are interrelated) include laser wavelength λ, energy per laser pulse E, pulse repetition rate f, energy fluence ρ (in J/mm^2), laser pulse length t_p, laser power P, target-substrate distance d, deposition rate r_d (in nm/1,000 pulses or nm/min), cooling rate r_c (in °C/min), anneal time t_a, anneal temperature T_a, anneal oxygen overpressure p_a, and overall base pressure p_b. Choosing the correct target stoichiometry is also essential, as is the choice of the correct substrate. Values of these parameters for our apparatus are shown in Table 4.1.[1]

[1]For an additional review, as well as information on the development of PLD, see [83]. For a more in depth description, see [84]. Finally, an amusing animation of the PLD process can be found at `http://www.geocities.com/afserghei/LVE.htm`.

4.2 Structural Characterization with 2DXRD

X-ray diffraction (XRD) is the bread and butter of most materials scientists interested in phase identification, texture analysis, and structure refinement, as well as other types of analyses. The tool of choice has traditionally been one-dimensional XRD (1DXRD), and this technique is amongst the most well understood in our field.[2]

Two-dimensional XRD (2DXRD), however, is used far less frequently by the materials science community due to the fact that it is a relatively new concept. Only recently have advances in detector technology, point beam-xray optics, and computing power allowed 2DXRD to achieve its full utility [36]. We have, in fact, found the technique so invaluable for phase identification, texture analysis, and lattice parameter determination in thin films that we have used it almost exclusively in preparing this thesis.

The five main components of a 2DXRD system are shown in Figure 4-4 for the Bruker AXS D8 DISCOVER with GADDS, which is the instrument we have used in our analysis. These components are the two-dimensional detector itself, the sample stage (sitting on an Eulerian cradle), the video camera and laser optics which are used for alignment, the x-ray collimator (for us, either a monocapillary or pinhole collimator with a 0.5 mm diameter opening), and the x-ray generator. The standard coordinate systems defined in the picture are $2\Theta_g$, the angle between the direction of the incident beam and the center of the detector; ω, the angle between the plane of the sample and the incident beam; ϕ, the angle of rotation in the plane of the sample; and χ, the angle of out-of-plane tilt of the sample, viewed as a slide up or down the Eulerian cradle. The plane of the sample is defined as the xy-plane, and the normal direction is the z-direction. All three of these orthogonal directions can be scanned in addition to the angular orientations [86].

As x-rays are directed down the collimator from the source, they interact with the sample causing a spherical diffraction in three dimensions. Since the waveforms

[2]Because we feel that so many of the concepts in 1DXRD are elementary, we refer the reader to [85] for explanations of the basic concepts of XRD. From henceforth, an introductory knowledge shall be assumed.

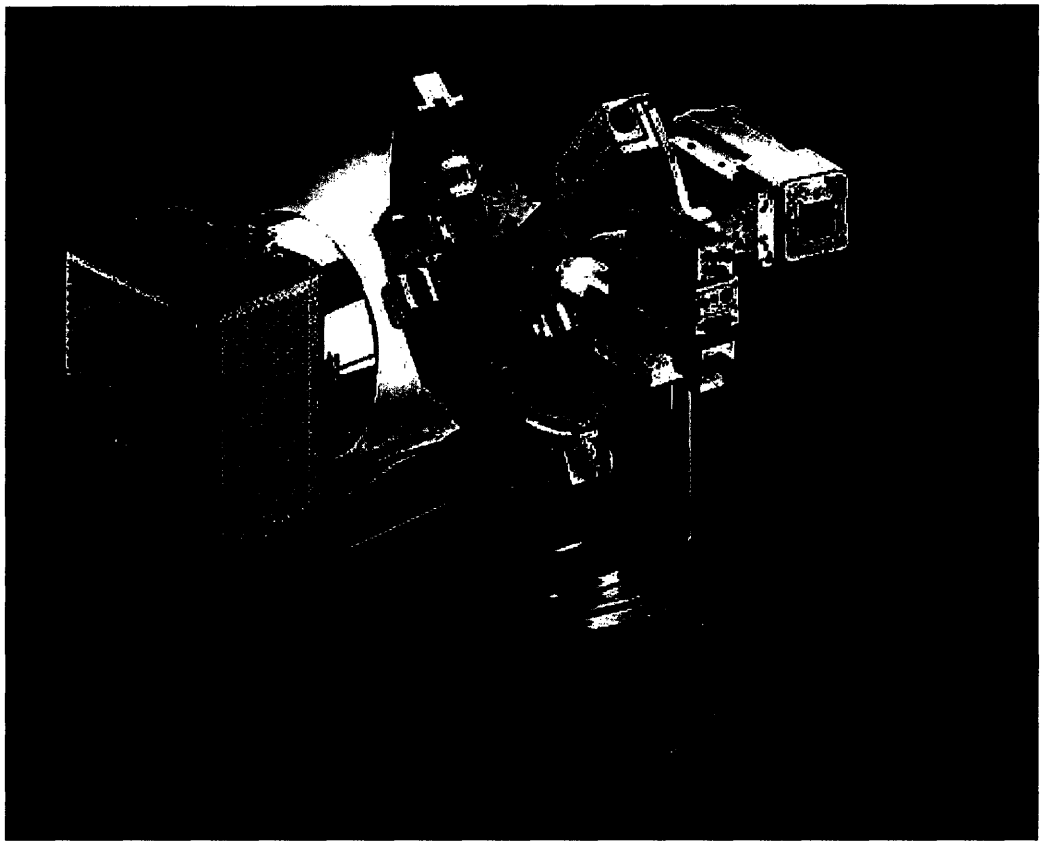

Figure 4-4: Image of the Bruker AXS D8 DISCOVER with GADDS with main components and variables indicated [35].

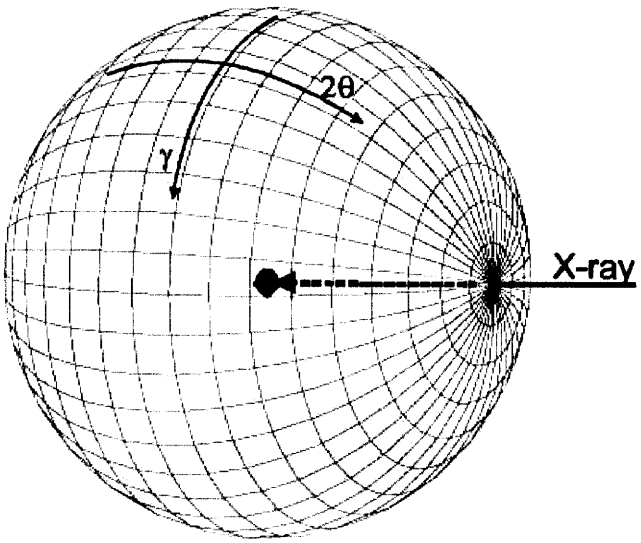

Figure 4-5: Schematic of the ideal two-dimensional detector: a sphere covering a solid-angle of 4π. The coordinates 2Θ and γ are indicated [36].

of the electromagnetic radiation radiate with spherical symmetry from the sample, a perfect detector would have the shape of a sphere whose center is the sample. This detector would capture all the signal from the sample and cover a solid angle of 4π, as shown in Figure 4-5. The coordinates along the two-dimensional, curved surface of the sphere are described angularly by 2Θ (different from $2\Theta_g$) and γ. In reality, however, a detector is only a section of this spherical surface; and, moreover, it is not even spherical, but flat. Nevertheless, it is possible to extract information from a 2D diffraction pattern, even with a flat detector, through an "unwarping" procedure. The diffraction pattern ends up looking like rings, the source of which are described in Figure 4-6. We can see that 2Θ describes the distance of the ring away from the sample, while γ describes where we lie along the ring itself. These alternate descriptions, of course, map directly to the definitions in Figure 4-5.[3]

Scanning through 2Θ and γ in Figure 4-5 is tantamount to building an Ewald sphere, a spherical representation of the sample in reciprocal space. In our films, we can see three different types of diffraction patterns, each of which represents a slice

[3]It is interesting to note that a 1DXRD scan would account for only the $\gamma = 90°$ plane, i.e. the diffractometer plane, in Figure 4-6. By capturing a range of values in γ, we therefore obtain a great deal more information with the 2DXRD scan.

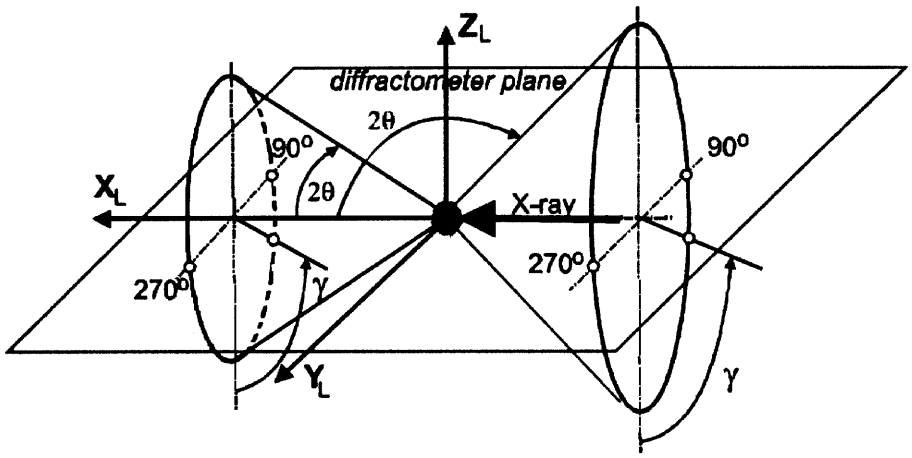

Figure 4-6: Relationship between diffraction rings and x-ray coordinates 2Θ and γ [36].

through the Ewald sphere. As shown in Figure 4-7, small dots represent diffraction from single crystal planes, which have a definite value of 2Θ and γ. At the other extreme, a purely polycrystalline film will exhibit all values of γ (crystals of all tilts) for a given value of 2Θ diffraction. In between these two extremes is the textured film, for which certain values of γ diffract, but others do not. This detailed information regarding texture is quite difficult to obtain with 1DXRD, but, as we can see, it is quite elementary to do with 2DXRD.

It now becomes clear that moving the detector to a value of $2\Theta_g$ in real space is equivalent to taking a slice of the Ewald sphere at "distance" $2\Theta_g$ from its center. In 2DXRD, however, because our detector approximates a section of the curved surface of the ideal detector shown in Figure 4-5, many values of 2Θ (say $2\Theta \in [2\Theta_g - \Delta, 2\Theta_g + \Delta]$) are measured simultaneously. Each measurement of 2Θ therefore consists

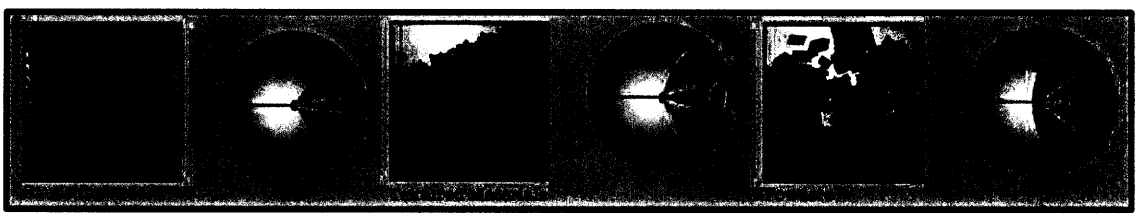

Figure 4-7: Crystallographic diagrams and Ewald spheres for different types of samples examined using 2DXRD [37].

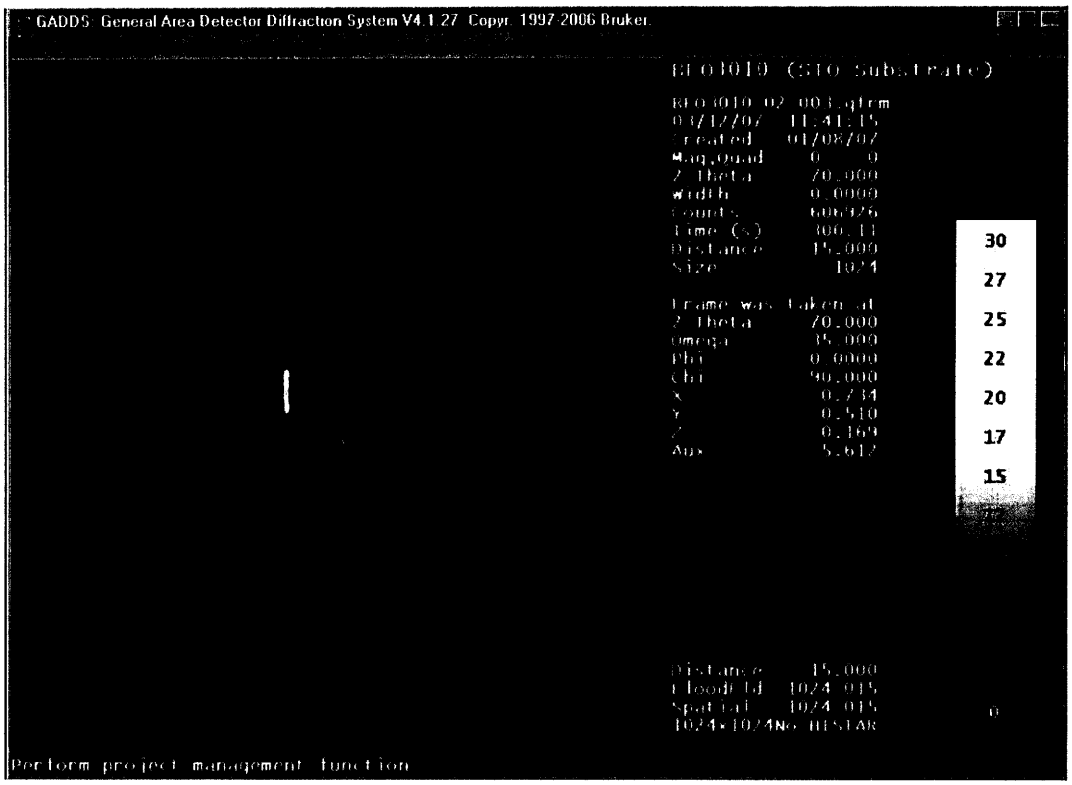

Figure 4-8: Characteristic data output of Bruker 2DXRD software for a highly textured BFO film grown on STO (001). The 2Θ and γ coordinate directions are shown, as well as sections of diffraction rings (light blue) indicating the constant values of 2Θ for which the STO (003) and BFO (003) peaks appear. This frame was obtained while rotating in ϕ, at $2\Theta_g = 70°$, $\omega = 35°$, and $\chi = 90°$.

of a "frame" or "window" of width Δ on each side of $2\Theta_g$. In practice, Δ can be anywhere between 8° and 15°, although we will use the latter setup almost exclusively (corresponding to a physical distance between the detector and the sample of 15 cm). Furthermore, just as $2\Theta_g$ represents the physical position of the detector but our diffraction pattern contains a range of values in 2Θ, χ represents the tilt of our sample on the Eulerian cradle, but our diffraction pattern contains a range of values in γ, centered at $\gamma = \chi$.

The data output of the detector software, then, typically looks like that shown in Figure 4-8 for a highly textured BFO film grown on an STO (001) substrate. Arcs of constant 2Θ are shown in light blue, and 2Θ increases as these arcs move to the left. Lines of constant γ are essentially radial lines emanating from the right side

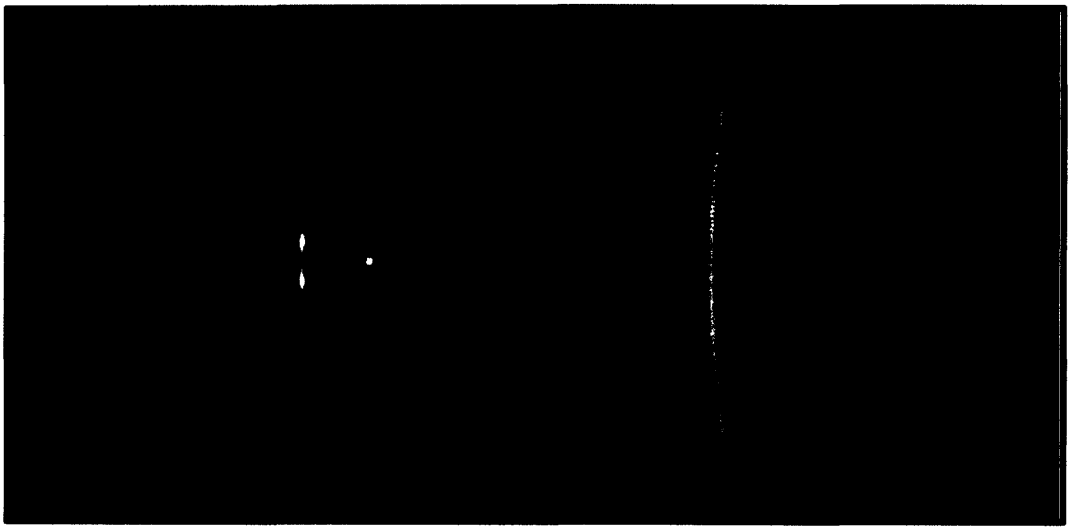

Figure 4-9: Characteristic data output of Bruker 2DXRD software for a textured film (left) and a perfectly polycrystalline film (right).

of the detector. We can arrive at a typical XRD pattern, i.e. diffraction intensity as function of 2Θ, by integrating over γ over some domain in 2Θ. Similarly, we can do the opposite to obtain an XRD pattern in γ. In this case, the usual 2Θ pattern (i.e. the former integration) would have two peaks: one corresponding to the BFO (003) and one corresponding to the STO (003). We know that the higher angle peak is the single crystal substrate STO (003) because it is very narrow in 2Θ as well as in γ and is very bright, even at high angle.[4] The highly textured peak is slightly broader both in 2Θ and γ, but still fairly close to the $\gamma = 90°$ axis. It should also be noted that this pattern was obtained while rotating the sample uniformly in ϕ, thus averaging out any texture components in-plane. The fact that we see two dots for BFO (003) is then simply a consequence of the fact that the sample is slightly tilted and, upon rotating in ϕ, there is a slight eccentricity. In the case where we only care quantitatively about 2Θ, however, the difference really does not matter. If we wished to know more about γ quantitatively, a more careful analysis would be needed.

The detector data output for both a more lightly textured film and a perfectly polycrystalline film (corresponding, respectively, to the middle and rightmost parts of Figure 4-7) are shown in Figure 4-9. Whereas the latter has rings of uniform intensity,

[4]Note that this situation corresponds to the leftmost part of Figure 4-7.

corresponding to all values of γ for a given value of 2Θ, the former has rings of non-uniform intensity. Those values of γ for which there is more intensity are referred to as the directions of the texture. In the aforementioned case of a highly textured film, only a very small section of certain rings have a large intensity.

Although 2Θ scans obtained by integrating over the detector area in γ will be the most useful types of scans to determine phase content and lattice parameters of films, we will at times find it useful to perform scans in ϕ as well as in ω, otherwise known as "rocking curves" with respect to those variables. A rocking curve in the former can reveal information about the crystal symmetry of a highly textured film, while a rocking curve in the latter can reveal the quantitative degree of epitaxy or texture of a high-quality film. Integrating in 2Θ to obtain a rocking curve in γ can also be useful. More detailed information on the theory and practice of 2DXRD can be found in [87].

4.3 Magnetic Characterization with VSM

To measure magnetic hysteresis loops of our films, we used a Vibrating Sample Magnetometer (VSM) Model 1660 made by ADE Technologies, an approximate schematic of which can be found in Figure 4-10. The first magnetometer was designed by Simon Foner in 1959 [88]. Since then many improvements have been made to the device, mostly electronic in nature, which have allowed it to reach its current configuration.

Essentially, the sample is attached to a long rod and vibrated at a constant frequency and amplitude in the vicinity of two pickup coils. The sample also sits in a large magnetic field provided by two large electromagnets, capable of 10 kOe in our case. The magnetic field serves to magnetize the sample; this magnetization is then translated into an AC voltage in the pickup coils via the movement of the specimen. The important fact to realize is that the DC field from the electromagnets is not picked up by the coils since the induced voltage only arises from time dependant fields [89, pg. 67].

In the past, a reference sample was attached to the vibrating rod with its own set

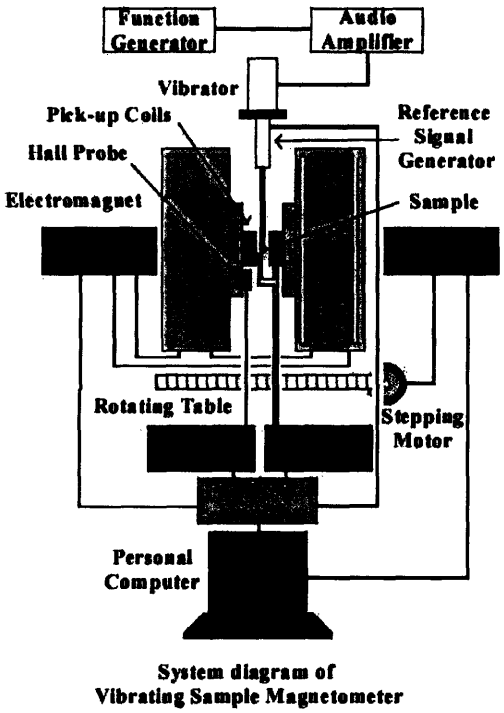

Figure 4-10: Schematic of a vibrating sample magnetometer (VSM) [38].

of pickup coils and the actual magnetization of the sample material was calculated through a ratio method that was designed to ignore the influence of the frequency and amplitude of the vibration and any instabilities in the electronics. The advent of modern electric circuits, however, releases us from this calibration scheme so that now we calibrate the VSM with a Ni standard, mounted in the sample position, at the beginning of every measurement. Thus, the measurement consists of applying a DC H field with the electromagnets and measuring the induced voltage as a function of time in the pickup coils, which can be processed to obtain M. The result is a hysteresis loop for M as a function of H.[5]

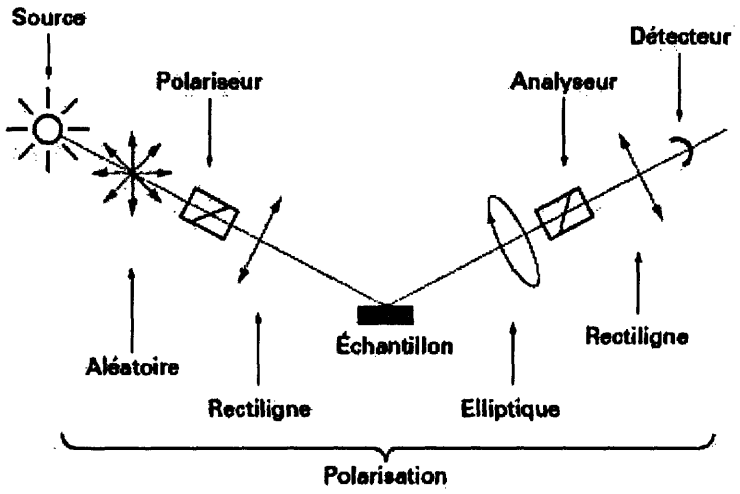

Figure 4-11: Schematic of a typical ellipsometry setup, including (from left to right) the source with random ("Aléatoire") output, polarizer with linear ("rectiligne") output, sample with elliptical ("elliptique") output, analyzer with linear output, and detector [39].

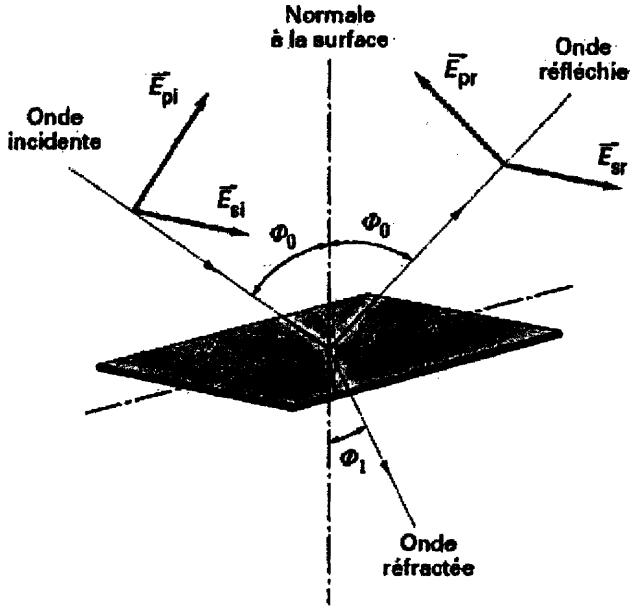

Figure 4-12: Illustration of a reflected electromagnetic wave split up into its s- and p-components reflecting off of a surface as in ellipsometry [39]. The French is hopefully simple enough to require no translation!

4.4 Optical Characterization with Ellipsometry

To measure the average real and imaginary parts of the index of refraction of our materials, n and k respectively, as well as to obtain a more accurate measure of thickness t, we used a SOPRA Spectroscopic Ellipsometer equipped with detectors spanning a large spectral range (from 200 nm to 2000 nm). The principle behind ellipsometry is that one can obtain information about the dielectric constants of a material by looking at the change in polarization of reflected light. A schematic of a typical ellipsometric setup is shown in Figure 4-11. SOPRA uses in its machine a rotating polarizer configuration, in which the polarizer is rotated while the measurement is being taken. This setup has the advantage that the detector does not need to be sensitive to polarization and that the spectrometer can be placed between the analyzer and the detector. This configuration also tends to suppress parasitic light [39].

In order to understand the principles of operation of the ellipsometer, it is useful to split the electric vector $\boldsymbol{E}$ into two components: an s-component parallel to the surface of the film and a p-component perpendicular to it. Figure 4-12 shows these two components, both for an incident wave (subscript i) and a reflected wave (subscript r). The angle of incidence equals the angle of reflection (both Φ_0), and Snell's law gives the angle of the refracted wave Φ_1 by $\sin\Phi_0 = n\sin\Phi_1$. In terms of the amplitudes of these vector components of the electric field, we then write the s and p reflectivities, respectively, as

$$\begin{aligned} r_s &= \frac{E_{sr}}{E_{si}} = |r_s|e^{i\delta_s} \\ r_p &= \frac{E_{pr}}{E_{pi}} = |r_p|e^{i\delta_p} \end{aligned}$$

[5]It should also be noted that both in-plane and out-of-plane measurements can be taken with this technique, although, with the former type, it is easier to saturate the material and therefore obtain a reliable M_s.

which we then divide by one and other to obtain

$$\rho \equiv \frac{r_p}{r_s} = \tan\Psi e^{i\Delta} \tag{4.1}$$

where $\tan\Psi \equiv |r_p|/|r_s|$ (where Ψ is defined differently here than in the previous chapter) and $\Delta = \delta_p - \delta_s$. The two ellipsometric parameters Ψ and Δ defined in Eq. (4.1) are related to the azimuthal angle θ of the elliptically polarized light (i.e. the angle between the major axis of the ellipse and the film normal) and the ellipticity $e = a/b = \tan\varepsilon$ (where a and b are the lengths of the semi-minor and semi-major axes of the ellipse, respectively), by

$$\sin 2\varepsilon = \sin 2\Psi \sin\Delta$$

$$\tan 2\theta = \tan 2\Psi \cos\Delta$$

Furthermore, the intensity seen by the detector I can be written as

$$I = I_0(\alpha \cos 2P + \beta \sin 2P + 1) \tag{4.2}$$

where P is the angle of the polarizer and

$$\alpha = \frac{\tan^2\Psi - \tan^2 A}{\tan^2\Psi + \tan^2 A} \tag{4.3}$$

$$\beta = 2\cos\Delta \times \frac{\tan\Psi \tan A}{\tan^2\Psi + \tan^2 A} \tag{4.4}$$

$$I_0 = \frac{|r_s|^2|E_0|^2}{2}\cos^2 A(\tan^2\Psi + \tan^2 A) \tag{4.5}$$

where A is the angle of the analyzer and E_0 is the initial amplitude of the electric field. Using Eqs. (4.2-4.5), we can write the ellipsometric parameters Ψ and Δ as

functions of these measurable quantities α, β, and A in the following way:

$$\tan\Psi = \sqrt{\frac{1+\alpha}{1-\alpha}}\tan A \tag{4.6}$$

$$\cos\Delta = \frac{\beta}{\sqrt{1-\alpha^2}} \tag{4.7}$$

Note that, according to Eq. (4.2), α and β are independently measurable quantities for special values of P, i.e. when $P = 0°$, $I = I(\alpha)$, but when $P = 45°$, $I = I(\beta)$. Furthermore, Eqs. (4.6-4.7) show no dependence on I_0, which allows us to ignore the initial light intensity. Knowing Ψ and Δ, then, by Eq. (4.1) we know ρ. For the simple case of a two-layer measurement (i.e. air/substrate), ρ and Φ_0 are all we need to determine the complex index of refraction $n + ik$, which is given by

$$n + ik = \sin\Phi_0\sqrt{1+\left(\frac{1-\rho}{1+\rho}\right)^2\tan^2\Phi_0} \tag{4.8}$$

For a more complicated multilayer structure, such as a film on a substrate, this relationship is not so simple and will, in general, depend on the thicknesses t_i and complex indices n_i and k_i of each ith layer. A detailed analysis of these equations can be found in the various technical documents on SOPRA's website [39].

Once the measurement of Ψ and Δ is complete, we have many data points which sample the multi-layer version of Eq. (4.8). Thus, the right hand side is completely known, but the left hand side is not. In particular, if we choose to measure our sample at many different wavelengths λ_0, the λ_0 dependence of the left hand side, i.e. that of n and k, must be taken into account. For that reason, the SOPRA software performs a non-linear regression on the Cauchy Law

$$n = A + \frac{B}{\lambda_0^2} + \frac{C}{\lambda_0^4}$$

$$k = \frac{D}{\lambda_0} + \frac{E}{\lambda_0^3} + \frac{F}{\lambda_0^5}$$

in order to find the coefficients A, B, C, D, E, and F, which will determine n and k. The program also allows the user to fit on the thickness of each layer t. Advanced

features include the ability to fit on surface roughness and to manually add absorption peaks. In addition to the sources already provided, more information on the basic theories of ellipsometry may be found in [90].

4.5 Magneto-Optical Characterization

In order to measure the Faraday rotation of our samples, we use a custom-built Faraday rotation apparatus designed by Dr. David C. Bono, Research Scientist here at MIT. A full description of it, which we reproduce here, can be found in [27]:

> Faraday rotation was measured to an accuracy of 1 mdeg using a custom-built apparatus. Collimated laser light of 1.55 μm wavelength was focused through a rotating stage consisting of a polarizer prism and a Faraday cell modulator. The incoming light was modulated by an ac signal from a lock-in amplifier. The laser light then passed through a path bored in the pole pieces of an electromagnet, between which the sample was placed. A second prism detected the modulated ac signal. In all experiments, the Faraday rotation was measured with both the applied field and the laser beam perpendicular to the plane of the film.

The resulting data, which is a plot of the specific Faraday rotation Θ as a function of applied field H, was characterized in terms of its slope (i.e. the Verdet constant V) and its saturation M_s, remanence M_r, and coercivity H_c if it showed hysteresis.

4.6 Other Characterization Methods

In addition to its measurement with ellipsometry, film absorption was also measured in transmission mode with a Cary 500i UV-Vis-NIR Dual-Beam Spectrophotometer with a wavelength range of 175 nm to 1750 nm. This simple measurement technique essentially measures the percentage of transmitted light and converts that percentage into the absorption coefficient of the film and substrate. We also make an independent measurement of the substrate so that we can subtract it from the sample's signal in order to arrive at the absorption of the film only.

Preliminary thickness measurements, which were later refined by spectroscopic ellipsometry if needed (see Section 4.4), were performed with a Tencor P10 Surface Profilometer with a 2 μm radius diamond tipped stylus on Si samples which were made at the same time as their corresponding transparent substrate samples (either MgO or $SrTiO_3$). The Si sample consists of a piece of (001) oriented Si, half covered by a Si mask. The removal of this mask creates a very sharp step, which is easily measured by profilometry. We also have used profilometry in some cases to measure surface roughness.

Information on the stoichiometric composition of our films was obtained through Wavelength Dispersive Spectroscopy (WDS), performed by Dr. Nilanjan Chatterjee, Research Scientist here at MIT. Briefly, WDS consists of the bombardment of the sample with high energy electrons designed to remove inner core electrons of elements present in the sample. This removal results in decay of outer shell electrons to the empty inner shell, a process which releases photons in the x-ray spectrum. By comparing peak intensities to those of elemental standards and deconvoluting the peak information with a special software package, one can obtain fairly accurate elemental ratios in a material. This measurement occurs over several microns in diameter and penetrates deeply into the film, so it is therefore considered a bulk measurement. More information on WDS may be found in [91].

Chapter 5

$BiFeO_3$: PLD Growth & Characterization

In this chapter, we will present the bulk of our experimental data. Because we sought to characterize thin film $BiFeO_3$ (BFO) structurally, magnetically, optically, and magneto-optically, we realized that we first needed a high quality film. We therefore examined BFO grown on two transparent, cubic oxide substrates, MgO (001) and $SrTiO_3$ (001) (STO). We first optimized growth conditions of a polycrystalline phase on the former because it is cheaper, and then used the result of that optimization to grow high quality, epitaxial films on STO.

5.1 $BiFeO_3$ on MgO (001) Substrates

5.1.1 Optimization of Growth Conditions

MgO is a cubic crystal with the NaCl structure and a lattice parameter of $a = 4.216$ Å. BFO (using its bulk rhombohedral parameter of $a = 3.959$ Å from Section 2.2.1) has a 6.7% lattice mismatch with the MgO substrate. It is therefore highly unlikely that we could grow an epitaxial film of BFO on MgO. Nevertheless, because MgO is so much cheaper than $SrTiO_3$, which has a smaller lattice mismatch of 0.8%, we used the former to optimize our deposition conditions to obtain only polycrystalline BFO.

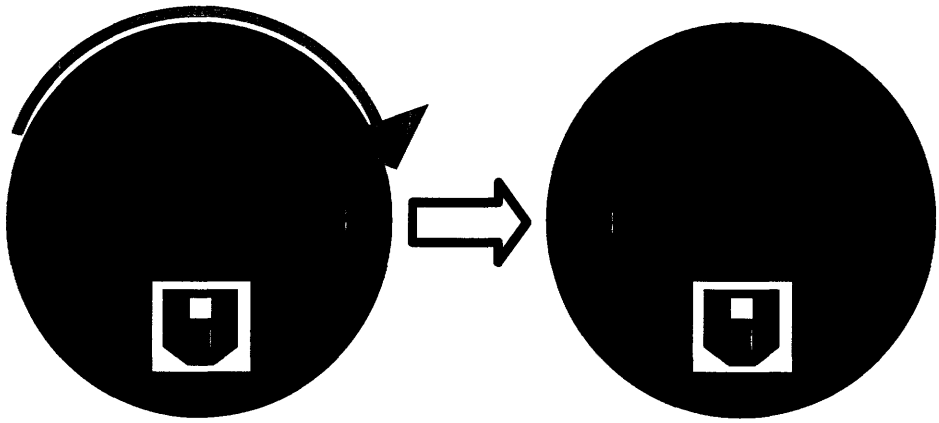

Figure 5-1: Schematic of our 2-sample deposition stage showing how during the deposition of the second sample, the first one is always *in situ* annealed (ISA).

Because of the way our PLD system is constructed, however, it is impossible to make two samples *in situ* with exactly the same conditions. Specifically, as shown in Figure 5-1, because we need to rotate the first deposited sample 90° in order to reveal the second one and hide the first one, the first sample will always have to sit on the heater while the second sample is being deposited. Therefore, the first sample will always be *in situ* annealed (ISA). This fact makes it very difficult to obtain an experimental matrix with reproducible conditions, so we have attempted in the following analysis to compare only "apples to apples," i.e. ISA samples with ISA samples and non-ISA samples (NISA) with non-ISA samples. It should also be noted that ISA does not include post-deposition annealing (PDA), which is the same for both samples. We shall also use the notation NPDA for non-PDA samples.

In our optimization, we kept constant all the deposition conditions in Table 4.1 with the exception of the substrate temperature T_s and the oxygen overpressure p_{O_2}. These were our variable parameters, and we constructed several experimental matrices to find the optimal phase and stoichiometry as a function of T_s (530°C–680°C) and p_{O_2} (vacuum to 15 mTorr).[1] We measured the phase content with two-dimensional x-ray diffraction (2DXRD) and the stoichiometry with wavelength dispersive spectroscopy (WDS). To confirm the presence of ferrimagnetic phases in some samples (like Fe_3O_4),

[1]By "vacuum," we typically mean pressures on the order of 1×10^{-6} Torr.

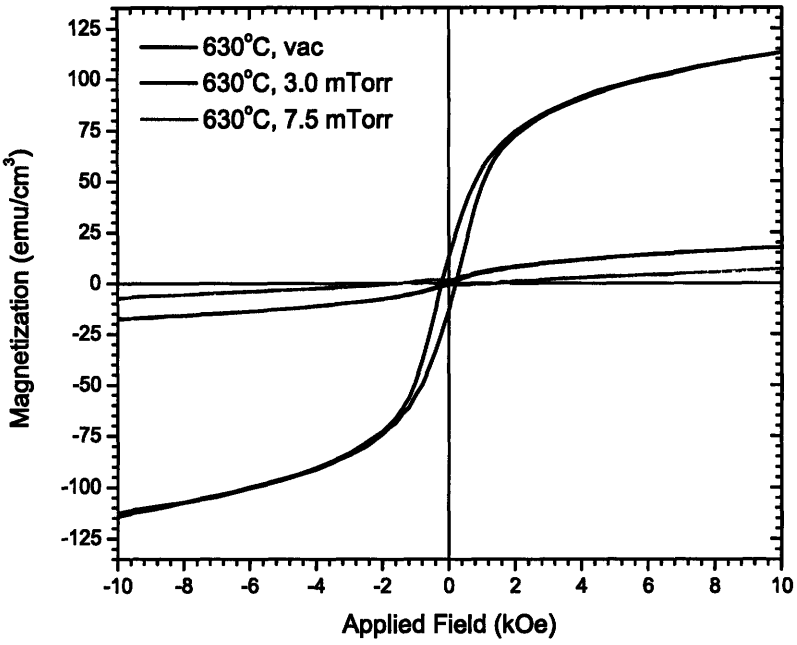

Figure 5-2: *M-H* hysteresis loops for 3 ISA-NPDA samples grown at $T_s = 630°C$ on MgO (001) at p_{O_2} =vac (black), 3.0 mTorr (red), and 7.5 mTorr (green). The MgO substrate has been subtracted from these loops already, but no other background subtraction has been performed.

we also examined these samples with vibrating sample magnetometry (VSM).

Because of the difficulty in controlling annealing, both ISA and PDA, across all samples, we shall attempt to compare samples that have similar annealing conditions. Therefore, we shall examine all possible permutations of annealing conditions, i.e. ISA-NPDA, NISA-NPDA, ISA-PDA, and NISA-PDA. For instance, in Table 5.1, we present an experimental matrix of phases found by 2DXRD for ISA-NPDA samples.[2] One main trend is clearly shown: that lowering the pressure to vacuum results in the formation of an iron oxide phase Fe_3O_4, magnetite. The VSM hysteresis loops in Figure 5-2 comparing those samples in the 630°C column of Table 5.1 (which have already had the MgO substrate and sample holder background subtracted through an independent measurement) clearly show the presence of this ferrimagnet, which

[2]The notation used in the tables in this section is the following: BFO=$BiFeO_3$, B2F4=$Bi_2Fe_4O_9$, Mag=Fe_3O_4, and Bis=Bi_2O_3. The dominant phase is always listed first; and, if no qualifier is given before a phase, it should be assumed that the two phases are of comparable volumetric magnitude.

Table 5.1: PHASES OF ISA-NPDA SAMPLES ON MGO (001)

T_s/p_{O_2}	530°C	580°C	630°C	680°C
vacuum		Mag	BFO, Mag	BFO, Bis, Mag
3.0 mTorr			BFO, slight B2F4	
7.5 mTorr			BFO, some B2F4	
15.0 mTorr				

Table 5.2: PHASES OF NISA-NPDA SAMPLES ON MGO (001)

T_s/p_{O_2}	530°C	580°C	630°C	680°C
vacuum	*All*			
3.0 mTorr		*Samples*		
7.5 mTorr			*Are*	
15.0 mTorr				*Glassy*

Table 5.3: PHASES OF ISA-PDA SAMPLES ON MGO(001)

T_s/p_{O_2}	530°C	580°C	630°C	680°C
vacuum				
3.0 mTorr	BFO, B2F4	BFO, some B2F4	B2F4	B2F4, some BFO
7.5 mTorr		BFO, B2F4, Mag		
15.0 mTorr				

Table 5.4: PHASES OF NISA-PDA SAMPLES ON MGO(001)

T_s/p_{O_2}	530°C	580°C	630°C	680°C
vacuum				
3.0 mTorr				
7.5 mTorr	BFO, Bis, Mag			
15.0 mTorr		BFO, Bis	BFO, Bis	

Figure 5-3: 2DXRD pattern for the ISA-NPDA sample deposited on MgO (001) at $T_s = 630°C$ and $p_{O_2} = 7.5$ mTorr, with frames centered at (a) $2\Theta_g = 33°$, (b) $2\Theta_g = 57°$, and (c) $2\Theta_g = 73°$. These patterns were taken while rotating in ϕ, with $\omega = 2\Theta_g/2$, and $\chi = 90°$. The rings, which have constant intensity at a given value of 2Θ as a function of γ, clearly show that all phases are polycrystalline, i.e. they possess no texture.

has an $M_s = 480$ emu/cm^3, in the sample grown in vacuum. No other phase except an iron oxide phase could account for a moment on the order of 100 emu/cm^3. This sample does not saturate, as one would expect for pure magnetite, however, due to the fact that it makes up only a fraction of the total volume of the film. On the contrary, those films grown in oxygen, which have BFO as their primary phase and the non-magnetic $Bi_2Fe_4O_9$ phase as a minor impurity, have a much lower moment at high field. Furthermore, they also do not show a clear saturating behavior because of the weak, canted antiferromagnetism of the BFO. WDS data from these samples reveals that, in the 630°C column, the vacuum sample has a Bi:Fe ratio of 0.20, while the 3.0 mTorr and 7.5 mTorr samples have ratios of 0.80 and 0.96, respectively. The stoichiometric data points to the source of the iron oxide phase at low pressures: a lack of enough of Bi to form BFO as the primary phase. We assert that the reason there is no Bi at low pressures is that the Bi atom is very volatile and easily escapes from the film when the ambient pressure is low. This trend is universally observed in the literature and by us, so we shall accept it as fact. Put in a more positive light, we find that we can use the oxygen overpressure during deposition to greatly influence the stoichiometry of our films and, as shown in the 7.5 mTorr sample which has a

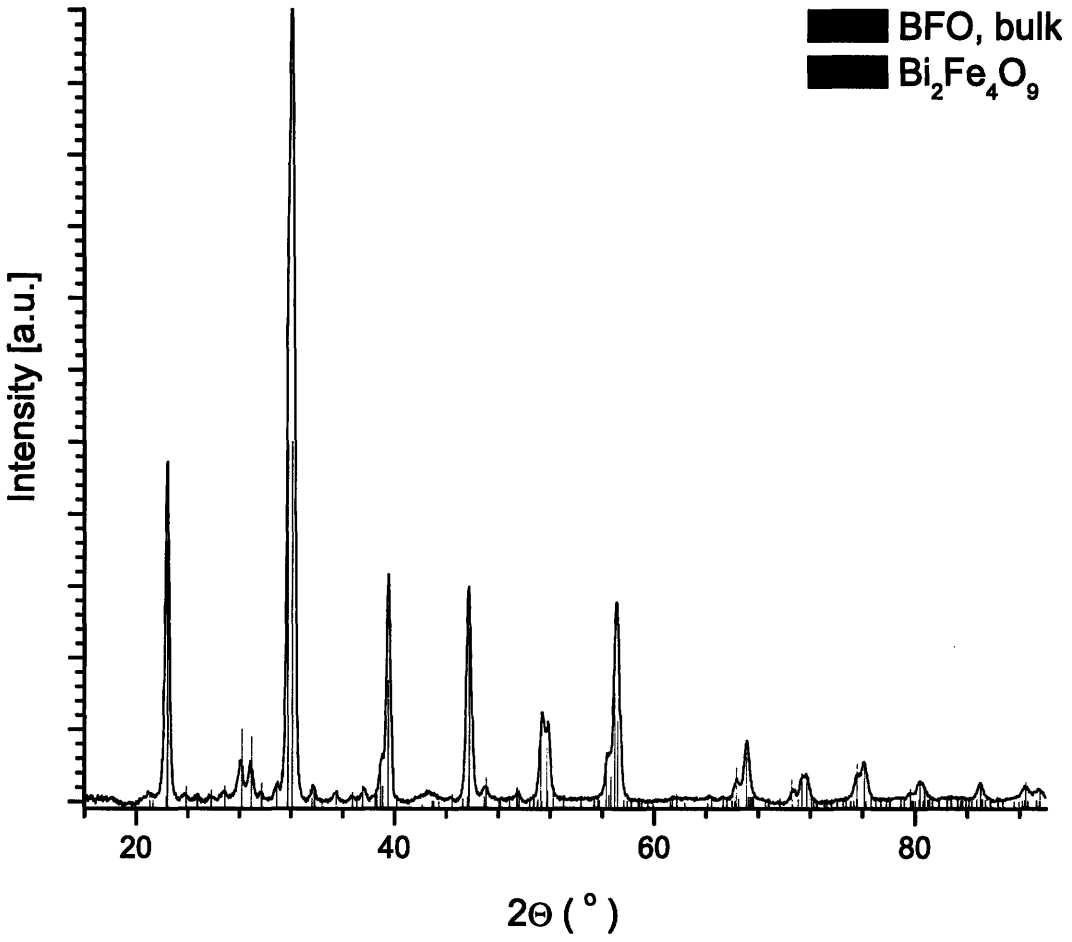

Figure 5-4: γ-integrated XRD intensity as a function of 2Θ for the sample shown in detail in Figure 5-3. XRD peaks for BFO (red) and $Bi_2Fe_4O_9$ (green) are shown for reference.

Bi:Fe ratio close to 1, empirically drive our films toward an ideal stoichiometry for forming the phase of interest. A 2DXRD pattern for this sample is shown in Figure 5-3, while its integrated intensity as a function of 2Θ is shown in Figure 5-4.[3] The former clearly shows the polycrystalline nature of the film since the rings are fairly uniform in γ, while the latter shows that the film is mostly composed of BFO, with

[3]It should be noted that the peak heights of the phases given in the figures provided henceforth are taken from published powder diffraction records. As such, the intensities of the peaks relative to one another in the same record are relavent when examining a polycrystalline film, or even one which is slightly textured. The peak heights relative to other records, however, are largely meaningless unless the sample is perfectly polycrystalline, in which case an RIR value can be used to compute a phase fraction. Hence, we have arbitrarily scaled the different phases' peak heights. Furthermore, for epitaxial or highly textured single phase samples, these peak heights are entirely meaningless, even within the same record, since texture will give preference to a particular peak direction, even one which does not diffract strongly in a powder sample.

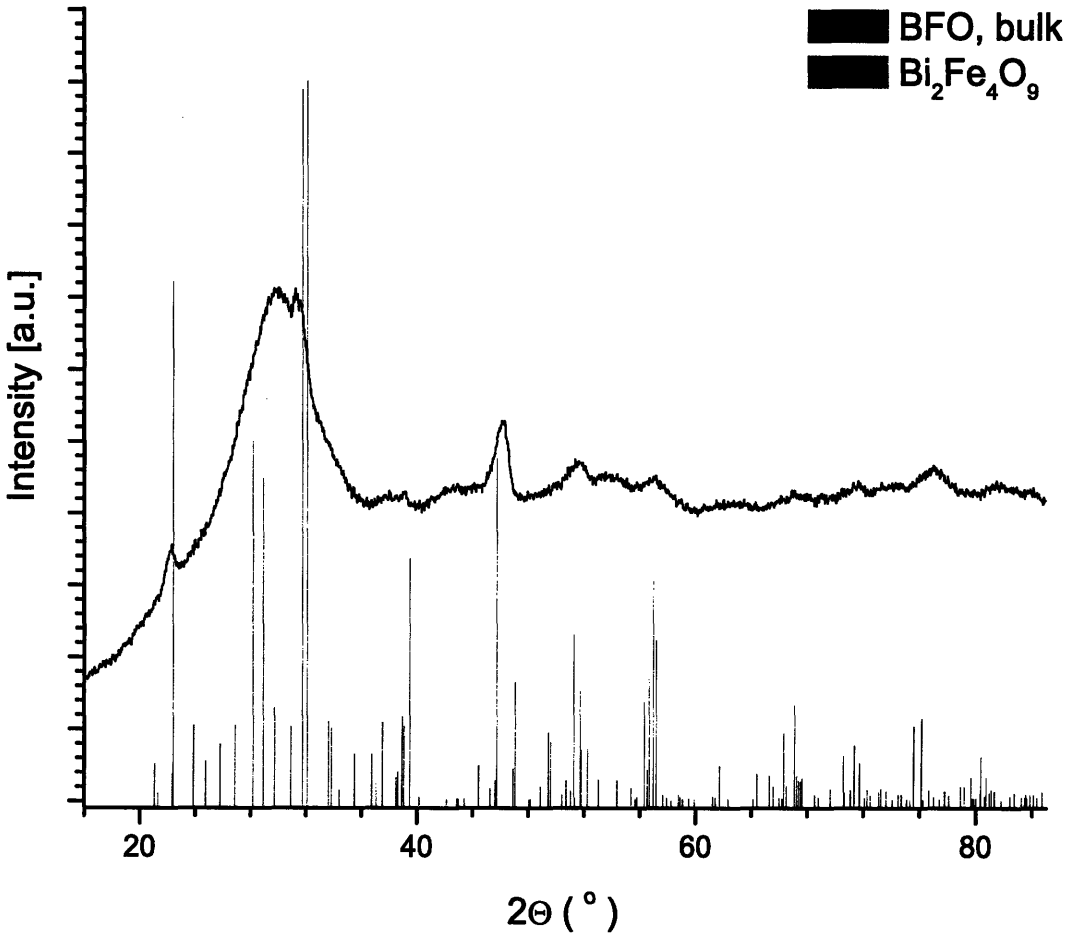

Figure 5-5: γ-integrated XRD intensity as a function of 2Θ for the NISA-NPDA sample deposited on MgO(001) at T_s = 680°C and p_{O_2} = 7.5 mTorr. The broad, amorphous hump is evident at low angle. XRD peaks for BFO (red) and $Bi_2Fe_4O_9$ (green) are shown for reference.

a minority phase of $Bi_2Fe_4O_9$.

NISA-NPDA samples are, unfortunately, not very useful because they result in "glassy" or amorphous material, as indicated in Table 5.2. Even a sample deposited at 680°C in 7.5 mTorr of oxygen, which showed some polycrystalline BFO growth, was mostly amorphous in character, as shown by the low angle glassy "hump" in Figure 5-5. The glassiness is, of course, a consequence of insufficient kinetics during growth to form a crystalline phase. It therefore becomes apparent that there must be some annealing, either ISA or PDA, in order to obtain a crystalline phase on MgO, even at the highest deposition temperatures.

The ISA-PDA samples, of PDA times ranging from 2.5 to 5 hrs at around 700°, on the other hand, present the opposite extreme of the NISA-NPDA samples. Here, there is *too much* annealing. While annealing is necessary to promote crystalline growth kinetics, annealing in excess can drive Bi out of the film due to its volatile nature. The film, then off stoichiometry, forms Bi-deficient phases like $Bi_2Fe_4O_9$ or, in extreme cases, Fe_3O_4. The phases of the ISA-PDA samples are shown in Table 5.3. In particular, looking in the 3.0 mTorr row, if we compare the 580°C and 630°C samples, which had identical PDA times of 4 hrs, we see that the effect of increasing the deposition temperature is to increase the presence of a Bi-deficient phase, i.e. to volatilize more Bi. Further evidence of this effect can be found in the WDS data for these two samples, which reveals that the Bi:Fe ratio for the former is 0.85, while that of the latter is 0.38. Thus, increasing deposition temperature is a double-edged sword, making the film more crystalline but simultaneously robbing it of Bi. Clearly, we need to find a happy medium between the two in order to grow BFO free of other phases.

The NISA-PDA samples, whose phases are shown in Table 5.4, present us with additional useful information. In particular, these were the only films made at high oxygen pressures. What we see is that at high pressures, the film not only contains BFO, but also a Bi_2O_3 phase. We would therefore expect our films to be rich in Bi. WDS confirms this data, giving a Bi:Fe ratio of 1.31 for the 580°C sample and 1.34 for the 630° sample. This extreme is the opposite of the vacuum situation. We have too much oxygen in the system which is keeping too much Bi in the film. This excess Bi phase separates as Bi_2O_3. Once again, we see the importance of picking an appropriate oxygen pressure on film stoichiometry and, hence, phase formation.

In summary, we see two main trends, both of which are confirmed in Figure 2-15 from [19]:

1. Oxygen pressure during deposition directly controls film stoichiometry and therefore phase formation by either allowing more Bi to volatilize away from the film (low pressure) or keeping more of it in (high pressure). At very low pressures, the Bi:Fe ratio is low, and we form iron oxide. At high pressures, the

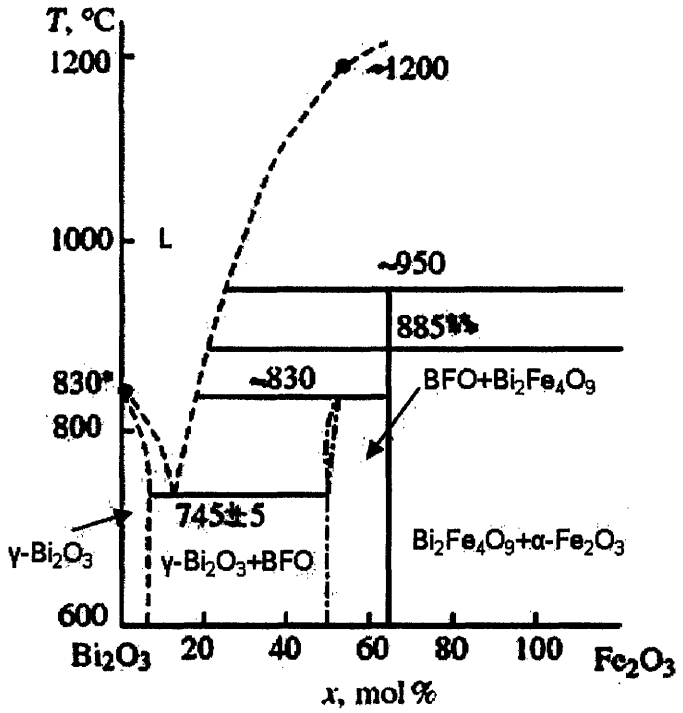

Figure 5-6: Equilibrium phase diagram of the bulk Bi_2O_3-Fe_2O_3 system, where x is the concentration of Fe_2O_3 in the system in mol%. We can also use it to write Bi:Fe $= -1 + 100/x$ [40].

Bi:Fe ratio is high, and we form bismuth oxide. In a regime between 3.0 mTorr and 7.5 mTorr, we seem to find Bi:Fe ratios close to 1 and BFO as the dominant phase; we, therefore, choose this pressure regime for our STO substrate samples.

2. Substrate temperature influences both film stoichiometry and crystallinity. Films deposited at low temperatures or which are not annealed long enough will be amorphous. Films deposited at high temperatures or which are annealed for too long will be Bi-deficient due to the volatile nature of Bi. The optimal temperature range, however, is not as easy to define as the optimal pressure range, since the former is always coupled into the annealing conditions. Although several optimal combinations of substrate temperature and annealing conditions probably exist, we will, on our STO samples, attempt to eliminate PDA both for

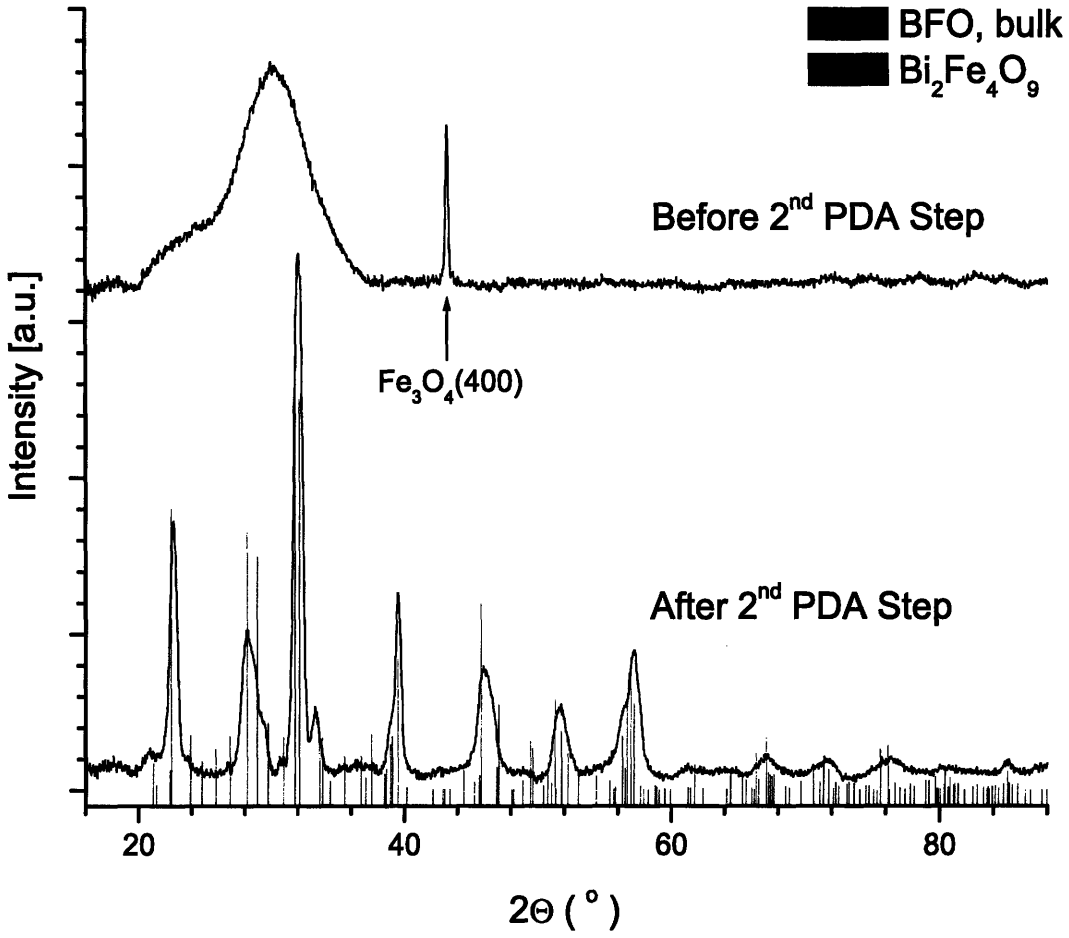

Figure 5-7: γ-integrated XRD intensity as a function of 2Θ for the NISA-PDA sample deposited on MgO (001) at T_s = 580°C and p_{O_2} = 7.5 mTorr before and after a second PDA step for 2.5 hr at 580°C. Crystallinity clearly increases, although the final pattern has a high impurity content. XRD peaks for BFO (red) and $Bi_2Fe_4O_9$ (green) are shown for reference.

practical reasons (it takes a lot of time!) and for consistency, since it is easier to reproduce an experiment which does not feature a PDA step. We therefore pick the highest temperature possible, 680°C, as our optimal temperature since we will be operating without PDA and need to give our samples the maximal odds of forming a perfect crystal. Any Bi-deficiency shall be corrected by increasing oxygen pressure during deposition.

These results are also consistent with the bulk equilibrium phase diagram of the Bi_2O_3-Fe_2O_3 system shown in Figure 5-6. Although PLD is by no means an equilib-

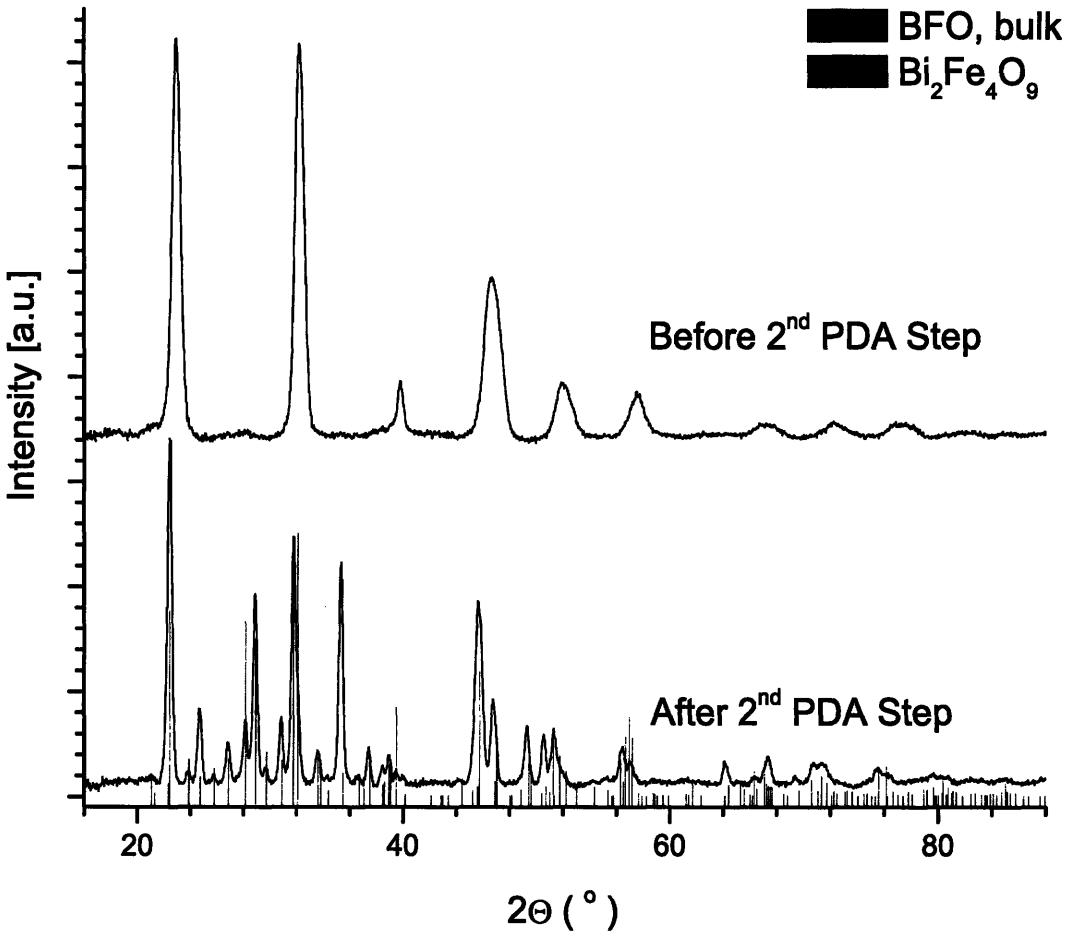

Figure 5-8: γ-integrated XRD intensity as a function of 2Θ for the NISA-PDA sample deposited on MgO (001) at T_s = 680°C and p_{O_2} = 7.5 mTorr before and after a second PDA step for 2.5 hr at 680°C. Crystallinity clearly increases, although the final pattern has a high content of secondary phases. XRD peaks for BFO (red) and $Bi_2Fe_4O_9$ (green) are shown for reference.

rium process, it is interesting to note certain relationships. According to the diagram, as long as we stay below 745°C, for a composition reasonably close to Bi:Fe = 1:1, we should form some BFO. Temperature, therefore, has a lesser influence on the growth kinetics and more of an influence on the stoichiometry of the film. As we use annealing to drive the film towards the right side of the diagram, we obviously form $Bi_2Fe_4O_9$ and iron oxide phases. We can, of course, obtain a similar result by using oxygen pressure to move ourselves horizontally on this graph as well.

5.1.2 Direct Examination of the Effect of Annealing

In order to illustrate directly the effect of annealing samples, we examine the integrated 2DXRD intensity as a function of 2Θ of two samples, both of which had a good deal of amorphous character even after PDA. These two samples were then given an *additional* PDA step in order to achieve crystallinity. In both cases, however, the detrimental effects of the second PDA step are apparent since the dominant phase in both films becomes the Bi-deficient $Bi_2Fe_4O_9$. The first sample, deposited at 7.5 mTorr and 580°C with a PDA of 2.5 hr at 580°C, as shown in Figure 5-7, is initially glassy with some Fe_3O_4 textured in the (400) direction; but, following a second PDA for 2.5 hr at 680°C, polycrystalline BFO forms, as well as $Bi_2Fe_4O_9$. The second sample, deposited at 7.5 mTorr and 680°C with a PDA of 2.5 hr at 680°C, as shown in Figure 5-8, is initially nanocrystalline BFO (as evidenced by the broad peak widths); but, following a second PDA for 2.5 hr at 680°C, $Bi_2Fe_4O_9$ becomes the dominant phase, although there is some polycrystalline BFO remaining, now of normal peak width. In both these cases, the effect of annealing is to increase crystallinity, but at the expense of film stoichiometry and, hence, desirable phase formation.

5.2 $BiFeO_3$ on $SrTiO_3$ (001) Substrates

5.2.1 Optimization of Growth Conditions

Many of the same phase formation trends observed on MgO (001) substrates were also observed on $SrTiO_3$. ISA-PDA samples, for instance, consistently showed the presence of the Bi-deficient $Bi_2Fe_4O_9$ phase, most likely due to Bi volatilization during either or both of the annealing steps. Integrated 2DXRD patterns as a function of 2Θ for ISA-PDA samples grown at 580°C and three different pressures all show the presence of this phase, as shown in Figure 5-9.[4]

NISA-PDA samples taken at 630°C, oppositely, seem to suffer from a lack of kinetics. The 2DXRD patterns comparing samples fabricated at 3.0 mTorr, 7.5 mTorr,

[4]It should be noted that all XRD plots which refer to the BFO (00ℓ) direction are referring to the pseudocubic direction.

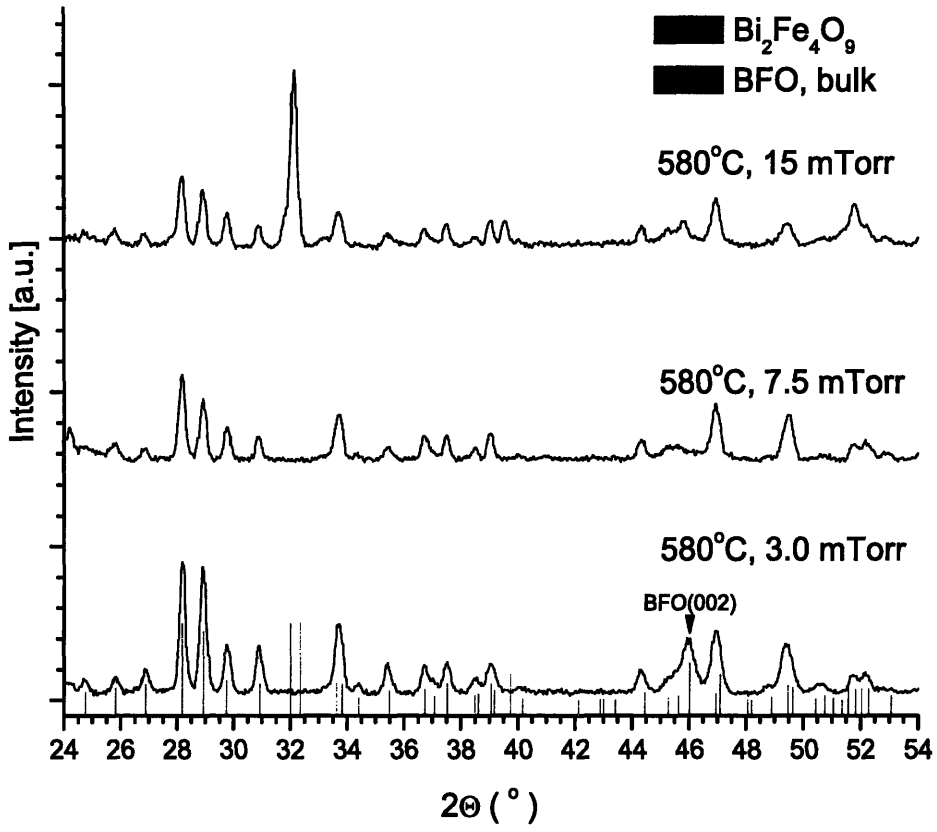

Figure 5-9: γ-integrated XRD intensity as a function of 2Θ for the ISA-PDA samples deposited on STO (001) at T_s = 580°C and p_{O_2} = 3.0 mTorr, 7.5 mTorr, and 15 mTorr. XRD peaks for BFO (red) and $Bi_2Fe_4O_9$ (green) are shown for reference and the epitaxial direction is indicated.

and 15 mTorr are all shown for comparison in Figure 5-10. From the 2DXRD patterns, we can see 4 different morphologies of BFO. In (a), there is a textured BFO hump that is relatively broad in 2Θ and is therefore somewhat amorphous. In (b), there is what we call an epitaxial BFO (e-BFO) peak in the (001) direction as well as partial rings which indicate an additional, textured BFO (t-BFO) phase.[5] In (c), there is only a polycrystalline BFO phase. Integrated patterns as a function of 2Θ,

[5]We are aware of the ambiguity of terms like "epitaxial" and "textured" in this context. Suffice it to say that by textured we mean that the ring intensity is not a uniform function of γ and that epitaxial is a special case of this wherein the values of γ over which the intensity is non-zero are closely related to those over which the substrate diffracts. We will make this criterion quantitative subsequently when we discuss rocking curves in χ, ω, and ϕ for pure, e-BFO samples.

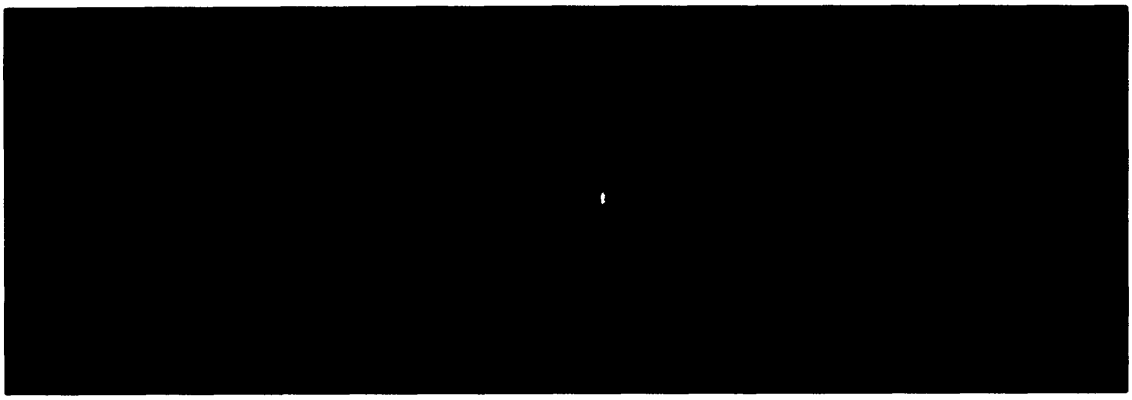

Figure 5-10: 2DXRD pattern for the NISA-PDA samples deposited on STO (001) at $T_s = 630°C$ and (a) $p_{O_2} = 3.0$ mTorr ($2\Theta_g = 38°$), (b) $p_{O_2} = 7.5$ mTorr ($2\Theta_g = 42°$), and (c) $p_{O_2} = 15$ mTorr ($2\Theta_g = 43°$). These patterns were taken while rotating in ϕ, with $\omega = 2\Theta_g/2$, and $\chi = 90°$. The different morphologies of BFO are shown by arrows: glassy BFO in (a), epitaxial BFO (e-BFO) and textured polycrystalline BFO (t-BFO) in (b), and polycrystalline BFO in (c).

shown in Figure 5-11, confirm these observations as well as the presence of sillenite ($Bi_{12}MO_{20-\delta}$, where M is a tetravalent ion or combination of ions that averages to 4+ and δ can be slightly positive or negative; space group $I23$, isomorphic to γ-Bi_2O_3 [92]) in the 15 mTorr sample. Because sillenites are Bi-rich phases, we expect them to form at high oxygen pressures where Bi is present in the film in excess. Furthermore, all of these samples show a lack of kinetics since each contains either glassy BFO or polycrystalline BFO, neither of which is the lowest energy state of the system.

ISA-NPDA samples also showed polycrystalline BFO phases, although, when we compare two samples both made at 3.0 mTorr, but at 630°C and 680°C respectively, we see that the former only has BFO phases (e-BFO with some polycrystalline BFO) while the latter has $Bi_2Fe_4O_9$ in addition to polycrystalline BFO. Thus, we see the trend of increasing temperature leading to increased Bi volatilization we saw in the MgO samples. Integrated 2DXRD patterns of these samples may be found in Figure 5-12.

The only class of samples for which we were able to grow pure, e-BFO was the NISA-NPDA class. The optimal deposition conditions turn out to be $T_s = 680°C$ and $p_{O_2} = 7.5$ mTorr. This combination of a high substrate temperature and medium

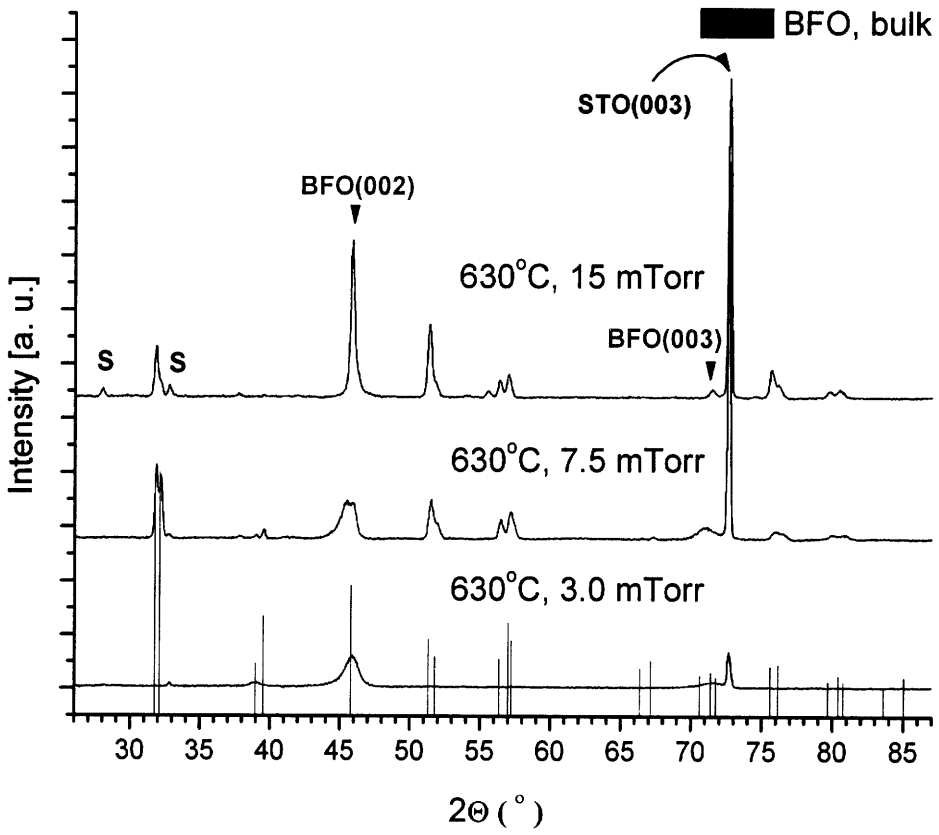

Figure 5-11: γ-integrated XRD intensity as a function of 2Θ for the NISA-PDA samples deposited on STO (001) at T_s = 630°C and p_{O_2} = 3.0 mTorr, 7.5 mTorr, and 15 mTorr. XRD peaks for BFO (red) are shown for reference and the epitaxial directions are indicated. The STO (003) substrate also appears at high angles and is indicated. "S" marks sillenite peaks in the 15 mTorr sample.

pressure allows us to both provide sufficient kinetics during growth so that annealing is not required and control the Bi:Fe ratio, keeping it close to 1. Frames showing the e-BFO (002), (003), and (004) peaks may be found in Figure 5-13. Finally, an integrated pattern in 2Θ may be found in Figure 5-14.

Because of the work done in [20] (see Section 2.2.3), we know it is important to examine high angle data for our film more carefully to make sure there is no ferrimagnetic γ-Fe_2O_3 phase present. According to this paper, we should find the BFO (004) peak somewhere between $2\Theta = 100°$ ($\omega = 50°$) and $2\Theta = 102.5°$ ($\omega = 51.25°$),

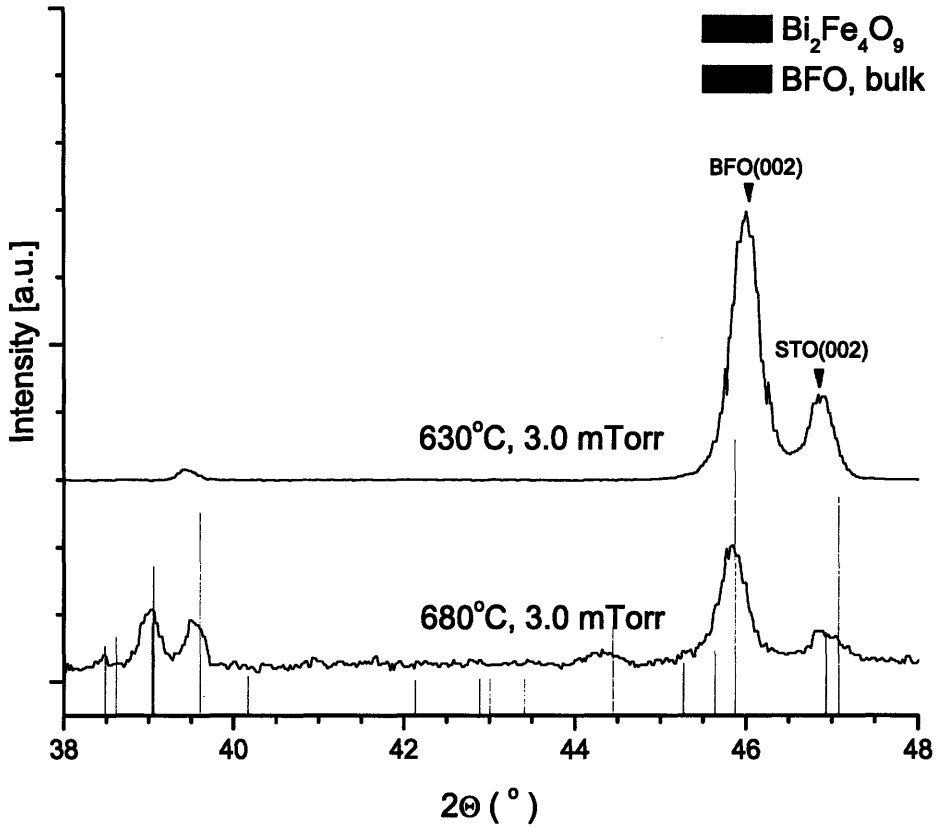

Figure 5-12: γ-integrated XRD intensity as a function of 2Θ for the ISA-NPDA samples deposited on STO (001) at p_{O_2} = 3.0 mTorr and T_s = 630°C and 680°C. XRD peaks for BFO (red) and $Bi_2Fe_4O_9$ (green) are shown for reference and the epitaxial directions are indicated. The STO (002) substrate also appears.

while we should find the γ-Fe_2O_3 (008) somewhere between $2\Theta = 95°$ ($\omega = 47.5°$) and $2\Theta = 97.5°$ ($\omega = 48.75°$). As shown in Figure 5-15, setting the diffraction condition to $\omega = 50°$ reveals what we believe to be the BFO (004) peak. However, setting the diffraction condition to $\omega = 47.5°$, for which γ-Fe_2O_3 (008) should diffract, yields no signal.[6] We therefore conclude, based on 2DXRD phase analysis, that this film is pure e-BFO in the (00ℓ) pseudocubic direction.

[6]We also experimented with many different values of ω in this range and were still not able to find the γ-Fe_2O_3 (008) peak.

Figure 5-13: 2DXRD pattern for an NISA-NPDA sample deposited on STO (001) at $T_s = 680°C$ and $p_{O_2} = 7.5$ mTorr. Frames were taken at (a) $2\omega = 44°$ to see the (002) peak, (b) $2\omega = 71°$ to see the (003) peak, and (c) $2\omega = 100°$ to see the (004) peak. These patterns were taken while rotating in ϕ, with $\omega = 2\Theta_g/2$, and $\chi = 90°$, with the exception of (c) where $2\Theta_g = 90°$ because of instrumental limitations. Because the detector has a width of $\pm 15°$ in 2Θ, however, we were still able to see the (004) peak at $2\Theta = 100°$ by setting $\omega = 50°$.

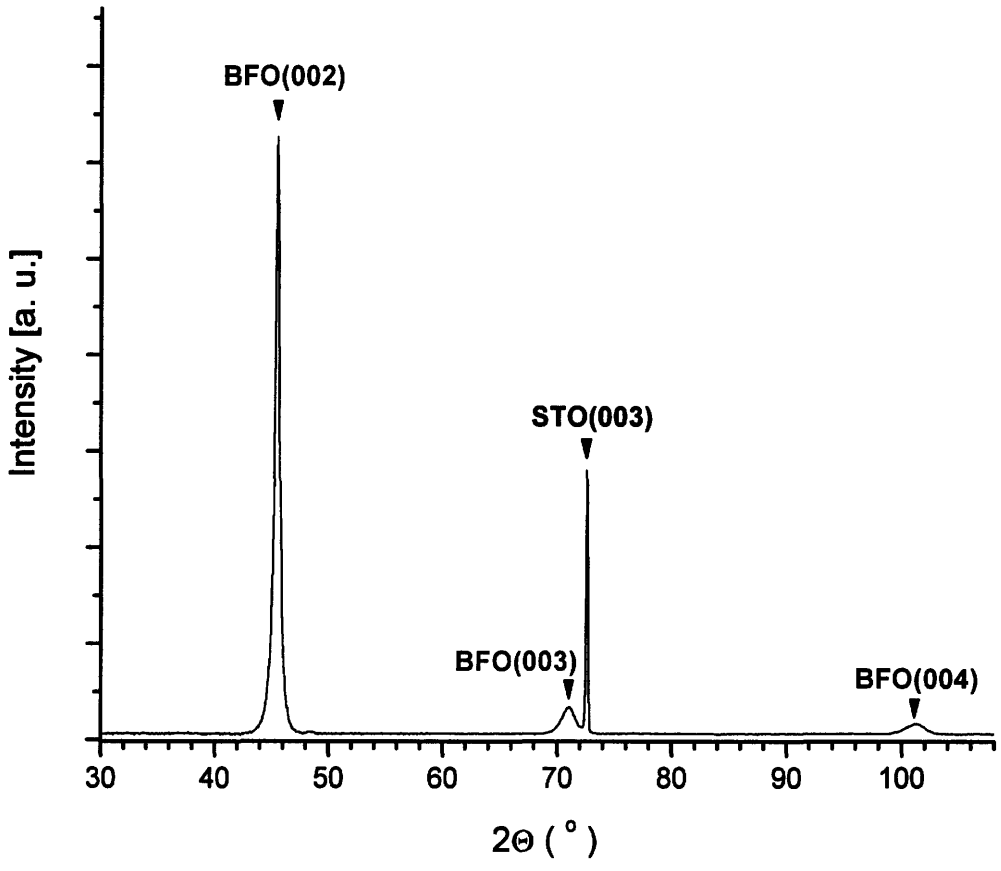

Figure 5-14: γ-integrated XRD intensity as a function of 2Θ for NISA-NPDA samples deposited on STO (001) at $p_{O_2} = 7.5$ mTorr and $T_s = 680°C$. The epitaxial BFO peaks are indicated in red. The STO (003) substrate also appears.

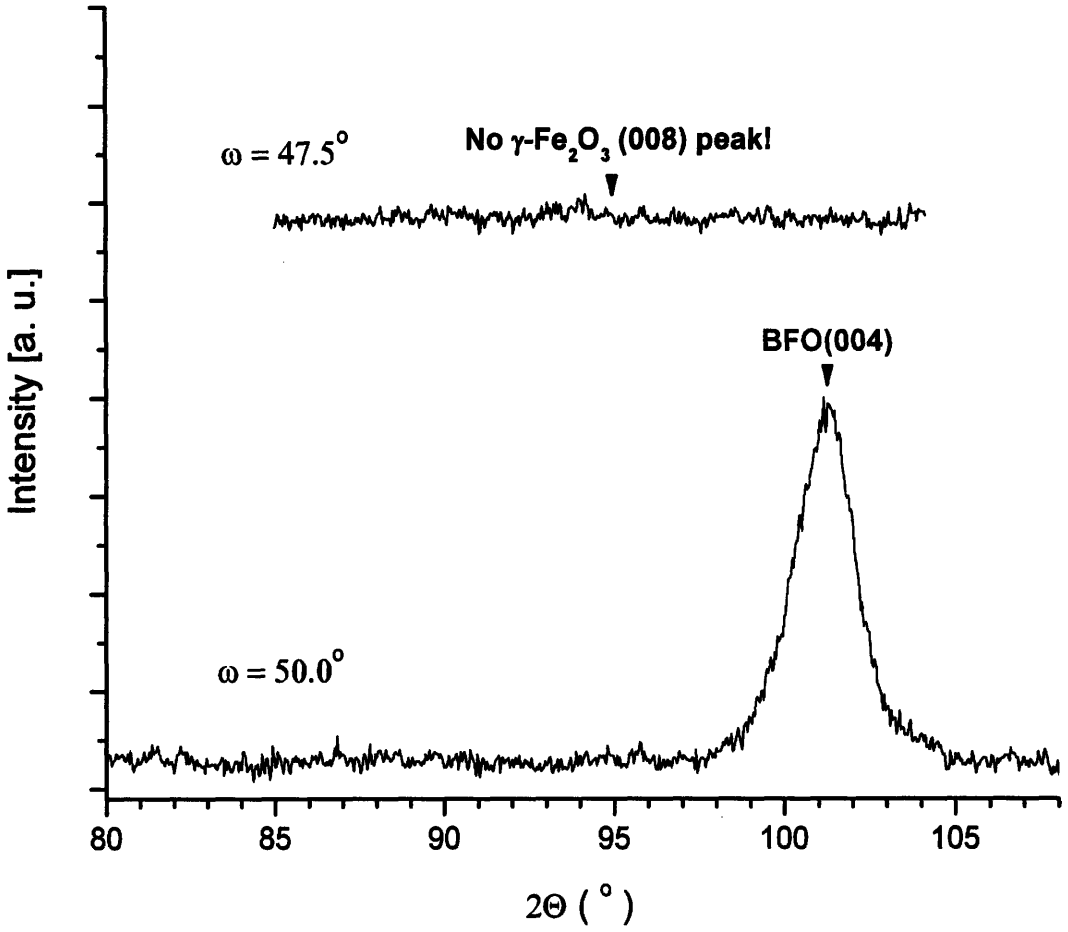

Figure 5-15: γ-integrated XRD intensity as a function of 2Θ for NISA-NPDA samples deposited on STO (001) at $p_{O_2} = 7.5$ mTorr and $T_s = 680°C$, with only high angle data shown. The epitaxial BFO peak is indicated in red. We chose $\omega = 50°$ on the bottom plot so that BFO (004) would diffract, and we chose $\omega = 47.5°$ on the top plot so that γ-Fe_2O_3 (008) would diffract. We see the former, but not the latter.

5.2.2 Structural Characterization

We executed rocking curves in both the ω and γ dimensions about the (003) reflection of this BFO sample with respect to the underlying STO substrate. The former, with a FWHM of 2.873° and 0.466° for BFO and STO respectively, is shown in Figure 5-16, while the latter, with a FWHM of 3.1674° and 0.323° for BFO and STO respectively, is shown in Figure 5-17. In each case, the film has an angular dimension which is approximately 10 times wider than that of the substrate.

The films themselves had a RMS roughness that varied between 6 to 12% of the total film thickness. We consider this roughness to be acceptable given the fact that

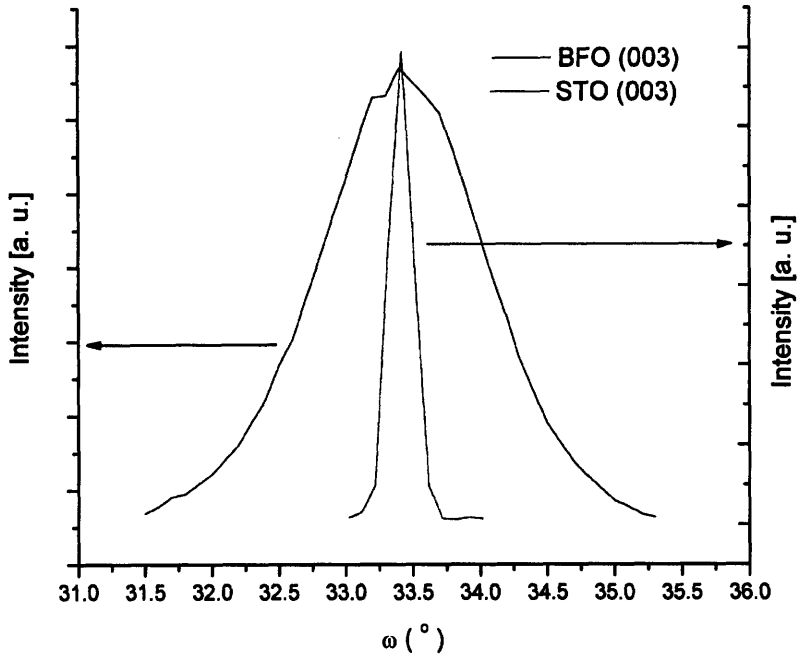

Figure 5-16: Rocking curve in ω for a BFO sample about its (003) reflection as well as the corresponding reflection in the underlying STO substrate.

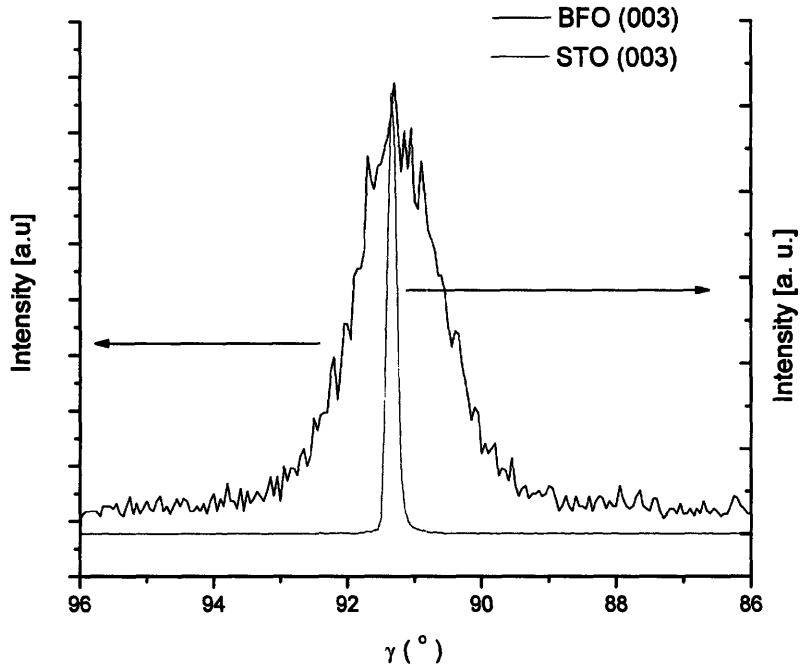

Figure 5-17: Rocking curve in γ for a BFO sample about its (003) reflection as well as the corresponding reflection in the underlying STO substrate.

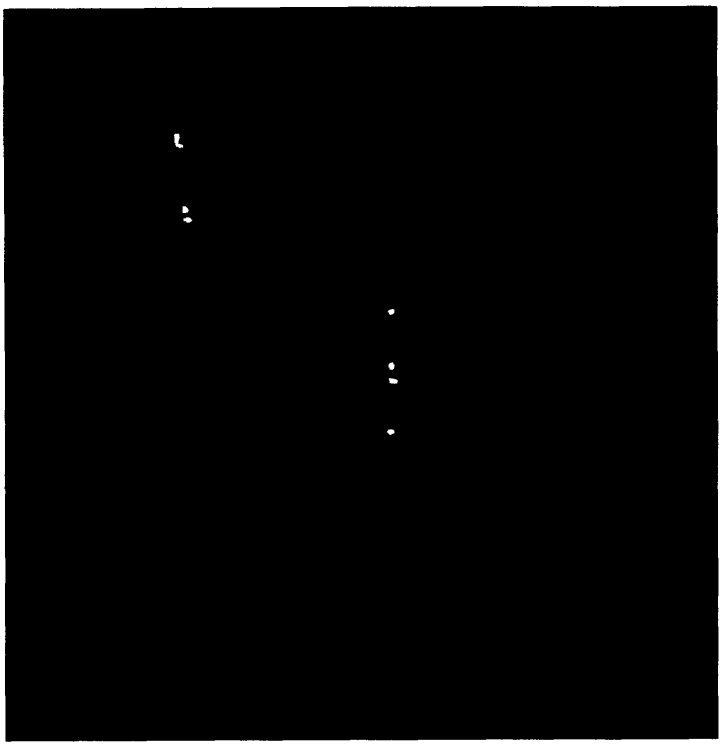

Figure 5-18: A 2DXRD scan of an epitaxial (or very highly textured) BFO sample grown on STO (001) with $\chi = 45°$. One can clearly see 3 BFO peaks at different values of γ and 2Θ, each adjacent to a reflection (smaller dots) from the substrate.

we never optimized our deposition conditions with this criterion in mind. In future film growth, however, the roughness could be controlled by optimizing both pulse rate and energy per pulse of the excimer laser.

Although attempts were made to more fully characterize the crystal structure and lattice parameters of these BFO films, the instrumental limitations of the 2D diffractometer, which is not a high-resolution instrument, prevented us from doing so to a high degree of accuracy. We were, however, able to do some analysis on one of our samples.

We began by examining the (00ℓ) peaks for a $\chi = 90°$ scan and choosing an optimal d_{001} based on these. Essentially, at this point, we assumed the material was cubic in the (001) direction. We then examined the peaks that show up when $\chi = 45°$, shown in Figure 5-18. When we integrated this pattern over γ and compared it to the integrated pattern taken over the same range in 2Θ but for $\chi = 90°$, as shown in

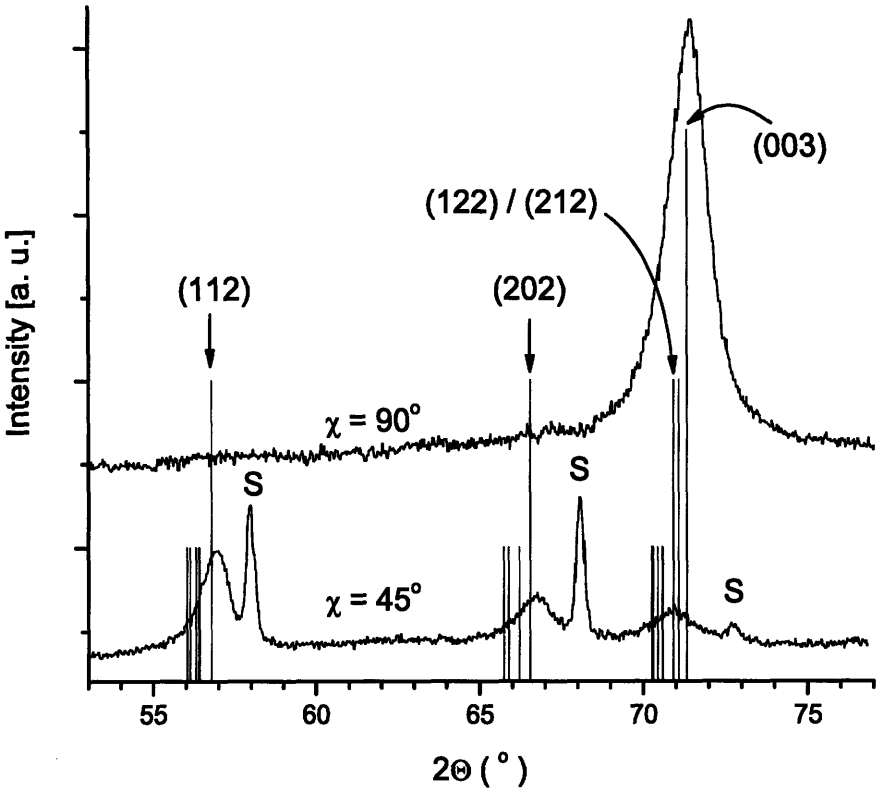

Figure 5-19: Integrated 2DXRD data for $\chi = 90°$ and $\chi = 45°$ for the BFO sample on STO (001). We can see that the (003) peak does not line up with any of the off-angle peaks near it, implying a non-cubic lattice. Only those peaks which appear in either diffraction pattern are labeled. The others should show up at another value of χ. Substrate peaks are labeled with an "S."

Figure 5-19, we saw that the (003) peak was not at the same location as the (221) (which belongs to the same family of peaks indexed by (122)/(212) in the figure). What this data implies is that the structure is not cubic, for, in a cubic system, these two crystal planes have the same spacing. We therefore chose to perturb our formerly cubic hypothesis in a tetragonal manner, i.e. elongating the in-plane parameter, until the (221) aligned with its reflection. The (003), of course, did not move since we were only changing the in-plane parameter. We then noticed that, although the (221) and (003) were aligned, the other two peaks were not. We subsequently made another perturbation and introduced a monoclinic deformation angle β. We then adjusted β, $a = b$, and c to get the best fitting monoclinic pattern we could find.

After some analysis, we indexed the peaks we found by examining a stereographic projection and found them to be the (112), (202), and (122)/(212) peaks. We found these peaks to have interplanar spacings of $d_{112} = 1.6149$ Å, $d_{202} = 1.4002$ Å, and $d_{122/212} = 1.3274$ Å, respectively. Finally, we took the lattice parameters we found by trial and error and used them as starting values for a non-linear fitting algorithm (implemented in Mathematica via the `FindRoot` function) that solved the equation

$$d_{hk\ell} = \frac{a \sin\beta}{\sqrt{h^2 + k^2(a \sin\beta/b)^2 + \ell^2(a/c)^2 - 2h\ell(a/c)\cos\beta}}$$

for each of the above d-spacings to find the variables $a = b$, c, and β. Through this analysis, we determined that $a = b = 4.037$ Å, $c = 3.947$ Å, and $90° - \beta = -0.88°$. When we compare these findings to those for the (001) oriented film in Table 2.3, we find a decent match of approximately 1% for $a = b$ and c, especially considering the low resolution of our diffractometer. In the future, we would benefit from the supplemental use of a high resolution diffractometer that is capable of more accurate cell refinement. Nevertheless, because our results are so close to those published, we have little doubt that our BFO films have the known monoclinic structure.

5.2.3 Magnetic Characterization

We characterized the magnetic properties of a BFO film by first measuring a hysteresis loop for $|H| < 10$ kOe for a bare STO (001) substrate and then subtracting that signal from the BFO film, which is obviously on an STO substrate of its own. By doing so, we remove the diamagnetic contribution of both the STO and the sample holder and arrive at the M-H hysteresis loop shown in Figure 5-20. Although the loop clearly does not saturate, which is to be expected given the discussion in Section 2.2.3, we can effectively define our M_s to be the magnetization at the highest field we can apply, 10 kOe. In that case, $M_s \approx 1.2$ emu/cm^3, which is slightly lower than, but definitely on the order of magnitude of, other groups' measurements for thicker films. It should also be noted that the loop shows no remanence, a function of the spiral structure of the magnetic moments in the material.

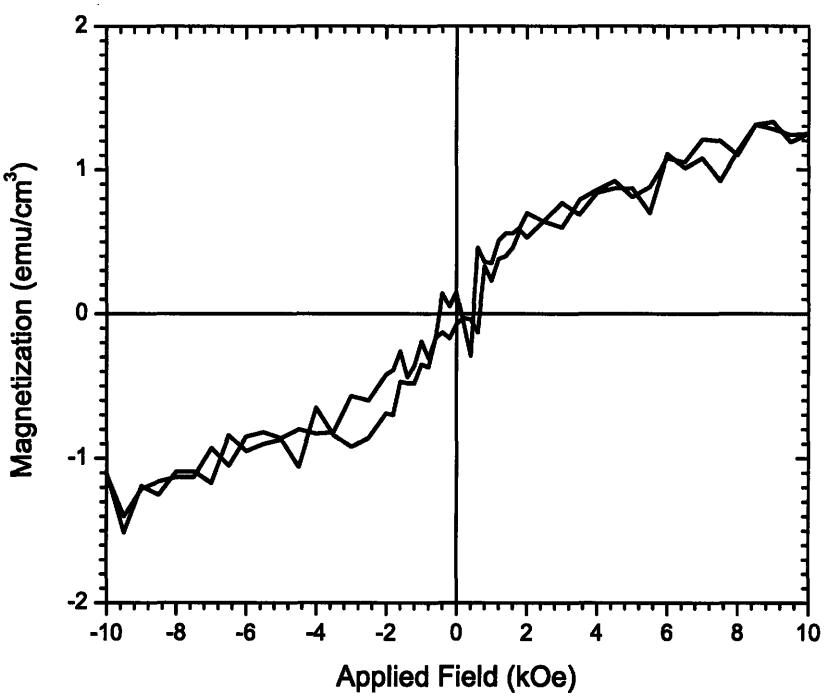

Figure 5-20: *M-H* hysteresis loop for a BFO sample 269 nm thick grown on STO (001) at $T_s = 680°C$ and $p_{O_2} = 7.5$ mTorr. Note that the loop is quite noisy due to the low magnetization and that the loop never saturates.

5.2.4 Optical Characterization

The optical absorption spectra of three BFO films were measured by two different methods, conventional photospectroscopy and spectroscopic ellipsometry. Two films of thicknesses 269 nm and 811 nm were measured by the former method and one film of thickness 446 nm was measured by the latter. The absorption spectra $\alpha(\lambda_0)$ for all three are shown in Figure 5-21. Unfortunately, the former method is plagued by thin film interference effects which cause oscillations in the spectrum. The thicker sample, as expected, oscillates with a smaller period. The ellipsometric measurement, although it does not show interference oscillations, does not accurately model the bandgap at low wavelength. In addition, it was very difficult to fit the ellipsometric data to a dispersion model, which is why we only have reliable ellipsometric data for one sample.

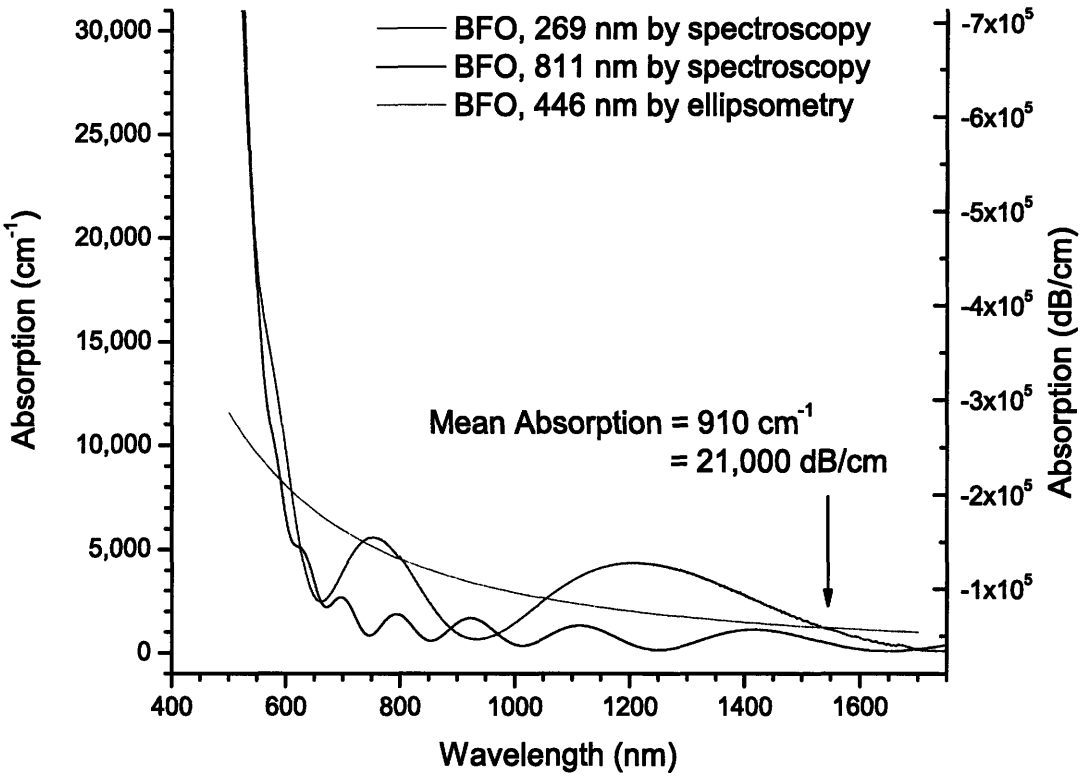

Figure 5-21: Absorption spectra of three BFO films, two measured with spectroscopy (thicknesses of 269 nm and 811 nm) and one measured with spectroscopic ellipsometry. The mean absorption at 1550 nm is indicated in the figure.

Since both methods clearly have their drawbacks, we simply averaged all three measurements at our wavelength of interest, 1550 nm, to arrive at a mean absorption of $\alpha = 910$ cm^{-1} or 2.1 dB/μm.[7] This absorption is much higher than what we expected for BFO since, theoretically, the only thing that makes BFO different from bismuth iron garnet, from an absorption perspective, is that BFO lacks the tetrahedral Fe^{3+} that the garnet has. This fact should make BFO even *more* transparent than the garnet since there are no octahedral Fe^{3+} transitions anywhere near 1550 nm and there are no tetrahedral Fe^{3+} present in the material. The only reasonable explanation for this high absorption, therefore, is the presence of Fe^{2+} and/or Fe^{4+}. As discussed

[7]This value of α corresponds to a value of k, the imaginary part of the index of refraction, of 0.0112. Ellipsometry gives a value of the real part of the index n of 2.649 at this wavelength, as well.

in [74], the presence of Fe^{2+}, which is introduced during a deposition under reducing conditions, can cause absorption on the order of several thousand cm^{-1}. In the case of maghemite (γ-Fe_2O_3), $\alpha \approx 80,000$ cm^{-1} at 1550 nm. Our absorption is obviously much lower than that, but nevertheless it stands to reason that even a small amount of Fe^{2+} could drive the absorption up to levels much higher than that of an iron garnet (on the order of 0.1 cm^{-1}). In fact, instead of having Fe^{2+} scattered uniformly throughout the structure, our BFO films may even possess a very thin layer of iron oxide on the surface that is causing this absorption. A simple calculation reveals that, even if we have a layer of γ-Fe_2O_3 which is 1% of the total thickness, a BFO film with a hypothetical absorption of 0.1 cm^{-1} will look like it has $\alpha = 910$ cm^{-1}. This is indeed a very small layer to control when we are growing films with thicknesses of several hundred nanometers.

Going forward, we must get to the bottom of these optical absorption quandaries. X-ray photospectroscopy (XPS) with ion beam etching could be used to do a depth profile in our films of the stoichiometry and valence of the various elements present. Any changes in the surface layer would then be obvious. In addition, we would learn a great deal more about the valences of the Fe atoms in particular, which would help us resolve this absorption issue.

5.2.5 Magneto-Optical Characterization

Despite the assumed birefringence present in BFO (although we neglected to measure it directly), we were able to measure some Faraday rotation in our thickest BFO film (811 nm). Because we could not saturate the BFO film, we did not observe a Faraday hysteresis loop, as in [27] for the Fe:$BaTiO_3$ system. We were able, however, to observe a non-trivial linear dependence of the BFO film on the field of the form

$$\theta/z = VH$$

where z is the sample thickness, H is the applied field, and V is the so-called Verdet constant of the material. We found V by performing linear regressions on data

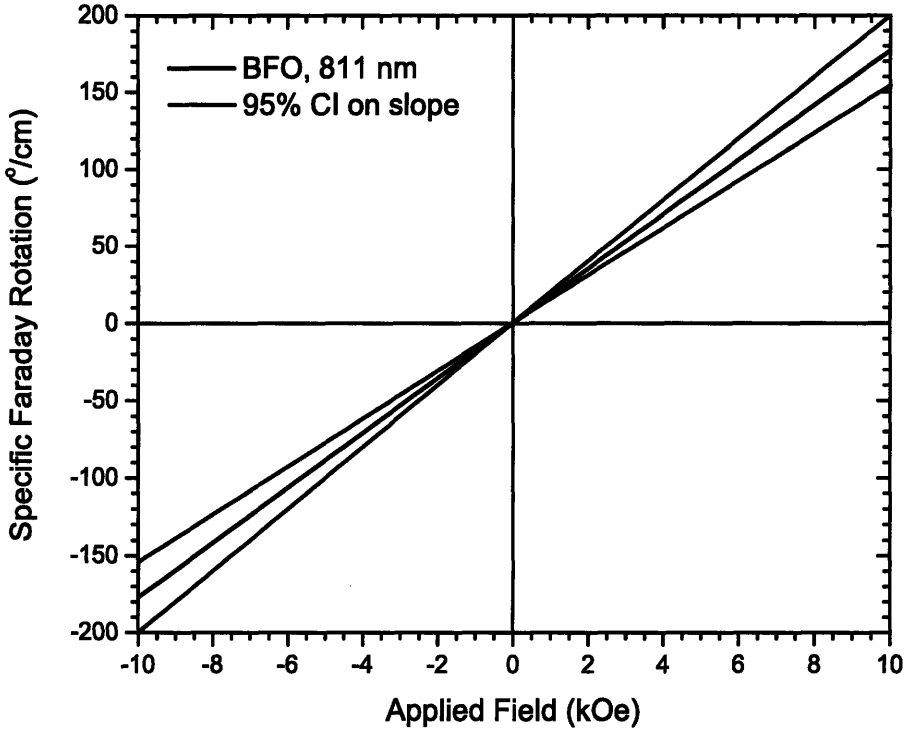

Figure 5-22: The results of linear regression analysis on the measured specific Faraday rotation in an 811 nm thick BFO film on STO (001). The black line is the mean slope, while the red lines represent a 95% confidence interval on that parameter calculated using the sum in quadrature of the standard errors of the individual regressions.

from both the BFO film on STO and on a bare STO substrate.[8] We then subtracted one from the other and added the standard errors of these measurements in quadrature. After normalizing by the thickness of the sample, we found that $V = 17.7 \pm 2.28°/(\text{cm}\cdot\text{kOe})$, which is about a factor of 50 smaller than many garnets at this wavelength [93]. In fact, the garnets in [93] saturate at around 1.8 kOe with a specific Faraday rotation of at most 1617°/cm, while our film has a specific Faraday rotation of only 32°/cm at the same field. We plot our fitted values as a function of applied field H in Figure 5-22.

We explain the low specific Faraday rotation of our BFO films by citing the low magnetization in the film (about 1 emu/cm^3), even at high field. Even though BFO

[8]These linear regressions each had R^2 values of more than 0.99.

has octahedrally coordinated Fe^{3+}, which has the correct electric dipole transition to provide significant Faraday rotation at 1550 nm, it does not have the internal magnetic field to line up the moments of the Fe^{3+} so that they execute this transition coherently. In fact, these moments are antiferromagnetically aligned, which is the opposite of the ideal case. Hence, without a strong ferri- or ferromagnetic internal field, there can be no buildup of Faraday rotation; we should not be surprised that a material that is so weakly magnetic has a weak specific Faraday rotation.

Finally, in light of the fact that we have such low Faraday rotation and high optical absorption at 1550 nm, we should expect the magneto-optical figure of merit F_Θ to be fairly low. Indeed, it has a value of 0.0015°/dB (or 0.035°), which is almost insignificant. Clearly, future research will have to work towards understanding not only the source of the high absorption in our samples, but also how to modify BFO to increase its magnetization, thereby increasing the net Faraday rotation of the material. We will briefly address some of these future ideas in the following chapter.

Chapter 6

Future Work & Conclusions

We have thus far reported, amongst other measurements, what we believe is the first magneto-optical characterization of $BiFeO_3$ (BFO). As stated in the previous chapter, we are not surprised that it exhibits little specific Faraday rotation because of its low internal magnetic field caused by the antiferromagnetic coupling of the Fe^{3+} cations. However, we emphasize that BFO is simply the first step in a long process of optimizing a generalized perovskite with high Faraday rotation and low optical loss. In this chapter, we therefore not only summarize our work, but also discuss future work, some already underway, involving substituted perovskites.

6.1 A- and B-Site Perovskite Substituents

6.1.1 $BiFe_{0.5}Mn_{0.5}O_3$ and Surface Effects

In order to achieve a non-trivial internal magnetic field in our material, we decided to substitute other transition metals besides Fe on the B-site of BFO. The objective of doing so was to change the antiferromagnet into a ferrimagnet. Because the material would then have two sublattices with oppositely aligned spins of different magnitudes, an internal magnetic field would be produced which would line up the remaining Fe^{3+} cations so that Faraday rotation could be executed coherently. We postulated that the tradeoff in lowering the number of Fe^{3+} per unit volume would be well worth

this increase in magnetic field. Futher discussion of this concept and examples of mixed-cation perovskites with high theoretical potential for magnetism and Faraday rotation at infrared wavelengths can be found in [94].

After experimenting with Mn, Co, and Ni, all of which have been shown to form perovskites with Bi on the A-site [95, 96, 97], we found the most success with the material $BiFe_{0.5}Mn_{0.5}O_3$ (BFM).[1] We believe that the $BiFeO_3$-$BiMnO_3$ system should form a solid solution for many values of the cation ratio Fe:Mn, especially since $BiFe_{0.7}Mn_{0.3}O_3$ has already been produced in bulk [98] and $LaFe_{0.5}Mn_{0.5}O_3$ has been grown on STO (111) by PLD [99]. Since Mn^{3+} has a 0 K magnetization of 4 μ_B and Fe^{3+} has a 0 K magnetization of 5 μ_B, we expect a compound with Fe:Mn = 1 to have a maximum magnetization of 0.5 μ_B per unit cell or about 75 emu/cm^3, assuming the Mn^{3+} and the Fe^{3+} align oppositely.[2] Furthermore, because Mn^{3+} has only 4 d electrons to fill 5 d orbitals, it is naturally an ion of low symmetry. This fact results in the so-called Jahn-Teller effect (first reported in [100]), in which the outer Mn^{3+} d level is split. Such a splitting and symmetry breaking may be advantageous in our case because they may promote alignment of the Fe^{3+} moments in a particular direction. Experimental evidence for the Jahn-Teller effect in other perovskites like $La_{0.65}Ca_{0.35}MnO_3$ is given in [101]. The one unfortunate consequence of substituting Mn on the B-site, however, is that doing so lowers the Curie or Néel temperature. For example, $BiMnO_3$ has a $T_C = 97$ K [95], $LaFe_{0.5}Mn_{0.5}O_3$ has a $T_C = 380$ K [99], and BFO has a $T_N = 643$ K and $T_C = 1123$ K [102].

One of our researchers, Lei Bi, characterized a BFM film on STO (001) with 2DXRD. His results, displayed in Figure 6-1, clearly show the (003) peak of a highly textured BFM film grown on STO (001). We also notice, however, that there seems to be another texture orientation which is about 20° in ϕ away from the epitaxial direction. The origins of this peak, plotted in red in the figure, are somewhat of a

[1] WDS reveals that the actual composition is closer to $Bi_{1.07}Fe_{0.51}Mn_{0.49}O_{3-\delta}$, where $\delta = 0.105$ is assumed to create charge neutrality to compensate the extra Bi^{3+} in the lattice.

[2] The system will probably be more complicated, however, perhaps involving a mixture of di- and trivalent Fe and di-, tri-, and tetravalent Mn. Because of the mixture of these various valences in $LaFe_{0.5}Mn_{0.5}O_3$ grown on STO (111), for instance, a saturation magnetization of 1.5 μ_B per unit cell can be obtained, which is higher than that of the pure ferrimagnetic case [99].

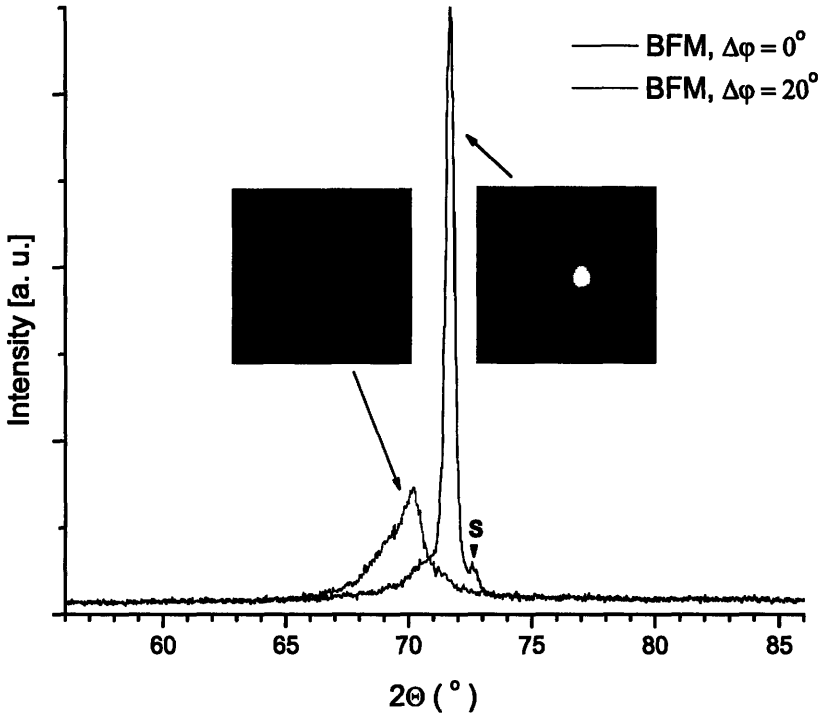

Figure 6-1: γ-integrated XRD intensity as a function of 2Θ for a BFM film on an STO (001) substrate taken at 2 different values of ϕ, one with ϕ aligned along the STO (001) axis (black) and one with ϕ 20° away from the previous value (red). Also indicated are the 2DXRD patterns for these peaks. The substrate peak is indicated by an "S."

mystery; but a reasonable explanation may be that there is a secondary, nanocrystalline phase with a larger d_{001} spacing than the dominant BFM phase. Whether this secondary phase is a perovskite or a sillenite, the two most likely candidates, is yet to be determined. Regardless, we see no other phases besides these two at any angle, which means that we have successfully grown BFM, even if our sample is not single phase.

An interesting property of this film, first revealed by X-ray Photoelectron Spectrometry (XPS), is that, on its surface, the A- to B-site ratio (i.e. the Bi:(Fe+Mn) ratio) is greater than 4. This result is in stark contrast with the WDS (bulk) data, which shows that Bi:(Fe+Mn) = 1.07 and Fe:Mn = 0.97 on average. To attempt to resolve this issue, we used a high-resolution Scanning Auger Nanoprobe (SAN) with

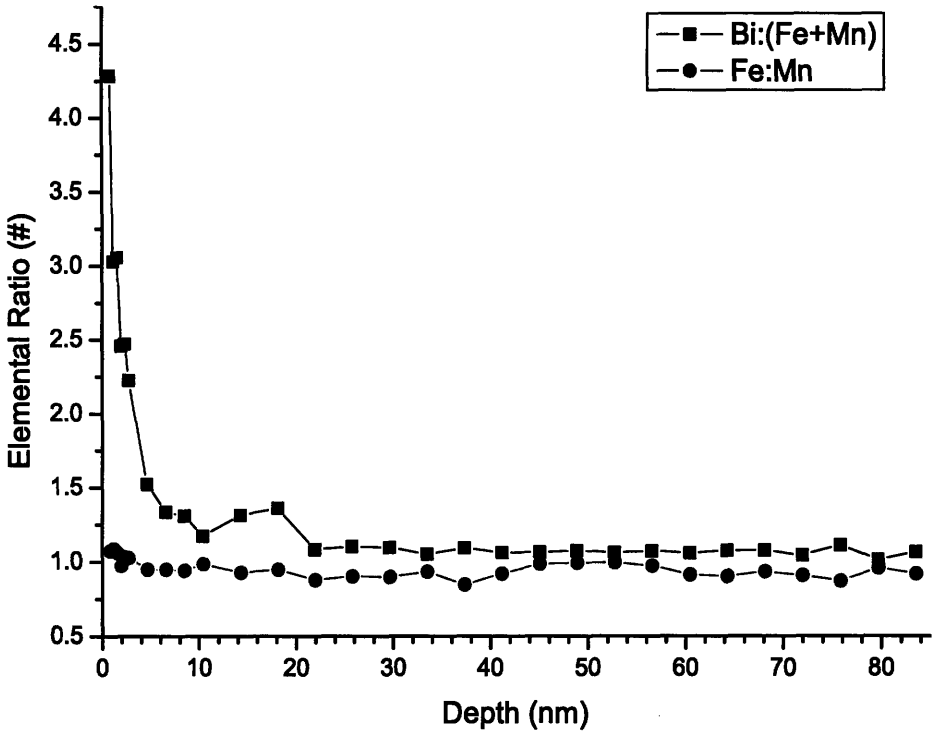

Figure 6-2: Elemental ratios Bi:(Fe+Mn) (black) and Fe:Mn (red) in a 120 nm thick BFM film as a function of depth into the film measured by Scanning Auger Nanoprobe with ion milling. After about 20 nm, the former ratio reaches an average value of 1.07 while the latter reaches an average of 0.97.

ion milling to do a stoichiometric depth profile of this 120 nm film. As shown in Figure 6-2, we found that the former ratio starts at a high value on the surface and eventually decays to 1.07 after a depth of about 20 nm. Interestingly, the Fe:Mn ratio stays fairly constant throughout the film with a value of about 0.97.

At this point, we can only speculate on the origin of this Bi gradient near the surface. One idea is that, because the part of the film closest to the substrate is deposited first and therefore sits on the heater for a longer period of time, this section of the film has more time to volatilize its Bi and reach a stable, stoichiometric composition. On the other hand, the part of the film closest to the surface has the least amount of time on the heater and, therefore, has less time to volatilize its Bi. It is conceivable that the outermost part of the film, then, cools without losing enough Bi to reach the correct stoichiometry. In this case, we would either expect the surface material to be glassy or to be phase separated into bismuth and iron/manganese oxides, or

perhaps $Bi_2Fe_4O_9$ or sillenite. Such a process, however, would most likely produce a linear composition gradient; ours, on the other hand, is far more localized. Another explanation, then, could be that bismuth oxide has a low surface energy and, hence, segregates to the surface of the film preferentially. At any rate, the strange peaks shown in red in Figure 6-1 could be from the surface phase, although 20 nm may be too little material to see by 2DXRD.

To further complicate the matter, XPS was also performed on one of our BFO films retroactively and showed a Bi:Fe ratio of about 3 on the surface, despite a Bi:Fe ratio in the bulk (determined by WDS) close to 1. Unlike in the BFM case, however, with BFO, there are no irregularities on the 2DXRD pattern, indicating that the red peaks in Figure 6-1 may *not* be representative of the surface region. Although we have yet to perform SAN on BFO, we postulate that this surface gradient is a property of the Bi system and does not depend, to first order, on the B-site cation. It poses a significant problem, in particular, to any optical measurements because even a very thin layer of an absorbing phase on the surface will push the absorption of our film way up. As stated in Section 5.2.4, even if 1% of our film is maghemite, which for a 120 nm film is 1.2 nm, we can end up with an $\alpha = 910$ cm^{-1}, as observed. Since the surface layer of the BFM film is 20 nm thick, it is entirely possible, if it is phase separated, that we have that much maghemite. We believe it makes sense to carry this logic over to the BFO films to explain their poor optical properties, although we intend to confirm this theory with SAN shortly.

Clearly, the surface issue must be controlled before moving on to detailed optical characterizations. One proposed method is to simply ion mill the first 20 nm of each film and remeasure them. In addition, we continue to optimize the BFM system and hope to grow and characterize a high quality film shortly.

6.1.2 $LaFe_{0.5}Co_{0.5}O_3$

Another one of our researchers, Dr. Hyun-Suk Kim, has fabricated what we believe to be $LaFe_{0.5}Co_{0.5}O_3$ (LFC) on STO (001). Although we have yet to do WDS to determine the exact Fe:Co ratio, the XRD data shown in Figure 6-3 unambiguously

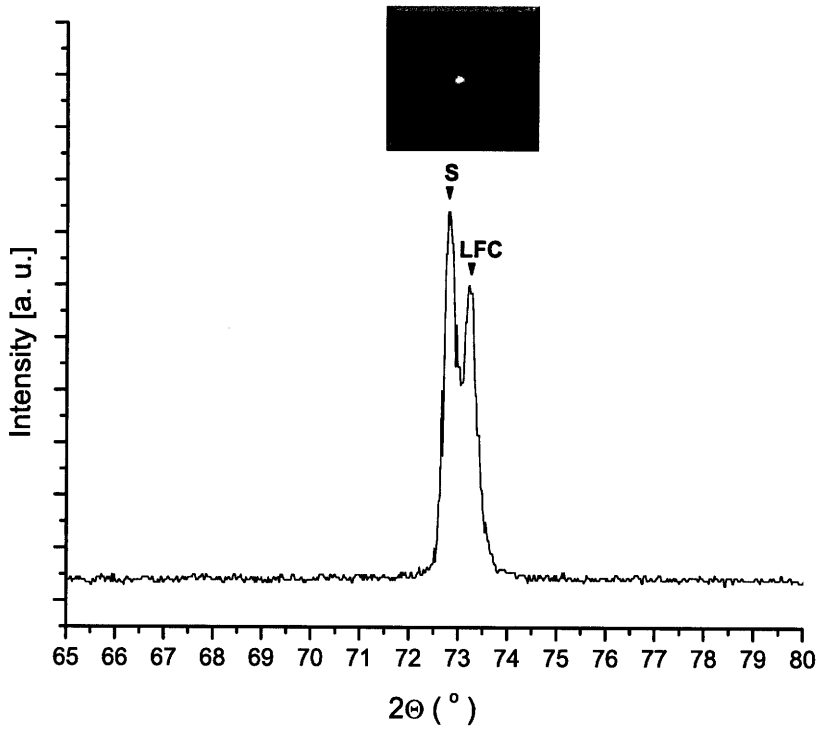

Figure 6-3: γ-integrated XRD intensity as a function of 2Θ for a LFC film on an STO (001) substrate. Also indicated is the 2DXRD pattern. The substrate peak is indicated by an "S" while the epitaxial LFC (003) peak is indicated by "LFC."

shows a truly epitaxial perovskite, very close in d_{001} spacing to the substrate. We should note (with great humility) that Dr. Kim's film is the highest quality one reported in this thesis, with a spread in γ as low as that of the substrate. We attribute his success to the apparently lower volatility of La relative to Bi. For this reason alone, La should be explored further as an A-site substituent, perhaps even as the dominant A-site element, as in $La_{0.9}Bi_{0.1}Fe_{0.5}Mn_{0.5}O_3$, which is currently under investigation. Another good reason to use La more prominently is that La-based orthoferrite has a better lattice match to STO than BFO. The sample shown, for instance, has an approximate $d_{001} = 3.885$ Å, while our BFO film has $d_{001} = 3.947$ Å. STO, as previously stated, has $d_{001} = 3.905$ Å. Lower mismatch may lead to lower linear birefringence, which is desirable from a device standpoint.

6.2 Concluding Remarks and Suggested Work

We have come quite a long way in terms of understanding how to grow high quality BFO films on STO (001) by PLD. We also have come to understand what the most pressing issues are when dealing with Bi in an oxide deposition and, to some degree, how to control these issues. From a characterization point of view, we have learned how to utilize 2DXRD to quickly and completely characterize the phase content of our films. As we inevitably move on to highly substituted materials with varying complexity, the ability to instantly spot any secondary phases at arbitrary angles of γ is one which is unique and invaluable.

In the future, we would like to proceed down two main routes. First and foremost, we need to refine our characterization methods. This involves high-resolution x-ray structural analysis of our most high-quality films on a one-dimensional diffractometer, as well as surface layer depth profiling via SAN methods. Once we are able to get rid of the detrimental surface layer, we can execute a more meaningful optical characterization and perhaps arrive at a non-trival magneto-optical figure of merit. Second, we need to move away from the BFO system and concentrate on systems of mixed A- and B-site cations which can give us substantial room temperature magnetization, all the while keeping Fe in a trivalent state. We should attempt to move away from 100% Bi content and, instead, work with other atoms that are easier to deal with like La or Y.

Further down the road, it would be useful to examine the linear birefringence of these materials as well is their dichroism. These measurements would bring us closer to device fabrication, which is the ultimate goal for some of us. For others, the goal is simply to show that the orthoferrite, which many left in the dust as a magneto-optical material 30 years ago, nevertheless shows interesting and perhaps useful properties. Although we claim to exchange "one nuisance for another nuisance," we hope that each subsequent nuisance becomes less noisome and that, eventually, an integrated magneto-optical isolator employing an perovskite-based active material will become a practical possibility.

Bibliography

[1] J. Bautista, M. Morse, and J. Swift. Microphotonics: Hardware for the Information Age. 2005 Communications Technology Roadmap, MIT Microphotonics Center, 2005.

[2] J. Hecht. *Understanding Fiber Optics.* Prentice-Hall, Inc., Upper Saddle River, NJ, 2006.

[3] G. F. Dionne, G. A. Allen, P. R. Haddad, C. A. Ross, and B. Lax. Circular polarization and nonreciprocal propagation in magnetic media. *Lincoln Laboratory Journal*, 15(2):323–340, 2005.

[4] Faraday optical tunable isolators / rotators. `http://www.eoc-inc.com/leysop/Faraday_optical_isolator_rotators.htm`, 2007.

[5] H. Dötsch, N. Bahlmann, O. Zhuromskyy, M. Hammer, L. Wilkens, R. Gerhardt, and P. Hertel. Applications of magneto-optical waveguides in integrated optics: review. *Journal of the Optical Society of America*, 22(1):240–253, 2005.

[6] H. Yokoi, T. Mizumoto, N. Shinjo, N. Futakuchi, and Y. Nakano. Demonstration of an optical isolator with a semiconductor guiding layer that was obtained by use of a nonreciprocal phase shift. *Applied Optics*, 39(33):6158–6164, 2000.

[7] M. A. Gilleo and S. Geller. Magnetic and crystallographic properties of substituted yttrium-iron garnet $3Y_2O_3 \cdot xM_2O_3 \cdot (5-x)Fe_2O_3$. *Physical Review*, 110(1):73–78, 1959.

[8] S. Y. Sung, N. H. Kim, and B. J. H. Stadler. Magneto-optic materials for integrated applications. *Materials Research Society Symposium Proceedings*, 768:G4.6.1–G4.6.1, 2003.

[9] D. L. Wood and J. P. Remeika. Effect of impurities on the optical properties of yttrium iron garnet. *Journal of Applied Physics*, 38(3), 1967.

[10] S. H. Wemple, S. L. Blank, J. A. Seman, and W. A. Biolsi. Optical properties of epitaxial iron garnet films. *Physical Review B*, 9(5), 1974.

[11] G. B. Scott and D. E. Lacklison. Magnetooptic properties and applications of bismuth substituted iron garnets. *IEEE Transactions on Magnetics*, 12(4):292–311, 1976.

[12] R. C. Booth and E. A. D. White. Magneto-optic properties of rare earth iron garnet crystals in the wavelength range 1.1-1.7 μm and their use in device fabrication. *Journal of Physics D: Applied Physics*, 17:579–587, 1984.

[13] W. Zhao. Magneto-optic properties and sensing performance of garnet YbBi:YIG. *Sensors and Actuators A*, 89:250–254, 2001.

[14] A. M. Glazer. Simple ways of determining perovskite structures. *Acta Crystallographia A*, 31:756–762, 1975.

[15] G. H. Kwei, A. C. Lawson, S. J. L. Billinge, and S. W. Cheong. Structures of the ferroelectric phases of barium titanate. *Journal of Physical Chemistry*, 97:2368–2377, 1993.

[16] J. M. Moreau, C. Michel, R. Gerson, and W. J. James. Atomic displacement relationship to rhombohedral deformation in some perovskite-type compounds. *Acta Crystallographia B*, 26:1425–1428, 1970.

[17] C. Michel, J. M. Moreau, and W. J. James. Structural relationships in compounds with $R\bar{3}c$ symmetry. *Acta Crystallographia B*, 27:501–503, 1971.

[18] J. Wang. *Deposition and Characterization of Multiferroic $BiFeO_3$ Thin Films.* PhD dissertation, University of Maryland, Department of Materials Science and Engineering, 2005.

[19] H. Bea, M. Bibes, A. Barthelemy, K. Bouzehouane, E. Jacquet, A. Khodan, J. P. Contour, S. Fusil, F. Wyczisk, A. Forget, D. Lebeugle, D. Colson, and M. Viret. Influence of parasitic phases on the properties of $BiFeO_3$ epitaxial thin films. *Applied Physics Letters*, 87:072508–1–072508–3, 2005.

[20] H. Bea, M. Bibes, E. Jacquet, K. Rode, P. Bencok, and A. Barthélémy. Unravelling the origin of the controversial magnetic properties of $BiFeO_3$ thin films. `http://www.citebase.org/abstract?id=oai:arXiv.org:cond-mat/0606441` (submitted to Physical Review B), 2006.

[21] B. Ruette, S. Zvyagin, A. P. Pyatakov, A. Bush, J. F. Li, V. I. Belotelov, A. K. Zvezdin, and D. Viehland. Magnetic-field induced phase transition in $BiFeO_3$ observed by high-field electron spin resonance: cycloidal to homogenous spin order. *Physical Review B*, 69:064114–1–064114–7, 2004.

[22] J. Wang, J. B. Neaton, H. Zheng, V. Nagarajan, S. B. Ogale, B. Liu, D. Viehland, V. Vaithyanathan, D. G. Schlom, U. V. Waghmare, N. A. Spaldin, K. M. Rabe, M. Wuttig, and R. Ramesh. Epitaxial $BiFeO_3$ multiferroic thin film heterostructures. *Science*, 299:1719–1722, 2003.

[23] N. Wang, J. Cheng, A. Pyatakov, A. K. Zvezdin, J. F. Li, L. E. Cross, and D. Viehland. Multiferroic properties of modified $BiFeO_3$-$PbTiO_3$-based ceramics: Random-field induced release of latent magnetization and polarization. *Physical Review B*, 72:104434–1–104434–5, 2005.

[24] F. Bai, J. Wang, M. Wuttig, J. Li, N. Wang, A. P. Pyatakov, A. K. Zvezdin, L. E. Cross, and D. Viehland. Destruction of spin cycloid in $(111)_c$-oriented $BiFeO_3$ thin films by epitaxial constraint: Enhanced polarization and release of latent magnetization. *Applied Physics Letters*, 86:032511–1–032511–3, 2005.

[25] D. L. Wood, J. P. Remeika, and E. D. Kolb. Optical spectra of rare-earth orthoferrites. *Journal of Applied Physics*, 41(13), 1970.

[26] W. J. Tabor, A. W. Anderson, and L. G. Van Uitert. Visible and infrared Faraday rotation and birefringence of single-crystal rare-earth orthoferrites. *Journal of Applied Physics*, 41(7), 1970.

[27] A. Rajamani, G. F. Dionne, D. Bono, and C. A. Ross. Faraday rotation, ferromagnetism, and optical properties of Fe-doped $BaTiO_3$. *Journal of Applied Physics*, 98:063907–1–063907–4, 2005.

[28] D. J. Griffiths. *Introduction to Electrodynamics.* Prentice-Hall, Inc., Upper Saddle River, NJ, 1999.

[29] N. W. Ashcroft and N. D. Mermin. *Solid State Physics.* Thomson Learning, Inc., United States of America, 1976.

[30] G. F. Dionne and G. A. Allen. Spectral origins of giant Faraday rotation and ellipticity in Bi-substituted magnetic garnets. *Journal of Applied Physics*, 73(10):6127–6129, 1993.

[31] S. Wittekoek, T. J. A. Popma, J. M. Robertson, and P. F. Bongers. Magneto-optic spectra and the dielectric tensor elements of bismuth-substituted iron garnets at photon energies between 2.2-2.5 eV. *Physical Review B*, 12(7):2777–2788, 1975.

[32] G. F. Dionne and G. A. Allen. Molecular-orbital analysis of magneto-optical Bi-O-Fe hybrid excited states. *Journal of Applied Physics*, 75(10):6372–6374, 1994.

[33] M. N. R. Ashfold, F. Claeyssens, G. M. Fuge, and S. J. Henley. Pulsed laser ablation and deposition of thin films. *Chemical Society Review*, 33:23–31, 2004.

[34] H. Perowne. Image of PLD plume. `http://en.wikipedia.org/wiki/Image:PLD%20Plume.png`, 2006.

[35] Bruker AXS D8 DISCOVER with GADDS (image). http://www.bruker-axs.de/uploads/pics/D8-DISCOVER-with-GADDS%2001.jpg, 2007.

[36] B. B. He, U. Preckwinkel, and K. L. Smith. Fundamentals of two-dimensional x-ray diffraction (XRD^2). *Advances in X-ray Analysis*, 43:273–280, 2000.

[37] Bruker AXS Ewald Spheres (image). http://www.bruker-axs.de/uploads/tx%20linkselectorforpdfpool/XRD2%20Poster%20A4%20P88-E00045.pdf, 2007.

[38] VSM Schematic. http://cnsm.kaist.ac.kr/Vsmsys.jpg, 2007.

[39] F. Bernoux, J. P. Piel, B. Castellon, C. Defranoux, J. H. Lecat, P. Boher, and J. L. Stehlé. Ellipsométrie théorie. *http://www.sopra-sa.com*, 2007.

[40] M. I. Morozov, N. A. Lomanova, and V. V. Gusarov. Specific features of $BiFeO_3$ formation in a mixture of bismuth(III) and iron(III) oxides. *Russian Journal of General Chemistry*, 73(11):1676–1680, 2003. Translated from *Zhurnal Obshchei Khimii*.

[41] S. Kahl and A. M. Grishin. Evolution of properties of epitaxial bismuth iron garnet films with increasing thickness. *Journal of Magnetism and Magnetic Materials*, 278:244–255, 2004.

[42] G. B. Scott, D. E. Lacklison, and J. L. Page. Absorption spectra of $Y_3Fe_5O_{12}$ (YIG) and $Y_3Ga_5O_{12}$:Fe^{3+}. *Physical Review B*, 10(3):971–986, 1974.

[43] J. Li, J. Wang, M. Wuttig, R. Ramesh, N. Wang, B. Ruette, A. P. Pyatakov, A. K. Zvezdin, and D. Viehland. Dramatically enhanced polarization in (001), (101), and (111) $BiFeO_3$ thin films due to epitaxial-induced transitions. *Applied Physics Letters*, 84(25):5261–5263, 2004.

[44] H. D. Megaw. Crystal structure of double oxides of the perovskite type. *The Proceedings of the Physical Society*, 58(2):133–152, 1946.

[45] L. E. Helseth, R. W. Hansen, E. I. Il'yashenko, M. Baziljevich, and T. H. Johansen. Faraday rotation spectra of bismuth-substituted ferrite garnet films with in-plane magnetization. *Physical Review B*, 64, 2001.

[46] Coaxial Cable Specifications. `http://www.rfcafe.com/references/electrical/coax_chart.htm`, 2007.

[47] B. M. Holmes, D. C. Hutchings, and J. J. Bregenzer. Experiments towards the realisation of a monolithically-integrated optical isolator incorporating quasi-phase matched magneto-optical effects. *Materials Research Society Symposium Proceedings*, 834:J4.4.1–J4.4.6, 2005.

[48] B. Stadler, K. Vaccaro, P. Yip, J. Lorenzo, Y. Li, and M. Cherif. Integration of magneto-optical garnet films by metal-organic chemical vapor deposition. *IEEE Transactions on Magnetics*, 38(3):1564–1567, 2002.

[49] L. J. C. Rivera, S. Pandit, S. Pieski, R. Cobian, and M. Cherif. Integrated isolators for opto-electro-mechanical systems and devices. *Proceedings of SPIE*, 4284:29–42, 2001.

[50] A. K. Zvezdin and V. A. Kotov. *Modern Mangetooptics and Magnetooptical Materials.* Institute of Physics Publishing, London, UK, 1997.

[51] P. Hansen, C. P. Klages, and K. Witter. Magnetic and magneto-optic properties of praseodymium- and bismuth-substituted yttrium iron garnet films. *Journal of Applied Physics*, 60(2):721–727, 1986.

[52] J. L. Deschanvres, M. Langlet, and J. C. Joubert. Garnet thin film deposited by a new chemical vapour deposition. *Thin Solid Films*, 175:281–285, 1989.

[53] M. Okada, S. Katayama, and K. Tominaga. Preparation and magneto-optic properties of Bi-substituted yttrium iron garnet thin films by metalorganic chemical vapor deposition. *Journal of Applied Physics*, 69(6):3566–3570, 1991.

[54] M. Gomi, T. Tanida, and M. Abe. rf sputtering of highly Bi-substituted garnet films on glass substrates for magneto-optic memory. *Journal of Applied Physics*, 57(8):3888–3890, 1985.

[55] P. C. Dorsey, S. E. Bushnell, and C. Vittoria. Epitaxial yttrium iron garnet films grown by pulsed laser deposition. *Journal of Applied Physics*, 74(2):1242–1246, 1993.

[56] E. Popova, N. Keller, F. Gendron, M. Guyot, M. C. Brianso, Y. Dumond, and M. Tessier. Structure and magnetic properties of yttriumirongarnet thin films prepared by laser deposition. *Journal of Applied Physics*, 90(3):1422–1428, 2001.

[57] T. Tepper and C. A. Ross. Pulsed laser deposition and refractive index measurement of fully substituted bismuth iron garnet films. *Journal of Crystal Growth*, 255:324–331, 2003.

[58] Robert O'Handley. *Modern Magnetic Materials.* John Wiley & Sons Inc., New York, NY, 2000.

[59] R. Wolfe, R. A. Lieberman, V. J. Fratello, R. E. Scotti, and N. Kopylov. Etch-tuned waveguide magneto-optical isolator. *Applied Physics Letters*, 56(5):426–428, 1990.

[60] A. S. Bhalla, R. Guo, and R. Roy. The perovskite structure - a review of its role in ceramic science and technology. *Materials Research Innovations*, 4(1):3–26, 2000.

[61] J. D. Bucci, B. K. Robertson, and W. J. James. The precision determination of the lattice parameters and coefficients of thermal expansion of $BiFeO_3$. *Journal of Applied Crystallography*, 5:187–191, 1972.

[62] H. D. Megaw and C. N. W. Darlington. Geometrical and structural relations in the rhombohedral perovskites. *Acta Crystallographia A*, 31:161–173, 1975.

[63] C. M. Foster, Z. Li, M. Buckett, D. Miller, P. M. Baldo, L. E. Rehn, G. R. Bai, D. Guo, H. You, and K. L. Merkle. Substrate effects on the structure of $PbTiO_3$ thin films prepared on MgO, $LaAlO_3$, and $SrTiO_3$ by metalorganic chemical-vapor deposition. *Journal of Applied Physics*, 78(4), 1995.

[64] D. Lee, M. G. Kim, S. Ryu, H. M. Jang, and S. Lee. Epitaxially grown La-modified $BiFeO_3$ magnetoferroelectric thin films. *Applied Physics Letters*, 86:222903–1–222903–3, 2005.

[65] S. R. Das, P. Bhattacharya, P. Choudhary, and R. S. Katiyar. Effect of La substitution on structural and electrical properties of $BiFeO_3$ thin film. *Journal of Applied Physics*, 99:066107–1–066107–3, 2006.

[66] X. Qi, J. Dho, M. Blamire, Q. Jia, J. S. Lee, S. Foltyn, and J. L. MacManus-Driscoll. Epitaxial growth of $BiFeO_3$ thin films by LPE and sol-gel methods. *Journal of Magnetism and Magnetic Materials*, 283:415–421, 2004.

[67] R. Ueno, S. Okaura, H. Funakubo, and K. Saito. Crystal structure and electrical properties of epitaxial $BiFeO_3$ thin films grown by metal organic chemical vapor deposition. *Japanese Journal of Applied Physics*, 44(39):L1231–L1233, 2005.

[68] S. W. Lee and C. S. Kim. Growth of multiferroics $BiFeO_3$ thin films by sol-gel method. *Journal of Magnetism and Magnetic Materials*, 304:e772–e774, 2006.

[69] M. Murakami, S. Fujino, S. H. Lim, L. G. Salamanca-Riba, M. Wuttig, I. Takeuchi, B. Varughese, H. Sugaya, T. Hasegawa, and S. E. Lofland. Microstructure and phase control in Bi-Fe-O multiferroic nanocomposite thin films. *Applied Physics Letters*, 88:112505–1–112505–3, 2006.

[70] C. Ederer and N. A. Spaldin. Weak ferromagnetism and magnetoelectric coupling in bismuth ferrite. *Physical Review B*, 71:060401–1–060401–4, 2005.

[71] W. Eerenstein, F. D. Morrison, J. Dho, M. G. Blamine, J. F. Scott, and N. D. Mathur. Comment on "Epitaxial $BiFeO_3$ multiferroic thin film heterostructures". *Science*, 307:1203a, 2005.

[72] J. Wang, A. Scholl, H. Zheng, S. B. Ogale, D. Viehland, D. G. Schlom, N. A. Spaldin, K. M. Rabe, M. Wuttig, L. Mohaddes, J. Neaton, U. V. Waghmare, T. Zhao, and R. Ramesh. Response to Comment on "Epitaxial $BiFeO_3$ multiferroic thin film heterostructures". *Science*, 307, 2005.

[73] Y. K. Jun, W. T. Moon, C. M. Chang, H. S. Kim, H. S. Ryu, J. W. Kim, K. H. Kim, and S. H. Hong. Effects of Nb-doping on electric and magnetic properties in multi-ferroic $BiFeO_3$ ceramics. *Solid State Communications*, 135:133–137, 2005.

[74] T. Tepper and C. A. Ross. Microstructure and optical properties of pulsed-laser-deposited iron oxide films. *IEEE Transactions on Magnetics*, 40(3):1685–1690, 2004.

[75] P. S. Pershan. Magneto-optical effects. *Journal of Applied Physics*, 38(3):1482–1490, 1967.

[76] Y. Jun, W. Moon, C. Chang, H. Kim, H. Ryu, J. Kim, K. Kim, and S. Hong. Effects of Nb-doping on electric and magnetic properties in multi-ferroic $BiFeO_3$ ceramics. *Solid State Communications*, 135:133–137, 2005.

[77] W. J. Tabor and F. S. Chen. Electromagnetic propagation through materials possessing both Faraday rotation and birefringence: experiments with Ytterbium orthoferrite. *Journal of Applied Physics*, 40(7):2760–2765, 1969.

[78] S. R. Woodford, A. Bringer, and S. Blügel. Interpreting magnetization from Faraday rotation in birefringent magnetic media. *Journal of Applied Physics*, 101:053912–1–053912–7, 2007.

[79] J. R. Reitz, F. J. Milford, and R. W. Christy. *Foundations of Electromagnetic Theory.* Addison-Wesley Publishing Company, Reading, MA, 1993.

[80] F. J. Kahn, P. S. Pershan, and J. P. Remeika. Ultraviolet magneto-optical properties of single-crystal orthoferrites, garnets, and other ferric oxide compounds. *Physical Review*, 186:891–918, 1969.

[81] R. K. Singh and J. Narayan. Pulsed-laser evaporation technique for deposition of thin films: Physics and theoretical model. *Physical Review B*, 41(13):8843–8859, 1990.

[82] T. J. Jackson and S. B. Palmer. Oxide superconductor and magnetic metal thin film deposition using pulsed laser ablation: a review. *Journal of Physics D*, 27:1581–1594, 1997.

[83] P. R. Willmott and J. R. Huber. Pulsed laser vaporization and deposition. *Review of Modern Physics*, 72(1), 2000.

[84] D. B. Chrisey and G. K. Hubler, editors. *Pulsed Laser Deposition of Thin Films.* John Wiley & Sons, Inc., New York, NY, 1994.

[85] R. Jenkins and R. L. Snyder. *Introduction to X-ray Powder Diffractometry.* John Wiley & Sons, Inc., New York, NY, 1996.

[86] R. E. Cefalu and A. H. King. Texture development and twinning in polycrystalline gold thin films. *Materials Research Society Symposium Proceedings*, 721:J2.2.1–J2.2.6, 2002.

[87] B. B. He. Introduction to two-dimensional x-ray diffraction. *Powder Diffraction*, 18(2):71–85, 2003.

[88] S. Foner. Versatile and sensitive vibrating-sample magnetometer. *Review of Scientific Instruments*, 30:548–557, 1959.

[89] B. D. Cullity. *Introduction to Magnetic Materials.* Addison-Wesley Publishing Co., Reading, MA, 1972.

[90] R. M. A. Azzam and N. M. Bashara. *Ellipsometry and Polarized Light.* North-Holland, New York, NY, 1987.

[91] D. B. Williams, J. I. Goldstein, and D. E. Newbury, editors. *X-Ray Spectrometry in Electron Beam Instruments.* Plenum Press, New York, NY, 1995.

[92] M. Valant and D. Suvorov. Processing and dielectric properties of sillenite compounds. *Journal of the American Ceramic Society*, 84(12):2900–2904, 2001.

[93] Z. C. Xu, M. Yan, M. Li, Z. L. Zhang, and M. Huang. Faraday rotation spectra analysis of Bi-substituted mixed rare-earth iron garnet crystals in optical communication band. *Journal of Applied Physics*, 101:053910–1–053910–4, 2007.

[94] G. F. Dionne, A. R. Taussig, M. Bolduc, L. Bi, and C. A. Ross. Mixed-cation designs of magnetic perovskites for Faraday rotation at IR wavelengths. *Journal of Applied Physics*, 101(9), 2007. In press.

[95] A. F. Moreira dos Santos, A. K. Cheetham, W. Tian, X. Pan, Y. Jia, N. J. Murphy, J. Lettieri, and D. G. Schlom. Epitaxial growth and properties of metastable $BiMnO_3$ thin films. *Applied Physics Letters*, 84(1):91–93, 2004.

[96] A. A. Belik, S. Iikubo, K. Kodama, N. Igawa, S. Shamoto, S. Niitaka, M. Azuma, Y. Shimakawa, M. Takano, F. Izumi, and E. Takayama-Muromachi. Neutron powder diffraction study on the crystal and magnetic structures of $BiCoO_3$. *Chemistry of Materials*, 18:798–803, 2006.

[97] H. Wadati, M. Takizawa, T. T. Tran, K. Tanaka, T. Mizokawa, A. Fujimori, A. Chikamatsu, H. Kumigashira, M. Oshima, S. Ishiwata, M. Azuma, and M. Takano. Valence changes associated with the metal-insulator transition in $Bi_{1-x}La_xNiO_3$. *Physical Review B*, 72:155103–1–155103–5, 2005.

[98] C. H. Yang, T. Y. Koo, and Y. H. Jeong. How to obtain magnetocapacitance effects at room temperature: The case of Mn-doped $BiFeO_3$. *Solid State Communications*, 134:299–301, 2005.

[99] K. Ueda, Y. Muraoka, H. Tabata, and T. Kawai. Atomic ordering in the $LaFe_{0.5}Mn_{0.5}O_3$ solid solution film. *Applied Physics Letters*, 78(4):512–514, 2001.

[100] H. A. Jahn and E. Teller. Stability of polyatomic molecules in degenerate electronic states. I. Orbital degeneracy. *Proceedings of the Royal Society of London. Series A. Mathematical and Physical Sciences*, 161(905):220–235, 1937.

[101] P. Dai, J. Zhang, H. A. Mook, S. H. Liou, P. A. Dowben, and E. W. Plummer. Experimental evidence for the dynamic Jahn-Teller effect in $La_{0.65}Ca_{0.35}MnO_3$. *Physical Review B*, 54(6):R3694–R3697, 1996.

[102] K. Y. Yun, M. Noda, M. Okuyama, H. Saeki, H. Tabata, and K. Saito. Structural and multiferroic properties of $BiFeO_3$ thin films at room temperature. *Journal of Applied Physics*, 96(6):3399–3403, 2004.